A Two-Photon E1-M1 Optical Clock

by

Emily A. Alden

A dissertation submitted in partial fulfillment
of the requirements for the degree of
Doctor of Philosophy
(Physics)
in The University of Michigan
2014

Doctoral Committee:

Assistant Professor Aaron E. Leanhardt, Chair
Professor Luming Duan
Professor Timothy A. McKay
Professor Georg A. Raithel
Professor Duncan G. Steel

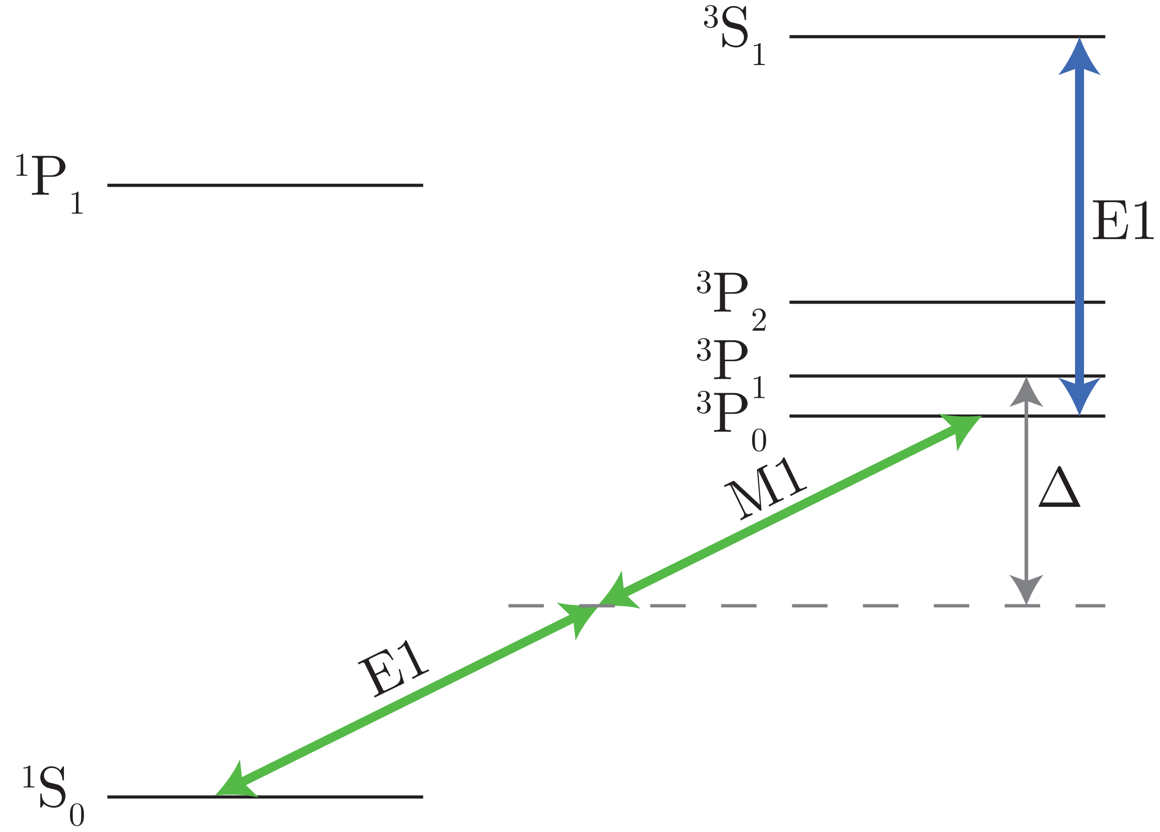
$^3S_1$
$^1P_1$
E1
$^3P_2$
$^3P_1$
$^3P_0$
M1
Δ
E1
$^1S_0$

For my mentors and my family

ACKNOWLEDGEMENTS

I want to express my sincere gratitude to my advisor Aaron Leanhardt. Aaron is tirelessly driven, both in his research and teaching. Indeed, tireless understates the amount of energy he invests in his work and his students. Everyone in his research group benefited from the breadth of his experience and the formative methods he used to support us as researchers and scientists. I'm particularly grateful for the crucible of the weekly group presentations. Though the scrutiny could be bracing, I can trace most of the pivotal steps I've taken as a physicist during my doctoral research to that forum. His perfect accommodation of my schedule needs when I became a mom was crucial to my success, I am grateful for all of Aaron's support.

I am deeply indebted to my colleagues in lab. Kaitlin Moore started work in our lab while she was an undergraduate and quickly became my valued colleague. Her skill and thoroughness is unparalleled, but our shared affinity for MatLab is what bonded us most. Jeongwon (Chris) Lee's fascinating research on the eEDM was separate from my work, but that never stopped him from following and contributing to my project. I deeply appreciated his willingness to take the third shift so I could work during the days and spend evenings with my sweet children. Yisa Rumala's enthusiasm for reporting the good news in his research helped remind me how important it is to keep track of what is working even when most time is spent on what isn't.

I would like to thank the University of Michigan Demonstration Lab, specifically Warren Smith and Mark Kennedy. During my time there I found mentors and made great friends. I am still humbled by the support I received.

The crucible of new parenthood forged indelible friendships for me in Ann Arbor, I deeply treasure the community I've found here. The life lesson I've learned: you know you live on the right street when you vacation with your neighbors (France anybody?).

I am grateful for the support of my husband's family, now my family. Phil and Mary Ann are the embodiment of generosity and love. Jim and Liz are good friends and I have come to admire them as great parents and revere them as they steer the ship for our heart family with grace, strength, and love. My darling niece and nephew fill my heart with joy. My brother-in-law Rob I love as a fellow geek and admire as a kind person.

I appreciate the support and love of my family. My mom's confidence in my scientific ability can be measured by her repeated inquiries if my research will enable superluminal, intergalactic communication (as a modest precursor to superluminal travel). I haven't been able to to dissuade her from that idea, but I'm glad the conversation continues. My dad's admirable blend of pragmatism and hedonism has shown me a great example of work ethic and a lifelong delight for dim sum. My sister's ebullient love for family both inspires and strengthens me.

My husband John's love has supported me, but his real gift has been sharing a seat on this safari through life. My beloved and charming girls: Amina who regales me (to my delight) with songs and stories and Poppy who laughs harder than I do when she tickles me. Tupo.

TABLE OF CONTENTS

CHAPTER

LIST OF FIGURES

Figure

LIST OF TABLES

Table

LIST OF APPENDICES

Appendix

LIST OF ABBREVIATIONS

OFS	Optical Frequency Standards
GPS	Global Positioning Systems
E1	Electric Dipole
M1	Magnetic Dipole
SHG	Second Harmonic Generation
AOM	Acousto-Optic Modulator
PPMgO:SLT	Periodically Poled MgO-Doped : Stoichiometric Lithium Tantalate
EEP	Einstein's Equivalence Principle
OD	Optical Depth
PMT	Photo-multiplier Tube
CW	Continuous Wave

LIST OF SYMBOLS

$\mathcal{S}$	Stability [$\sqrt{\mathrm{Hz}^{-1}}$]
σ_ν	Instability
$\Delta\nu$	Frequency Resolution [Hz]
$\mathcal{T}$	Experiment Period [s]
ν	Optical Frequency [Hz]
ν_0	Fundamental (Natural) Frequency [Hz]
ν_L	Laser Frequency [Hz]
τ	Experiment Duration [s]
N	Atoms Sampled [#]
$\Omega_{R2\gamma}$	Two-Photon Rabi Frequency [Hz]
σ	Van der Waals radius [m^2]
B	Magnetic Field [$^{T}/_{m}$]
c	speed of light [$^{m}/_{s}$]
E	Energy [J]
F	Electric Field [$^{V}/_{m}$]
g	local acceleration due to gravity [$^{m}/_{s^2}$]
h	Planck's constant [Js]
k_B	Boltzmann Constant [$^{J}/_{K}$]
M	atomic mass [kg]
ρ	number density [m^{-3}]
$\Delta\nu$	Effective Linewidth [Hz]

$\Delta\nu_{\mathrm{nat}}$	Natural Linewidth [Hz]
$\Delta\nu_{BB}$	Black-body Radiation Shift Broadening [Hz]
$\Delta\nu_{C}$	Collision Broadening [Hz]
$\Delta\nu_{D1}$	First-order Doppler Broadening [Hz]
$\Delta\nu_{D2}$	Second-order Doppler Broadening [Hz]
$\Delta\nu_{LL}$	Laser-Line Broadening [Hz]
$\Delta\nu_{LS}$	Light Shift Broadening [Hz]
$\Delta\nu_{TT}$	Transit-time Broadening[Hz]
ν_{BB}	Black-body Radiation Shift [Hz]
ν_{B}	Frequency Bias [Hz]
ν_{C}	Collision Shift [Hz]
ν_{D2}	Second-order Doppler Shift [Hz]
ν_{G}	Gravitational Redshift [Hz]
ν_{LS}	Light Shift [Hz]
ω_0	Gaussian Radius of the laser-beam [m]
T	Vapor Cell Temperature [K]
$\dot{N}_D$	Detection of $^3P_0$ Atoms Rate [s^{-1}]
$\dot{N}_{tot}$	Interrogation Rate [s^{-1}]
$\dot{N}_{^3P_0}$	Excitation Rate of Ensemble to $^3P_0$ Level [s^{-1}]
N	Sample Size [#]
N_C	Number of Collided Atoms [#]
P_D	Probability of Detection
$P_{^3P_0}$	Probability of Clock Excitation (single-atom)
P_{nc}	Probability of no collision
P_{pc}	Probability of photon collection
$\alpha_{^1S_0}(\lambda)$	Dynamic Dipole Polarizability of $^1S_0$ Ground State [a.u.]
$\alpha_{^3P_0}(\lambda)$	Dynamic Dipole Polarizability of $^3P_0$ Clock State [a.u.]

$\Delta\alpha(\lambda)$	Dynamic Dipole Polarizability Difference between ${}^1S_0$ and ${}^3P_0$ States [a.u.]
2γ	two-photon
$2z_R$	Rayleigh Range [m]
$\bar{v}$	mean atomic velocity $[{}^{m}\!/_{s}]$
Δh	Elevation change [m]
$\hat{v}$	unit atomic velocity (orientation) $[{}^{m}\!/_{s}]$
λ	wavelength [nm]
ξ	Focusing parameter
J	Total Angular Momentum Quantum Number
k	wavevector $[{}^{rad}\!/_{m}]$
L_o	Detection Limit [m]
Q	Quality Factor of Resonator
v	atomic velocity $[{}^{m}\!/_{s}]$
v_P	most probable atomic velocity $[{}^{m}\!/_{s}]$

ABSTRACT

A Two-Photon E1-M1 Optical Clock

by

Emily A. Alden

Chair: Aaron E. Leanhardt

Innovations in precision frequency measurement advance popular technologies such as global positioning systems (GPS), permit the testing of fundamental physics constants, and have the potential to measure local variations of acceleration due to gravity. Driving optical transitions for frequency measurement using an E1-M1 excitation scheme in a hot mercury (Hg) vapor cell is viable and could be the basis of a portable optical frequency standard with comparable accuracy to the most precise atomic clocks in the world.

This dissertation describes in detail the new E1-M1 method of high-precision frequency measurement in an optical, atomic clock. This two-photon scheme using electric (E1) and magnetic (M1) dipole coupling could attain high levels of accuracy and improve on existing systems through the simplicity of the experimental setup. The optimal operating temperature for an E1-M1 clock using neutral Hg has been calculated here to be 380 K, an accessible temperature for a hot vapor cell and therefore convenient for a portable E1-M1 frequency standard. Such a portable optical frequency standard would permit trace gravitational redshift measurement in far-flung locations on earth and in space. Analysis of both the E1-M1 optical transition and

thermal properties of the candidate clock atoms are presented. These models allow a stability estimate of an E1-M1 optical clock and recommend experimental settings to optimize the standard. The experimental work that has been performed in pursuit of observing the E1-M1 clock transition in Hg is also discussed.

A clock is a time-keeping system composed of two essential components: an oscillator and an oscillation counter. An atomic clock's oscillator is a transition between atomic energy levels that can be driven by an external resonator, for example a laser. The cesium clock which defines our second has an internal resonance such that when an external resonator excites that hyperfine transition (i.e. is resonant) then that external resonator is defined to have a frequency of exactly 9,192,631,770 Hz. An optical clock operates by making a precision frequency measurement of a laser that has been brought into resonance with that clock's oscillator: a high quality atomic level transition. Group II type atoms, such as Hg, have the ${}^1S_0 \rightarrow {}^3P_0$ clock transition that is an ideal basis for a frequency standard.

The E1-M1 excitation scheme proposed here allows hot atoms to be used as clock oscillators. Exciting an atom to the ${}^3P_0$ clock level can be done by bringing a laser's frequency into resonance with a two-photon allowed transition ${}^1S_0 \overset{\text{E1}}{\longleftrightarrow} {}^3P_1 \overset{\text{M1}}{\longleftrightarrow} {}^3P_0$. This is in contrast to other optical clocks which use lasers to drive a single-photon E1-type transition. Single-photon schemes must use ultracold atoms to reduce atomic motion and eliminate Doppler broadening in order to attain high levels of accuracy. It is difficult to produce ultracold atoms, so these clock systems operate with a single atom (optical ion clocks) or at most a few thousand atoms (optical lattice clocks). The equipment required to control ultracold atoms is bulky and cannot be easily transported. Driving the clock transition with a pair of degenerate counter-propagating photons in an E1-M1 scheme reduces Doppler broadening effects without the need for ultracold atoms. This allows frequency measurement to be performed at temperatures that have large atomic number densities ρ. For example, a typical Hg vapor cell at T=400 K can contribute 10^{10} atoms for measurement in an E1-M1 optical frequency standard. The advantage of increasing the number of addressed clock atoms is an increase in statistical accuracy.

Atomic Hg is the ideal system for a hot E1-M1 optical clock. Hg has a particularly large number density compared to other group II type atoms. A drop of Hg in a vapor cell at room temperature will have a vapor number density fifteen orders of magnitude larger than the next group II type atom, a property related to Hg's unusual liquid state at room temperature. The resonant frequency for Hg's clock transition is an optimally large PHz frequency; this is 100,000 times larger than the 9 GHz frequency of the Cs atomic clock. The specific wavelength of the clock transition in Hg is readily available. The monochromatic two-photon scheme operates at 531 nm, that is the same shade of green found in hand-held laser pointers because it is the second harmonic product of the common Nd:YAG laser system's wavelength. Another advantage is that the Hg clock's detection channel cycles with the same wavelength used in Blu-Ray players (405 nm). When resonant lasers for an atomic system are easily available off the shelf, so too are the optics and detectors needed to assemble the excitation and detection systems. These features in Hg position it as the ideal atomic system for a two-photon E1-M1 optical clock.

CHAPTER I

Precision Measurement with Atomic Systems

Recent advancements in Optical Frequency Standards (OFS) have seen three different systems hold the mantle of lowest stability ($\mathcal{S}$) in the past year [10, 23, 8]. These lattice and ion OFSs have attained high levels of precision by reducing the frequency uncertainty of clock atoms through exquisite control of the experimental environment. Increases in accuracy advance popular technologies such as Global Positioning Systems (GPS), permit testing of fundamental physics constants, and have the potential to measure variations in local gravity [11]. Most of these applications will benefit from an OFS that is portable so that an individual, local measurement can be compared to measurements from other locations. A map of the earth's geodesy measured locally with the precision of an optical frequency standard is one metrology application that will require a mobile atomic clock. An optical frequency standard using a portable vapor cell as the source of clock atoms can achieve high precision with a two-photon E1-M1 Doppler-free spectroscopy scheme.

The E1-M1 optical clock is a frequency standard based on a two-photon excitation from the ground state to the clock state by a pair of Electric Dipole (E1) and Magnetic Dipole (M1) allowed transitions. This novel scheme is in contrast to the one-photon, E1 transition that is currently used in lattice and ion systems [10, 23, 8]. Figure 1.1 diagramatically illustrates the E1-M1 optical transition scheme in group II type

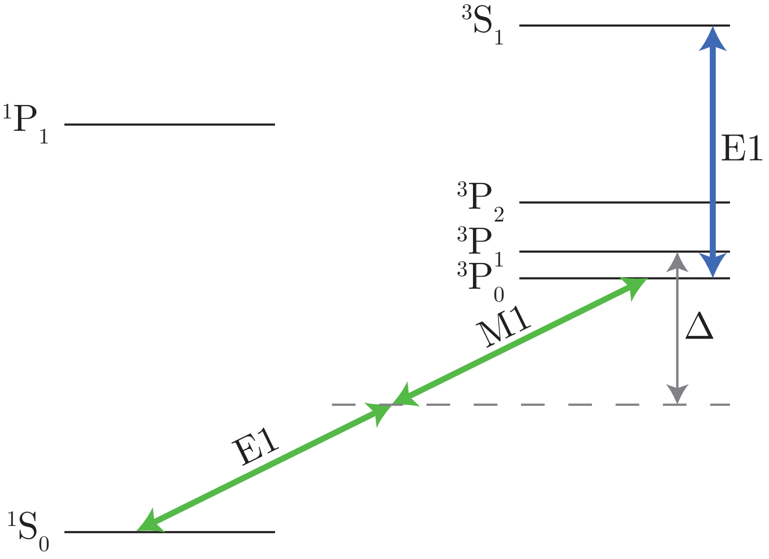

Figure 1.1: **Two-Photon Clock Level Structure** This is the prototypical, optical clock level structure for group II type atoms with a $^3P_0$ clock state. The electric field of one photon and the magnetic field of a second, degenerate photon directly couple the $^1S_0$ ground state to the clock state via the intermediate $^3P_1$ level. Detuning (Δ) by the excitation photons from the intermediate level impacts the two-photon Rabi frequency and transition probability. A sample detection channel for a hot clock is the $^3P_0 \overset{\text{E1}}{\longleftrightarrow} {}^3S_1$, E1 allowed transition.

atoms.

An ideal optical frequency standard will be able reach its highest accuracy (its minimum instability σ_ν) quickly. The benchmark by which all frequency standards are compared is therefore stability $\mathcal{S}$, the rate at which σ_ν can be attained where

$$\sigma_\nu(\tau) = \mathcal{S}/\sqrt{\tau} \tag{1.1}$$

and τ is the total measurement time (usually the aggregate of many rapid frequency measurements). The smallest instability σ_ν measurement ever recorded in an OFS is $\sigma_\nu = 1.6 \times 10^{-18}$. This was achieved in a Yb lattice clock after $\tau = 7$ hours of measurement time [23].

Stability $\mathcal{S}$ has units of $\left[\sqrt{\text{Hz}^{-1}}\right]$ and is fundamentally limited by

$$\mathcal{S} = \frac{\Delta\nu}{\nu}\sqrt{\frac{\mathcal{T}}{N_D}} \tag{1.2}$$

where ν is the fundamental frequency of the standard, $\Delta\nu$ is the effective linewidth of the oscillator, $\mathcal{T}$ is the period of each detection cycle, and N_D is the effective number of atoms that are detected in each experiment period.

A specific advantage of the hot E1-M1 optical clock described here is a large increase in N_D and only a small increase in linewidth $\Delta\nu$ compared with other ultracold optical frequency standards. Specifically, we calculate that for an increase of sample number N_D by 10^7, we only observe an increase to the linewidth $\Delta\nu$ by 10^5 compared to the Yb and Sr lattice clock systems [23, 8]. Other optical frequency standards require extensive state preparation to remove first-order Doppler effects as the largest broadening mechanism, a process that limits the number of atoms that can be addressed and requires a laboratory full of equipment to control the frequency measurement. In contrast, this E1-M1 scheme is able to reduce Doppler broadening while addressing large numbers of atoms in a portable, vapor cell. The potentially small $\mathcal{S}$ of the E1-M1 scheme could make it an ideal optical frequency standard for portable metrology applications.

1.1 Precision Measurement

Any measurement of a magnitude A performed in a precise way will report the mean magnitude measured $\bar{A}$ after a sequence of samples along with the statistical error $\varepsilon(A)$ of the measurement. The statistical error is a straightforward numerical calculation from measurement data $\varepsilon(A) = \mathrm{StDev}(A)/\sqrt{N}$, where $\mathrm{StDev}(A)$ is the standard deviation of the data and N is the number of data points (sample size). It turns out that all measurements can be compared to each other in terms of instability σ_A, a dimensionless quantity that is the ratio of measurement error $\varepsilon(A)$ over the mean magnitude $\bar{A}$ where $\sigma_A = \varepsilon(A)/\bar{A}$ and relatively small instability σ_A denotes a better measurement.

Precision measurement systems (such as optical frequency standards) require small instabilities, so it is useful to predict the statistical error of a measurement and select a system with a large initial magnitude. The optical frequencies ν of the clock transitions in group II type atoms have near PHz laser frequencies, this is a large initial magnitude. Prediction of error $\varepsilon(\nu)$ is possible if characteristic features of the system and sample size are known, for example the Gaussian distribution of thermal velocities.

Estimation of frequency measurement error $\varepsilon(\nu)$ requires characterization of the effective linewidth $\Delta\nu$ and the potential number of detected atoms N_D. The effective linewidth $\Delta\nu$ of the optical transition is the standard deviation of optical frequencies that will excite the transition, usually dominated by a Gaussian probability distribution from Doppler broadening. It is worthwhile to select atoms and experimental settings that reduce this linewidth. Increasing the number of detected atoms N_D or increasing the sample number of the experiment $\tau/\mathcal{T}$ are two methods that increase the sample size and reduce instability σ_ν. The sample size N of a long duration measurement is the product of the number of detected atoms N_D each cycle and the number of cycles completed: $N = N_D\tau/\mathcal{T}$. The instability σ_ν limit depicted in (1.1 and 1.2) presents the sample size contributions of cycle time and atom number separately.

The natural variance in frequency of an optical transition (or any system) doesn't reduce over time or with more samples. Reduction of measurement error $\varepsilon(A)$ benefits from more measurement cycles (time) and increased sample size, as long as the experimental settings remaining static or well known. Figure 1.2 displays this behavior diagrammatically for frequency measurements of the clock transition.

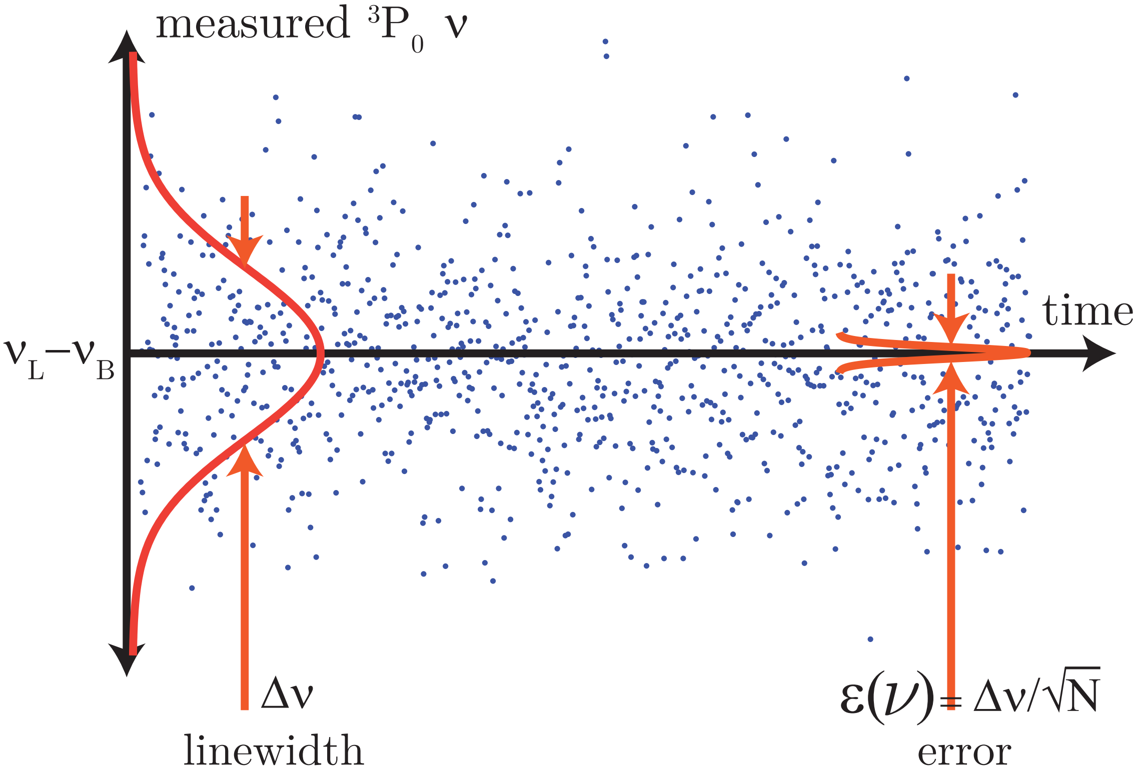

Figure 1.2: **Statistical Error Reduction in Optical Frequency Standards** Diagrammatic example of the statistical reduction to error $^{\Delta\nu}/_{\sqrt{N}}$ through increased sample number N from an initial statistical width $\Delta\nu$. Each dot represents a single frequency measurement, and the total number of dots displayed is the total measurement number N.

1.2 Precision Time Metrology

Precision time metrology is really precision frequency metrology. A clock is a time-keeping system composed of two essential components: an oscillator and a oscillation counter. A grandfather clock's pendulum is its oscillator, and the gears which move with each pendulum swing to advance the clock hands are oscillation counters. In an optical atomic clock, the oscillator is the transition between two atomic energy levels that has a characteristic transition frequency. The oscillation counter is a measurement of a laser's frequency when that laser has been brought into resonance with the chosen atomic transition. Absolute measurements of laser frequency in OFSs can be performed by frequency combs [50] and relative frequency measurements can be performed between two different OFSs [44].

The oscillator component of an atomic clock is the focus of this dissertation. Atoms are optimal oscillators because of the stability of their electronic levels, a stability so robust we use it do define our second. A microwave transition in the hyperfine structure of Cs is the oscillator that defines our second, where an external resonator that comes into resonance with that transition is defined to have 9,192,631,770 Hz frequency. The invariance of atoms' electronic levels is underpinned by Einstein's Equivalence Principle (EEP), where the presumed, absolute stability of the fine-structure constant α renders all atoms of a common species and isotope identical. Experimentally measured features in one atom should be exactly reproducible for all atoms of matching species and isotope. The utility of this premise is powerfully realized in group II type atoms which contain a desirable optical clock transition. The so-called "clock transition" is between the ${}^1S_0$ ground state and the ${}^3P_0$ clock state, shown in Figure 1.1. Appendix A contains a discussion of the "${}^3P_0$" notation and other nomenclature conventions in OFS. An explanation of why this clock transition has ideal properties for a frequency standard can be found in Chapter II.

We evaluate the group II type atoms Be, Mg, Ca, Sr, Ba, Hg, Yb, and Ra for their

Table 1.1: System stabilities $\mathcal{S}$ and realized instabilities σ_ν
(**bold** denotes predicted values)

System	$\mathcal{S}\,[\sqrt{\mathrm{Hz}^{-1}}]$	σ_ν
$\mathrm{Hg}_{2\gamma}$	$\mathbf{3.2 \times 10^{-15}}$	
Sr[8]	3.1×10^{-16}	6.4×10^{-18}
Yb [23]	3.2×10^{-16}	1.6×10^{-18}
Al^+ [12, 10]	3.7×10^{-16}	8.6×10^{-18}
Rb [51]	1.6×10^{-14}	6.5×10^{-16}
Cs [27]	2×10^{-13}	5×10^{-16}
Quartz	10^{-7}	
Chronometer	$10^{0.5}$	

suitability in a hot E1-M1 optical frequency standard. Atoms with the ${}^1S_0 \to {}^3P_0$ clock transition are referred to as clock atoms.

An attainable instability (accuracy) of a frequency standard depends on the same features that determine accuracy in any measurement system: the sample size and the natural precision (narrow linewidth) of the measurement. Sample size can be increased either by addressing a larger sample or through prolonged measurement. This is why $\mathcal{S}$ is a valuable comparison metric: in principle any system can achieve arbitrarily small instability σ_ν with infinite measurement time τ, but in practice it is difficult to maintain system stability for long durations of time. The best optical clocks in the world can cite stabilities that would maintain second accuracy for 5 billion years, but these claims defy verification. In fact, as one can readily calculate from the attained instabilities in current OFSs [23, 8], these systems are operating for less than 24 hours. Even though these systems are not operating for long durations yet, achieving instability quickly (i.e. having small $\mathcal{S}$) is useful for contemporary measurements and an attractive property in an OFS. This is accomplished in OFSs by reducing the intrinsic variance (the linewidth $\Delta\nu$) through experimental control of broadening mechanisms and by increasing the number of interrogated atoms N_{tot}.

1.3 Research

This dissertation outlines the fundamental physics of an E1-M1 optical clock transition and finds that neutral Hg in a hot vapor cell is the optimal system for a portable degenerate two-photon clock. While pursuing direct detection of the E1-M1 clock transition in neutral Hg, I also worked to characterize thoroughly the environmental and intrinsic factors of group II type atoms to compare the different systems and estimate the viability of each as an OFS. This dissertation describes in detail the parameter space needed to detect the E1-M1 transition in a hot vapor cell and calculates the potential stability $\mathcal{S}$. These calculations show that a hot monochromatic E1-M1 Hg clock has the capacity for very small $\mathcal{S}$ and could fill the currently empty niche of a portable optical frequency standard.

1.4 Applications

Should the estimated stability of this proposed monochromatic E1-M1 clock be realized, it could be the basis for a portable optical frequency standard. We predict that the stability $\mathcal{S}$ could be as low as $3.1 \times 10^{-15}\ \sqrt{\mathrm{Hz}^{-1}}$ in a vapor cell operating at 380 K . This is nearly as good as lattice and ion optical clocks (see Table 1.1), but importantly it is much better than the current crop of portable clocks [18, 29].

Portable frequency combs have 1×10^{-18} frequency sensitivity [15] and can easily measure the PHz frequencies of optical clock transitions with a resolution that exceeds the effective and natural linewidth of those transitions.[1] A frequency comb is one type of reference that could perform the oscillation counting required for a precise clock measurement.

When an optical frequency standard achieves an instability $\sigma_\nu = 1.1 \times 10^{-16}$, it becomes a gravitational redshift meterstick. Such an OFS is sensitive to changes in

---

[1] The PHz frequencies can be precisely measured because they are produced from IR wavelengths that can be measured with these combs.

altitude Δh on earth of one meter. The Δh sensitivity of a clock scales linearly with instability, so the Yb lattice clock ($\sigma_\nu = 1.6 \times 10^{-18}$) could resolve 1.5 cm after the requisite $\tau = 7$ hours of measurement time at each elevation. A remarkable local redshift measurement was performed in 2010 with an Al$^+$ OFS [10] where an elevation shift of 33 cm was measured through an observed offset in resonant laser frequency. However, these systems take "local" measurement too seriously, the state preparation and environment control to make the clock atoms ultracold and mitigate other environmental broadening requires equipment that easily fills an entire laboratory and prohibits portability of the clock. While the estimated stability of our monochromatic E1-M1 Hg OFS is not as precise as ultracold OFSs, it could achieve meterstick sensitivity in 14 minutes and do so in a portable package making it a useful metrology tool.

1.5 Thesis at a glance

Since readers of this dissertation will certainly come from different backgrounds, I include some tailored summaries with reading suggestions here. If you are reading this digitally you will find that the section (§), figure, and table numbers are hyperlink enabled.

The central claim of this dissertation is that a hot Hg E1-M1 optical frequency standard is viable and has several advantages. This dissertation aspires to explain why the proposed system should be hot (5.6), why it should be Hg (Table 5.2), why it should be an E1-M1 transition (2.1), what an optical frequency standard is (2.2), why it is viable (5.7), and includes explanation of the claim that this system is advantageous (8.2).

For the casual reader, the broad synopsis of this work is discussed at the start of this chapter (I). Performing this research required building the most powerful clock laser in the world, easily powerful enough to toast a marshmallow or be mistaken for a light saber. This green laser is about 1000 times more powerful than a common laser pointer. I have such fine frequency control over the laser that I can illuminate a vapor cell of Iodine molecules brightly enough to be seen by the human eye, see Figure 7.5.

For a clock scientist, the stability $\mathcal{S}$ estimates for the monochromatic E1-M1 scheme are listed for group II type atoms in Table 5.2. You can compare these stabilities to other optical frequency standards in Table 8.1.

For an experimental atomic physicist, the laser system we built for this experiment was robust and simple to assemble. The main virtue of this system was our ability to implement a single-pass Second Harmonic Generation (SHG) scheme in a periodically poled crystal with 23% single-pass efficiency.

For the reader interested in the dynamic behavior of monochromatic E1-M1 optical excitation in a thermal environment, the calculation results displayed in the figures and tables of Chapter V show the excitation rate $\dot{N}_D$ and stability $\mathcal{S}$ behavior for each group II type atom. This is calculated for the dynamic parameters of laser-beam radius ω_0 and vapor cell temperature T.

A summary of this dissertation is as follows:

Chapter I describes the history and current research of precision measurements using atomic systems. It also defines the comparison metric stability $\mathcal{S}$ used to compare optical frequency standards.

Chapter II explains the underlying theory of light-matter interaction as it applies to using lasers for excitation of clock atoms. The essential properties of clock lasers and clock atoms are described in terms of their optical properties. I present the two-photon Rabi frequency $\Omega_{R2\gamma}$ (2.3) and probability of optical transition $P_{^3P_0}$ (2.4) for the E1-M1 type transition.

Chapter III details the experimental environment's impact on the interrogation rate $\dot{N}_{tot}$ (3.10) of vapor cell atoms for a monochromatic E1-M1 excitation scheme. Experimental parameters that can be optimized independently (such as laser power) and parameters with interdependency (such as temperature and laser-beam radius) are outlined. Prototypical experimental values are listed (Table 3.1) and detection channels are briefly described.

Chapter IV also details the experimental environment of the atoms, but this time to explain how those features impact a precision optical frequency measurement in terms of line broadening $\Delta\nu$ (4.1) and frequency shifts ν_B (4.2).

Chapter V contains the calculation results for monochromatic E1-M1 detection rate $\dot{N}_D$ and stability $\mathcal{S}$ of the group II type atoms in a hot vapor cell. This calculation is performed with respect to two dynamic parameters: laser-beam radius ω_0 and vapor cell temperature T. Contour plots of $\dot{N}_D$ and $\mathcal{S}$ across these dynamic parameter spaces are included. Properties of the system at the optimized temperature T and laser-beam radius ω_0 are included for each atomic species.

Chapter VI explores the bichromatic variation of an E1-M1 optical clock. The bichromatic method introduces an opportunity to compensate for systematic frequency shifts ν_B and produce an optical frequency standard that measures the true natural frequency ν_0 (4.2) of the atomic transition.

Chapter VII describes the experimental progress performed toward observing a monochromatic E1-M1 optical transition in neutral Hg. A high-power narrow-linewidth laser system was built (Section 7.4) and an efficient detection imaging scheme was designed and assembled (Section 7.5).

I conclude in Chapter VIII with a summary the E1-M1 optical transition theory developed here and calculation results. I compare the predicted stabilities $\mathcal{S}$ of the monochromatic E1-M1 scheme with current, state-of-the-art optical frequency standards (Table 8.1).

I've included two appendices:

Appendix A explains the Russell-Saunders notation that is commonly used in this dissertation. I also detail some of the confusing and contradictory vernacular conventions used to describe optical frequency measurements.

Appendix B makes explicit our treatment of the (already simplified) three-level clock system as an effective two-level system through adiabatic elimination of the intermediate level.

CHAPTER II

Optical Transition Theory

The optical transition properties of group II type atoms underpin their viability as optical frequency standards. The favorable properties of the forbidden ${}^1S_0 \rightarrow {}^3P_0$ clock transition will be discussed in this chapter. The clock level excitation probability for a single atom in an E1-M1 scheme will be presented. Figure 2.1 illustrates an example of the E1-M1 excitation scheme in a vapor cell.

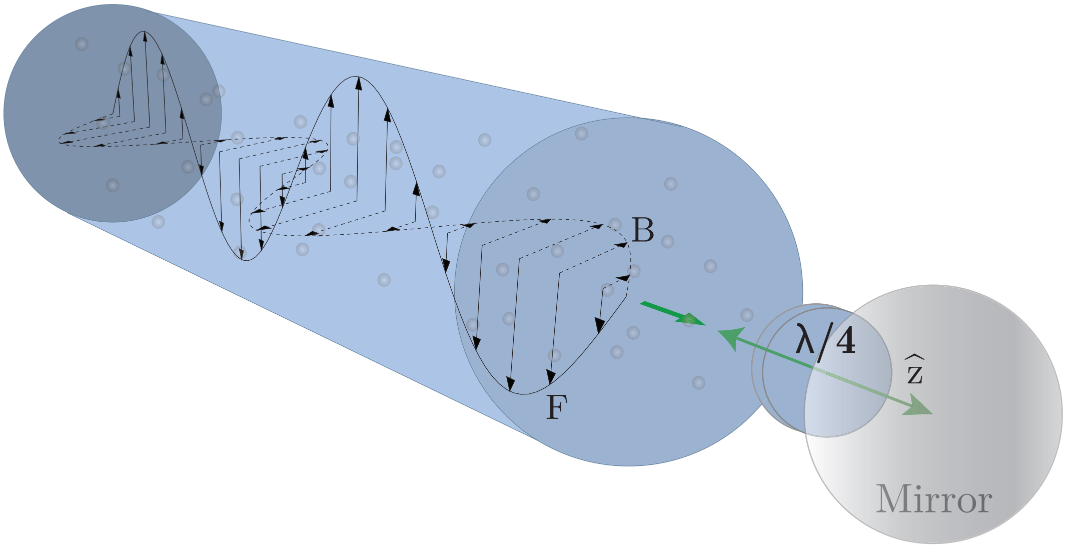

Figure 2.1: **Hot Optical Clock** To satisfy the selection rules of the transition, the counter-propagating laser must rotate polarization by 90-degrees. This can be accomplished with a $\lambda/4$-plate and a retro-reflection mirror. The orthogonal electric F and magnetic B fields are shown.

2.1 Forbidden Transitions

The challenge for optical atomic clocks it to both preserve and overcome forbidden transitions between atomic levels. Forbidden transitions create metastable states whose long lifetimes are ideal for clock levels. Forbidden transitions also make optical access to these clock levels difficult which is problematic for performing resonant frequency measurements. Our clock scheme preserves the metastability of the clock level while making the "forbidden" level optically accessible. This feature is unlike the one-photon direct excitation technique used in other optical frequency standards.

Forbidden transitions are disallowed for electric and magnetic coupling because they don't satisfy certain selection rules of quantum mechanics. By contrast, allowed transitions in an atom can take place with electric or magnetic coupling and can be dipole or multipole. Those allowed transitions permit excitation between levels that have been defined by spin (S), orbit (L), and spin-orbit (J) coupling. See Appendix A.1 for how the specific quantization of these features is represented in the level structure notation.

Where an atomic level is well defined by the S, L, and J quantum numbers, then an electric- or magnetic-allowed transition indicates that a quantized change to those quantum numbers has occurred. Electric-dipole (E1) transitions are typically much stronger than magnetic-dipole (M1) transitions.

A forbidden transition is desirable in a clock because the forbidden relaxation to the ground state from a clock state renders that clock state metastable, which is to say that relaxation only occurs rarely. The long lifetime of these metastable clock levels is equivalent to a narrow-transition linewidth $\Delta\nu_{nat}$, which is a desirable feature in OFSs because the initially narrow linewidth immediately improves the frequency resolution and ultimately the $\mathcal{S}$ compared with standards based on broad linewidth transitions.

For illustration, in Hg the weakly E1-allowed ${}^1S_0 \overset{\text{E1}}{\longleftrightarrow} {}^3P_1$ transition has an 8

MHz linewidth $\Delta\nu_{nat}$. For a single resonance laser frequency observation of this ${}^3P_1$ transition there is a 99.99999% probability that the measurement will be more than 1 Hz away from the natural frequency ν_0. For the even more weakly E1-allowed ${}^1S_0 \overset{\mathrm{E1}}{\longleftrightarrow} {}^3P_0$ transition in Fermionic ^{201}Hg (with similar ν_0 to the ${}^3P_1$ level), the linewidth is 0.45 Hz, which means that there is only a 3% probability of measuring the resonance more than 1 Hz away from the natural frequency ν_0. A clock level (${}^3P_0$) has higher resolution than similar E1-allowed level (like ${}^3P_1$) in that the clock level requires a more precise frequency to successfully drive optical transitions, and this precision is virtuous in an OFS.

In common usage "forbidden" transition often refers only to an E1 forbidden transition. A pure ${}^1S_0 \rightarrow {}^3P_0$ clock transition is not only E1 forbidden, it is doubly forbidden by all transition types because it is $J_{initial} = 0 \leftrightarrow J_{final} = 0$ and $S_{initial} = 0 \leftrightarrow S_{final} = 1$. The highly forbidden transition found in group II type atoms between the ground state ${}^1S_0$ and the metastable ${}^3P_0$ clock level is an ideal oscillator for OFSs because it has vanishingly small natural linewidth $\Delta\nu_{nat}$.

In reality, however, no levels are pristinely defined by spin features alone and so "forbidden" transitions can be allowed. The extent to which a forbidden transition is in fact allowed depends on mitigating interactions with nearby allowed levels. In fact, all current optical frequency clocks directly drive the "forbidden" ${}^1S_0 \rightarrow {}^3P_0$ transition with a one-photon, E1 transition. This is possible because the ${}^3P_0$ level mixes with the nearby ${}^3P_1$ level, which has a weakly E1-allowed transition to the ${}^1S_0$ ground state. This mixing can be done by selecting isotopes with hyperfine structure [10] or by applying a magnetic field [2]. Fermionic isotopes of group II type atoms possess nuclear spin which creates hyperfine-induced state mixing between the ${}^3P_0$ and the ${}^3P_1$ levels. While mixing the levels is necessary to make them electric dipole coupled, it also reduces the lifetime. This can potentially limit the ultimate precision of the clock. The ${}^1S_0 \overset{\mathrm{E1}}{\longleftrightarrow} {}^3P_1$ transition is E1 forbidden by the spin selection rule

($\Delta S = 0$ is not E1 allowed), but is effectively allowed through the spin-orbit coupling of the ${}^3P_1$ and ${}^1P_1$ levels. For an example of this effect in Hg see [33].

Our novel E1-M1 excitation scheme from the ${}^1S_0$ ground state into the metastable ${}^3P_0$ clock level is allowed and preserves the metastability of the level. We do this by driving a two-photon E1-M1 allowed transition that couples ${}^1S_0$ and ${}^3P_0$ through the intermediate ${}^3P_1$ level. Specifically, ${}^1S_0 \overset{\text{E1}}{\longleftrightarrow} {}^3P_1$ is a weakly allowed E1 transition and the ${}^3P_1 \overset{\text{M1}}{\longleftrightarrow} {}^3P_0$ is an allowed M1 transition. Using two photons whose total frequency matches the ${}^1S_0 \rightarrow {}^3P_0$ transition frequency, we can drive the clock transition using the electric and magnetic field components of a CW laser-beam. Driving the transition with degenerate photons introduces a large detuning Δ from the intermediate state, see Figure 1.1 for the frequency scale of Δ compared to the transition frequencies. This large Δ reduces the two-photon Rabi frequency (2.3) and therefore the overall excitation rate compared with a resonant, bichromatic system. The expected excitation probabilities are fortunately non-zero despite this detuning for group II type atoms.

Forbiddenness is claimed as a virtue primarily because it increases the natural quality factor Q of the frequency standard. Table 2.1 lists the natural Q's of individual group II type atoms. This table excludes the environmental perturbations introduced when a frequency measurement is performed. You can see that the 10^{18} frequency resolution found in frequency combs is in a useful resolution regime for OFSs [15].

2.2 Optical Clocks

The term "optical clock" refers to all atomic clocks that drive a ${}^1S_0 \rightarrow {}^3P_0$ clock transition, which is currently lattice and ion systems. The nomenclature refers to the shift in technology from microwave frequency standards (Rb and Cs) to the UV standards of today (Al+, Yb, and Sr). The dawn of atomic clocks in the mid-20th century came with the availability of coherent microwave sources. Frequency sources

Table 2.1: Natural Q of candidate E1-M1 clock atoms

System	Q = $\nu_0/2\Delta\nu_{nat}$
^{25}Mg [36]	1.9×10^{17}
^{87}Sr [56]	3.0×10^{16}
$^{\text{even}}$Sr	$> 3.0 \times 10^{16}$
^{199}Hg [36]	8.5×10^{14}
^{201}Hg [36]	1.2×10^{15}
$^{\text{even}}$Hg	$> 1.2 \times 10^{15}$
^{171}Yb [36]	3.8×10^{17}
^{173}Yb [36]	4.2×10^{17}
$^{\text{even}}$Yb	$> 4.2 \times 10^{17}$

today reach far into the UV and with them we have gained optical access to the PHz transition frequencies of today's OFSs. The term "optical" is also evocative of the spectrum of light in these systems which typically span the visible and UV wavelengths.

2.3 $^1S_0 \to {}^3P_0$ E1-M1 Transition

E1-M1 transition has been observed previously in highly charged ions [47, 28]. As an allowed transition, it provides optical access to all isotopes of group II type atoms. This excitation can be implemented using either degenerate (monochromatic) counter-propagating photons to eliminate first-order Doppler broadening or with non-degenerate (bichromatic) frequencies chosen to offset light shifts. The monochromatic scheme is the primary focus of this dissertation, but the bichromatic case is described in Chapter VI.

The viability of a hot clock will depend on the effective rate of detected atoms:

$$\dot{N}_D = P_D \times \dot{N}_{^3P_0} \tag{2.1}$$

where P_D is the probability of detecting an atom in the $^3P_0$ clock-level, and $\dot{N}_{^3P_0}$ is the effective rate of atoms excited to the clock level. The two primary experimental parameters with interdependency that require optimization are vapor cell temperature T and laser-beam radius ω_0. The effective rate of atoms excited to the $^3P_0$-level is given by:

$$\dot{N}_{^3P_0} = P_{^3P_0}(T, \omega_0) \times \dot{N}_{tot}(T, \omega_0) \tag{2.2}$$

where $P_{^3P_0}$ is the probability an individual atom in the interrogation region has been excited to the $^3P_0$ level and $\dot{N}_{tot}$ is the rate of atoms flowing through the interrogation region. The interrogation rate $\dot{N}_{tot}$ is discussed in Chapter III. The single-atom excitation probability $P_{^3P_0}$ is discussed in this chapter. In a thermal environment, the interrogation time of an atom by the excitation laser is always much less than the time required to coherently transfer the full population to the excited state (i.e. no risk of Rabi flopping). Therefore, an increase in laser power is always beneficial to $P_{^3P_0}$ because it increases the two-photon Rabi frequency $\Omega_{R2\gamma}$ and by extension the probability of excitation the the $^3P_0$-level in a time-limited measurement. The temperature T and laser-beam radius ω_0 contribution to the two-photon Rabi frequency $\Omega_{R2\gamma}$ will be explained in §2.4.

2.4 Two-Photon Rabi Frequency

E1-M1 excitation schemes can use either a single laser (monochromatic) or a pair of far-detuned lasers (bichromatic) to drive the clock transition. In both cases, the excitation laser frequencies are far off resonance from the intermediate $^3P_1$ level. To satisfy the selection rules of the transition, the electric-field vector of one excitation photon must be parallel to the magnetic-field vector of the other excitation photon.

This alignment can be realized utilizing either a Lin ⊥ Lin or σ^+/σ^- polarization scheme [14]. These schemes not only satisfy the selection rules, they ensure that any clock excitation is the product of counter-propagating beams and thus reduces or eliminates first-order Doppler broadening.

A far-detuned E1-M1 system (Δ is large) satisfies the constraints of adiabatic elimination [48, 9] described in detail in Appendix B. Specifically $\Delta >> \Omega_1, \Omega_2, \delta$ where Ω_i is the two-level Rabi frequency of each E1 and M1 transition, δ is the two-photon detuning from the light shifted transition frequency, and Δ is the minimum detuning of an excitation photon's energy from the intermediate ${}^3P_1$ level, see Figure B.1. In the limit where $\delta = 0$, the two-photon Rabi frequency for an atom addressed by a pair of photons is given by [38] :

$$\Omega_{R2\gamma} = \frac{2I}{\hbar^2 c^2 \epsilon_0} \frac{\langle {}^3P_0||\mu||{}^3P_1\rangle_{M1} \langle {}^3P_1||D||{}^1S_0\rangle_{E1}}{\Delta} \tag{2.3}$$

where I is the peak intensity of the excitation laser, $\langle {}^3P_0||\mu||{}^3P_1\rangle_{M1}$ is the reduced matrix element for the magnetic dipole (M1) transition, and $\langle {}^3P_1||D||{}^1S_0\rangle_{E1}$ is the reduced matrix element for the electric dipole (E1) transition.

In group II type atoms, the E1-M1 coupling will also occur via the ${}^1P_1$ intermediate level (see Figure 1.1). This is generally beneficial, and in the specific case of Hg it will constitute as much as 37% of the Rabi frequency (an effective increase). The ${}^1P_1$ contribution is maximum for the degenerate excitation scheme. We omit this favorable contribution from the $\Omega_{R2\gamma}$ calculations for simplicity, but experiments can anticipate an enhancement to rates $\dot{N}_D$ and stability $\mathcal{S}$. Observed and calculated reduced matrix elements are shown for the group II type atoms in Table 2.2. Additionally, the calculated two-photon Rabi frequency is listed for the degenerate two-photon case assuming the experimental parameters defined in Table 3.1. For

Table 2.2: Reduced matrix elements for the electric-dipole $\langle nsnp^3P_1||\mathbf{D}||ns^2\,{}^1S_0\rangle$ intercombination transition (E1) and the magnetic-dipole $\langle nsnp^3P_0||\boldsymbol{\mu}||nsnp^3P_1\rangle$ transition (M1) for each candidate element. Matrix element values are in a.u. For monochromatic excitation, the two-photon Rabi frequency $\Omega_{R2\gamma}$ is shown for unit intensity. A prototypical intensity for this scheme is $6 \times 10^6 [W/m^2]$.

Atom	n	$\mathrm{E1}/ea_0$	$\mathrm{M1}/\mu_B$	$\Omega_{R2\gamma}/I[Hz]$
Ra	7	1.2 [6]	$\sqrt{2}$ [13]	7.1×10^{-5}
Ba	6	0.45 [17]	$\sqrt{2}$ [13]	3×10^{-5}
Yb	6	0.54 [4]	$\sqrt{2}$ [4]	2.5×10^{-5}
Hg	6	0.44 [30]	$\sqrt{2}$ [13]	9.3×10^{-6}
Sr	5	0.15 [42]	$\sqrt{2}$ [13]	8.8×10^{-6}
Ca	4	0.036 [42]	$\sqrt{2}$ [13]	2×10^{-6}
Mg	3	0.0057 [42]	$\sqrt{2}$ [30]	2.2×10^{-7}
Be	2	0.00024 [30]	$\sqrt{2}$ [13]	9.3×10^{-9}

excitation intensity of 6×10^6 [W/m^2], the two-photon Rabi frequencies $\Omega_{R2\gamma}$ have greater than Hz magnitudes in most group II type atoms. This illustrates the viability of an E1-M1 excitation scheme.

2.5 Probability of Clock Excitation

With adiabatic elimination of the intermediate level (see Appendix B) we find the probability of exciting the atom into the ${}^3P_0$ clock level in this effective two-level system [48, 9, 43] is given by

$$P_{{}^3P_0}(T, \omega_0) = \frac{\Omega^2_{R2\gamma}}{\Omega^2_{R2\gamma} + \delta^2} \sin^2\left(\frac{\sqrt{\Omega^2_{R2\gamma} + \delta^2}}{2}\bar{t}\right) \tag{2.4}$$

where $\bar{t}$ is the average interrogation time of the atoms and δ is the two-photon detuning from the light-shifted resonant frequency ν_0.

In our calculation of the E1-M1 system, we report excitation probability of a single frequency measurement. To capture the reduction to signal from effective line broadening, the single frequency we use is detuned from resonance by the characteristic width of the first-order Doppler broadening ($\Delta\nu_{D1}$). This detuning δ from first-order

Doppler broadening $\Delta\nu_{D1}$ is much larger than the two-photon Rabi frequency $\Omega_{R2\gamma}$. See §4.1.4 for a discussion of Doppler effects. In this small $\Omega_{R2\gamma}$ limit, the excitation probability $P_{^3P_0}$ has two characteristic regimes. There is a time-limited regime, where transit-time (time-of-flight) broadening ($\Delta\nu_{_{TT}} = 1/\bar{t}$) is the dominant scaling feature of the excitation probability. Transit-time broadening dominates our system when $\Delta\nu_{_{TT}} >> \Delta\nu_{D1}$. The time-limited probability of excitation then scales quadratically in time as

$$P_{^3P_0} \approx \left(\frac{\Omega_{R2\gamma}\bar{t}_B}{2}\right)^2. \tag{2.5}$$

In this regime, experimental optimization that increases the time-in-beam is useful.

In a velocity-limited regime where $\Delta\nu_{D1} >> \Delta\nu_{_{TT}}$, the probability of clock excitation resembles a saturated system and can be simplified as:

$$P_{^3P_0}(T, \omega_0) \approx \frac{\Omega^2_{R2\gamma}}{\delta^2}. \tag{2.6}$$

In this regime, experimental optimization that decreases velocity broadening is important.

CHAPTER III

Atomic Environment and Excitation Rates

The unavoidable interaction of clock atoms with the experimental environment affects the sample size of addressed atoms N. In this chapter the nuanced interaction between vapor cell temperature T and laser-beam radius ω_0 is explored and characterized toward optimizing excitation rates $\dot{N}_{^3P_0}$ and stability $\mathcal{S}$. The previous chapter described the optical transition probability of a single atom, this chapter describes the ensemble behavior of the clock atoms in a hot vapor cell.

3.1 Static Experimental Parameters

Most experimental parameters can be optimized independently. Table 3.1 lists the static magnitudes we will assume for these independent experimental parameters. The magnitudes were conservatively selected to match existing or easily attainable levels. Importantly, these experimental magnitudes can be constructed in a portable package which will permit mobile optical frequency measurements.

We estimate that narrow-linewidth power can be achieved at approximately the 10 W level. We have generated 8 W of portable, narrow-linewidth light for a monochromatic Hg experiment in a preliminary device and estimate that more power is possible while preserving this portability, see Chapter VII for details of this system. The laser power required to excite the E1-M1 transition will contribute a sizable light shift

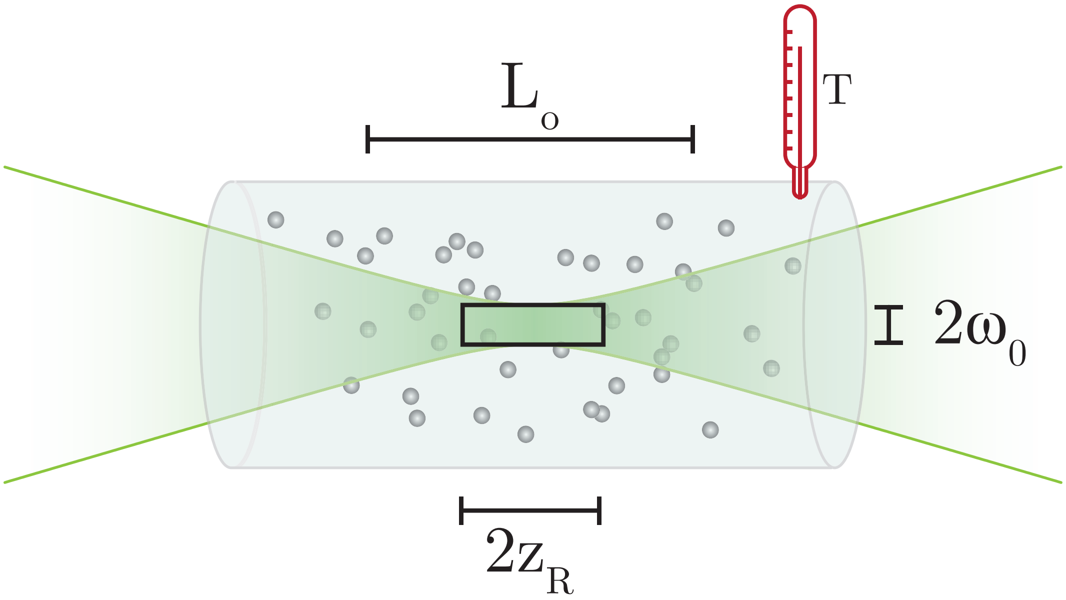

Figure 3.1: **Hot Optical Clock** This diagram of a monochromatic laser in a vapor cell depicts the experimental system. The detection length is L_o and the laser-beam radius is ω_0. The Rayleigh range, $2z_R$, that limits the interrogation region is shown in this graphic. The area enclosed by a box is the interrogation region of the atoms and in this case is Rayleigh-limited.

(ν_{LS}), but one that can be effectively quantified and eliminated in analysis. The light shift is discussed in terms of stability $\mathcal{S}$ impact in §4.1.3.

All group II type atoms, with the exception of Hg, improve in overall excitation rate $\dot{N}_D$ and stability $\mathcal{S}$ with increased temperature because atom-atom interactions are minimal. Since number density ρ increases exponentially with temperature, it was necessary to impose in our calculations a temperature ceiling of 800 K as a damage threshold for the physical optics and detectors of an experimental apparatus.

The physical size of the photon detector and imaging optics create an aperture and depth of field which impose boundaries on the observable volume of the vapor cell by the detection system. We are not limited by the depth of field in this experiment due to the small radius of the excitation laser beam. The length of excitation laser beam that we can observe is limited by the aperture of our detection system. In our Hg experiment we used a detector with a 2 cm active diameter (MP1941), the implementation of a 1:1 imaging system permits a detection length limit L_o of 2 cm in the vapor cell. Figure 3.1 displays the detection length L_o in relation to other experimental geometry parameters.

Misalignment of the counterpropagating laser-beams by an angle θ is anticipated. Figure 3.2 illustrates an exaggerated misalignment in our proposed experimental geometry. We impose a 0.1 milliradian limit in our simulation which has been previously

Table 3.1: Experimental parameters used for the simulation of a hot, vapor cell E1-M1 optical clock.

Parameter	Value
Power (CW)	10 W
Laser Linewidth	1 kHz
Retroreflection Misalignment θ	0.1 milliradian
Photon Collection Efficiency P_{pc}	1 %
Optical Damage Threshold	800 K
Temperature Instability $\sigma_{\bar{T}}$	0.1 K
Optical Detection Length L_o	2 cm
Experiment Period $\mathcal{T}$	1 s

realized in atom interferometry experiments [22]. In our experimental setup we estimated an alignment precision of 0.2 milliradians (see §7.3). Increased precision of alignment will improve both the rates $\dot{N}_D$ and the stability $\mathcal{S}$ by reducing residual first-order Doppler broadening $\Delta\nu_{D1}$ (see §4.1.4.1). We do not include a threshold for polarization rotation errors in this calculation although such experimental features will degrade the rates $\dot{N}$ and stability $\mathcal{S}$ of the experiment.

Since the experiment takes place at the beam waist of the laser, the atoms will experience the spatially dependent Gouy phase shift. This was not included in our calculations.

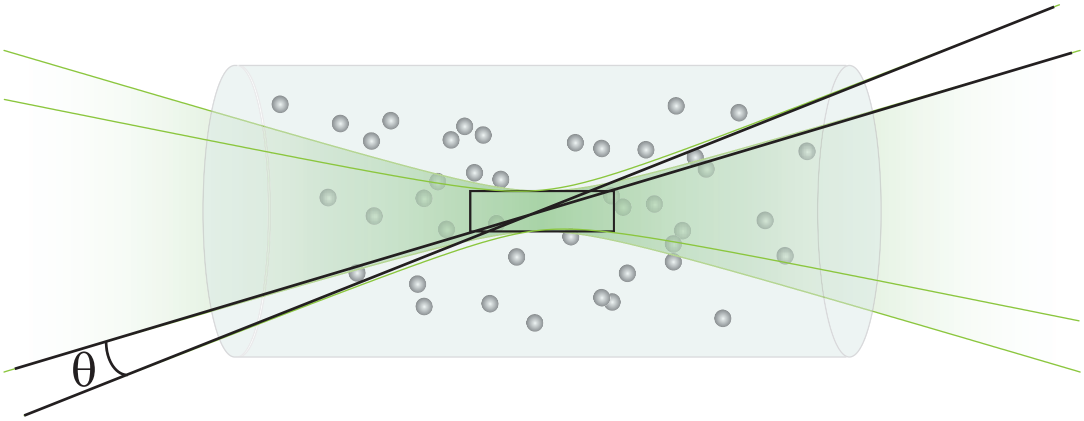

Figure 3.2: **Alignment Angle $\boldsymbol{\theta}$** The misalignment of a retroreflected laser beam from the input beam by an angle θ is illustrated.

An optical frequency standard will necessarily limit itself to a single atomic isotope. The natural abundance of the excluded isotopes will attenuate the excitation rates $\dot{N}_{^3P_0}$ because our calculations are based on total atomic number density ρ which includes all isotopes. Since isotope abundance is idiosyncratic to each atomic species, our calculations do not include the reduction to the number density ρ that will be present in an experiment.

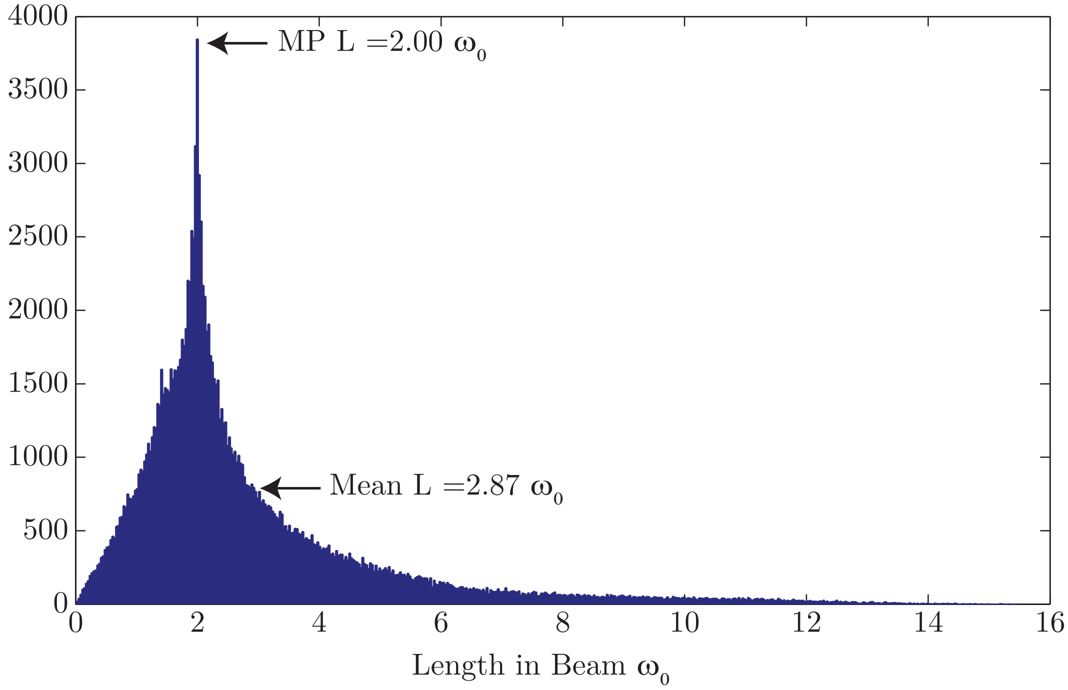

Figure 3.3: **Simulation of Length in laser-beam** Histogram of 160k Atoms' Travel Length in Cylinder with Radius ω_0

3.2 Spatial Approximation Length in Beam $\bar{l}$

The probability of exciting an atom from the ground state to the clock state depends on the amount of time an atom spends in the beam. Statistically characterizing hot atom trajectories in a laser-beam is important to accurately predict excitation rates in the experiment. For a region defined by a cylinder with radius ω_0 we can numerically calculate the average distance an ensemble of isotropically oriented atoms travels through such a cylinder. Since not all atoms will pass through the center of the beam, we take care to initialize the atoms at a variety of initial distances from the beam center. Results from this simulation are shown in Figure 3.3.

Numerical simulation reveals that the average length in beam is $2.87 \times \omega_0$ and the most probable length is $2.00 \times \omega_0$. We extrapolate from these results that the beam diameter is a valid approximation for the average length traveled by an atom in the laser beam ($\bar{l} = 2\omega_0$).

To increase $P_{^3P_0}$, it is ideal for atoms to spend as much time in the beam $\bar{t}$ as possible. A first-order consideration of this system suggests that the optimal atom path is co-linear with the laser-beam because that will enhance time in beam (we define this orientation as the $\hat{z}$-direction, see Figure 2.1). For contrast, a suboptimal path would glance across the edge of the excitation region. However, length in beam is not the only experimental contribution atoms make. The experimental geometry will effectively post-select atoms that travel along the $\hat{z}$-direction because such atoms will have a comparatively enhanced $P_{^3P_0}$. This post-selection also favors atoms with enhanced velocity in the $\hat{z}$-direction. A plot of this v_z enhancement is shown in Figure 3.4. This is a noteworthy bias because first-order Doppler broadening $\Delta\nu_{D1}$ effects (see §4.1.4.1) are created by atoms with velocity in the $\hat{z}$-direction. Our simulation only considers average length in beam, so the effect of this bias is not captured in our linewidth $\Delta\nu_{D1}$ calculations although it will introduce broadening in a experimental measurement.

3.3 Dynamic Experimental Parameters Vapor Cell Temperature T and Laser-Beam Radius ω_0

While many experimental parameters can be optimized independently, the interdependency of vapor cell temperature T and laser-beam radius ω_0 requires careful attention. It is convenient to numerically calculate the excitation rate $\dot{N}_D$ and stability $\mathcal{S}$ across a grid of temperatures and laser-beam radii. The resulting dependence of $\dot{N}_D$ and $\mathcal{S}$ on T and ω_0 are presented as a series of figures in Chapter V. Using thermal atoms instead of ultracold atoms increases the density and interrogation rate, a statistical advantage for optical frequency standards. A disadvantage for thermal

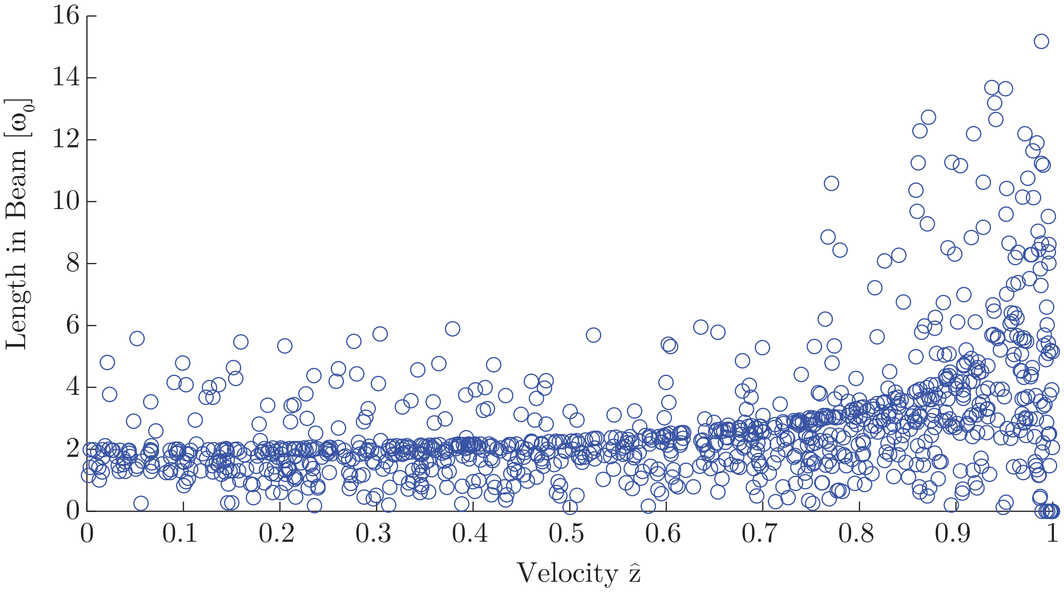

Figure 3.4: **Simulation of $\hat{v}_z$ Bias** 1000 atoms $\hat{v}_z$-component of $\hat{v}$ with respect to length in beam ω_0

atoms is atomic-mass-dependent thermal speed which both limits interrogation to the transit time $\bar{t}$ of the atom and introduces sensitivity to Doppler effects ($\Delta\nu_{D1}$ and $\Delta\nu_{D2}$). Unencumbered motion also leads to non-zero atom-atom collision probability.

The interrogation time $\bar{t}$ is the average time atoms spend passing through the excitation region, illustrated in Figure 3.1. This is the volume of the laser-beam enclosed by the Gaussian laser-beam radius ω_0 and length of the excitation region. From the calculations described in §3.2 we find that the beam diameter ($2\omega_0$) is a reasonable approximation of the average distance $\bar{l}$ an atom travels through the interrogation region. The mean thermal velocity $\bar{v}$ of an atom in the vapor cell depends on the vapor cell temperature T. The interrogation time scales with temperature T and laser-beam radius ω_0 as

$$\bar{t} = \frac{\bar{l}}{\bar{v}} = 2\omega_0 \times \sqrt{\frac{\pi M}{8k_BT}} \tag{3.1}$$

where k_B is Boltzmann's constant and M is the mass of the atom. Heavier atoms

Table 3.2: Mass and natural optical transition frequency ν_0 for each candidate element. The specific wavelength for the monochromatic excitation scheme, $\lambda_{2\gamma}$, is also listed. Citations are included when the clock transition has been experimentally observed.

Atom		m [amu]	ν_0 [Hz]	$\lambda_{2\gamma}$ [nm]
Hg	[35]	200.6	1.1×10^{15}	531
Be		9.1	6.6×10^{14}	910
Mg		24.3	6.6×10^{14}	915
Yb	[24]	173.1	5.2×10^{14}	1157
Ca		40.1	4.5×10^{14}	1319
Sr	[32]	87.6	4.3×10^{14}	1397
Ra		226.0	3.9×10^{14}	1529
Ba		137.3	3.7×10^{14}	1631

Table 3.3: Relative Time in Beam

Atom	$t_B(T, \omega_0)[s]$
Ra	$0.21\frac{\omega_0}{\sqrt{T}}$
Hg	$0.19\frac{\omega_0}{\sqrt{T}}$
Yb	$0.18\frac{\omega_0}{\sqrt{T}}$
Ba	$0.16\frac{\omega_0}{\sqrt{T}}$
Sr	$0.13\frac{\omega_0}{\sqrt{T}}$
Ca	$0.087\frac{\omega_0}{\sqrt{T}}$
Mg	$0.068\frac{\omega_0}{\sqrt{T}}$
Be	$0.041\frac{\omega_0}{\sqrt{T}}$

move more slowly than light atoms, and so enjoy longer interrogation times for a given temperature T. Longer interrogation time $\bar{t}$ enhances probability of clock excitation $P_{^3P_0}$ (2.4). The mass of each candidate atom is shown in Table 3.2 and the relative time in beam $\bar{t}$ with respect to temperature T is shown in Table 3.3.

For the degenerate (monochromatic) excitation case, mirror misalignment introduces first-order Doppler broadening $\Delta\nu_{D1}$ to atoms with velocity $\mathbf{v}$ components co-linear with the laser beam's wavevector $\mathbf{k}$ ($\mathbf{v} \cdot \mathbf{k} \neq 0$). This inhomogeneous broadening introduces an effective detuning δ to each atom from the natural transition frequency and diminishes the probability of clock excitation $P_{^3P_0}$ (2.4). This broadening is included in our calculations as a constant detuning magnitude equivalent to the mean velocity $\bar{v}$:

$$\Delta\nu_{D1}(T,\theta) = \frac{k}{2\pi}\bar{v}(T)\sin(\theta) \tag{3.2}$$

where k is the wavenumber. The specific detuning $\Delta\nu_{D1}$ for the mean velocity of each atomic species with respect to vapor cell temperature and misalignment is listed in Table 3.4. Figure 3.5 illustrates in Ra the interplay between single-atom excitation probability and the number density ρ, both shown with respect to effective detuning in 1 kHz bins. The correct calculation of total transition rate is the convolution of these two distributions. We find that a single frequency excitation probability where that single frequency is one detuned from resonance by the effective width of the residual Doppler broadening, the resulting transition rate is a good approximation of a convolved solution.

Typical experimental parameters (Table 3.1) result in broadening of 10-100 kHz for the candidate group II type atoms. This can be compared to the estimated natural linewidth of 0.45 Hz for neutral ^{201}Hg [36].

Table 3.4: Residual 1st-order Doppler broadening in an E1-M1 scheme introduced by mirror misalignment θ. The milliradian misalignment threshold makes the small angle approximation valid.

Atom	$\Delta\nu_{D1}(T$ [K],θ[rad]) [Hz]
Ra	$6.3 \times 10^6\sqrt{T} \times \theta$
Ba	$7.6 \times 10^6\sqrt{T} \times \theta$
Yb	$9.6 \times 10^6\sqrt{T} \times \theta$
Sr	$1.1 \times 10^7\sqrt{T} \times \theta$
Ca	$1.7 \times 10^7\sqrt{T} \times \theta$
Hg	$1.9 \times 10^7\sqrt{T} \times \theta$
Mg	$3.2 \times 10^7\sqrt{T} \times \theta$
Be	$5.3 \times 10^7\sqrt{T} \times \theta$

The total atom interrogation rate $\dot{N}_{tot}$ depends on the interrogation volume. The volume of the interrogation region is limited either by the Rayleigh range or the detection optics. Figure 3.1 depicts the Rayleigh range $2z_R$ and the detection length

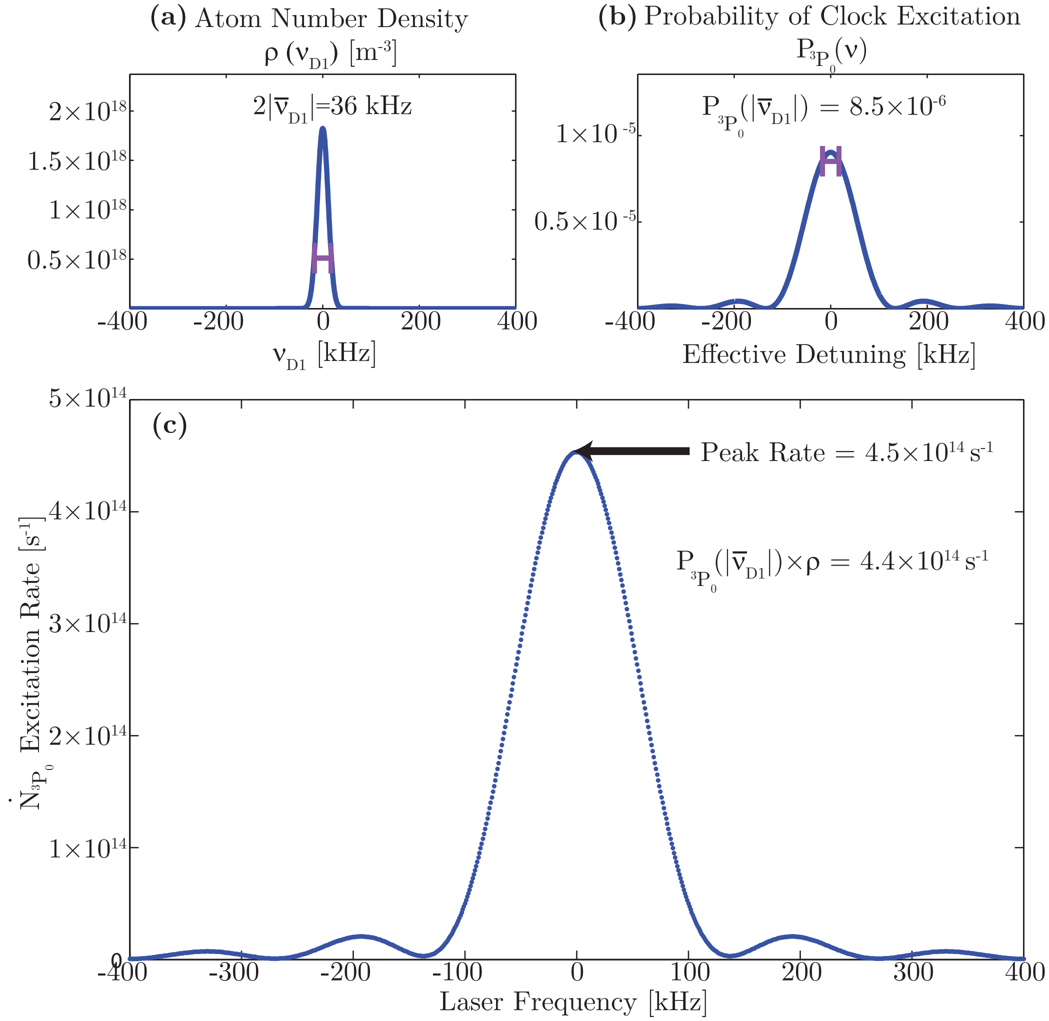

Figure 3.5: **Excitation Probability for Thermal Distribution** Simulation of Doppler effects and transition probability for neutral Ra in a monochromatic E1-M1 scheme. This assumes the experimental settings of Table 3.1, vapor cell temperature $T = 800$ K, and laser beam radius $\omega_0 = 6.3$ mm. (a) Plot of neutral Ra's number density with respect to effective resonance frequency due to first-order Doppler broadening ν_{D1}. The thermal distribution of velocities (for this simulation $T = 800$ K) manifests as effective frequency shifts. The number density amplitudes are for 1 kHz frequency bins. The width of the $2\nu_{D1}$ is measured by a purple ruler. (b) Plot of a single Ra atom's excitation probability with respect to the laser's detuning from the atom's effective resonance frequency. The probability of excitation at the mean velocity shift $\bar{\nu}_{D1}$ is reported and the $2\nu_{D1}$ width is marked (again in purple). (c) A laser scan across the natural resonance of a transition would produce the convolution of the first-order Doppler frequency distribution and the excitation probability, this is modeled in (c). Our approximation for peak probability of excitation is close in magnitude to the actual peak rate count from a convolution.

L_o in a vapor cell setup. When the volume is limited by detection optics V_{L_o} the volume of addressed atoms is the laser-beam area multiplied by the detection length L_o

$$\begin{aligned} V_{L_o} &= L_o \times \pi\omega_0^2 &(3.3)\\ V_{L_o}(\omega_0) &\propto \omega_0^2 &(3.4)\end{aligned}$$

where L_o is an experimental constraint unrelated to the laser-beam radius ω_0.

In the Rayleigh range limit the volume V_{z_R} is given by:

$$\begin{aligned} V_{z_R} &= 2z_R \times \pi\omega_0^2 &(3.5)\\ &= \frac{2\pi\omega_0^2}{\lambda} \times \pi\omega_0^2 &(3.6)\\ V_{z_R}(\omega_0) &\propto \omega_0^4 &(3.7)\end{aligned}$$

where the Rayleigh range $2z_R$ depends on the laser wavelength λ and beam radius ω_0. For tight focusing in the interrogation region, ω_0 is the smallest radius of the laser beam (the spot size), hopefully centered on the detection optics. From these equations, we find the unsurprising result that a large laser-beam radius maximizes the volume and the system favors utilizing the full Rayleigh range as long as $2z_R \leq L_o$.

The number density of atoms ρ in the vapor cell can be calculated from published vapor pressure curves [1, 25].[1] Number density ρ [m^{-3}] is shown in Figure 3.6 with respect to temperature T. The number density ρ of all group II type atoms scales exponentially with temperature and can be expressed generally as

---

[1] The number density of Ra in this temperature range is not known; we extrapolate the curve for Ra from known high temperature values for vapor pressure and assumed similarity to other group II type atoms.

$$\rho(T[K]) \propto e^{\frac{-10^4}{T}}. \tag{3.8}$$

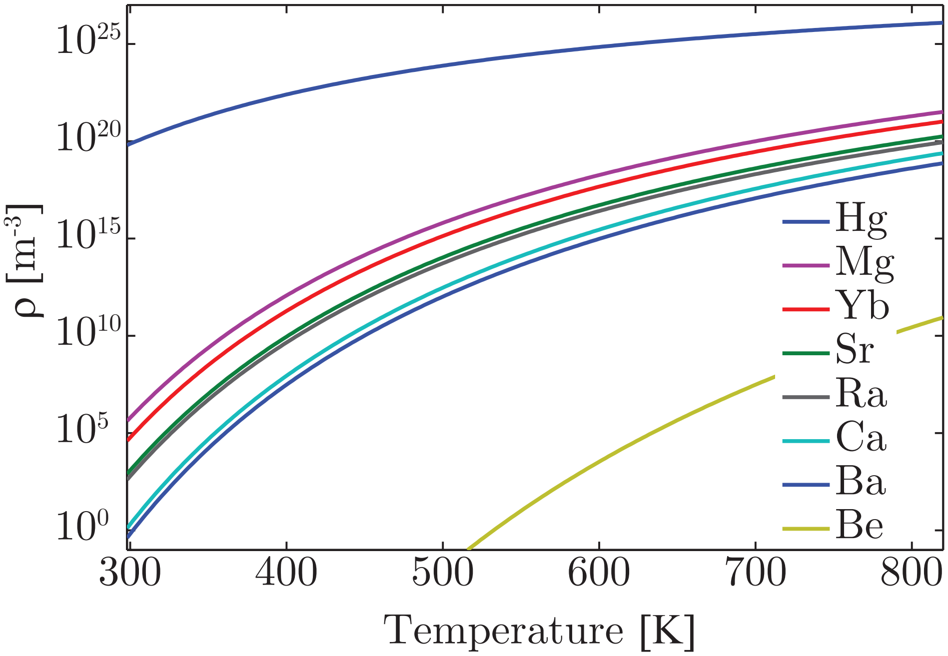

Figure 3.6: **Vapor Cell Density** Number density of group II type atoms with respect to vapor cell temperature. The high number density of Hg gives it a statistical advantage for optical stability.

The rate of atom interrogation $\dot{N}_{tot}$ is the product of the excitation volume V, the number density at room temperature ρ, and the rate at which atoms refresh in that volume. This refresh rate is the inverse of the average interrogation time $\bar{t}$. In curly brackets the different scaling behavior of detection- or Rayleigh-limited regimes is preserved. The interrogation rate is as follows:

$$\begin{aligned}\dot{N}_{tot} &= V \times \frac{\rho}{\bar{t}} \\ &= \begin{Bmatrix} V_{L_o} \\ V_{2z_R} \end{Bmatrix} \times \frac{\rho}{\bar{t}} \qquad (3.9) \\ \dot{N}_{tot}(T[K], \omega_0[m]) &\propto \begin{Bmatrix} \omega_0^2 \\ \omega_0^4 \end{Bmatrix} \times \frac{\sqrt{T}}{\omega_0} e^{\frac{-10^4}{T}} \qquad (3.10)\end{aligned}$$

3.4 Detection Channels

Detection of $^3P_0$ is difficult due to its metastability, it does not readily cascade to the ground state to produce a photon signaling excitation. Detection channels for this E1-M1 scheme in Hg are discussed in §7.6. In brief, collision induced relaxation or secondary excitation from the clock state to a level that relaxes more readily are both available options.

3.5 Probability of Clock Excitation

The two characteristic regimes of excitation probability $P_{^3P_0}$ in a hot E1-M1 optical clock are the time-limited and velocity-limited regimes, these follow from the discussion in §2.5. The time-limited probability of clock excitation (2.5) in a hot vapor cell can be written explicitly in terms of the vapor cell temperature and laser-beam radius as

$$P_{^3P_0}(T, \omega_0) \approx \Omega_{R2\gamma}(\omega_0)^2 \bar{t}(T, \omega_0)^2 \propto \frac{1}{T\omega_0^2}. \qquad (3.11)$$

This approximation provides less than 1% disagreement with the $P_{^3P_0}$ scaling behavior for sub-millimeter laser-beam radii in simulation. This is the appropriate length scale to verify because it contains the optimal radius for maximum detection rate $\dot{N}_D$.

The Doppler-limited probability of excitation (2.6) can also be written explicitly in terms of the vapor cell temperature and laser-beam radius:

$$P_{^3P_0}(T,\omega_0) \approx \frac{\Omega_{R2\gamma}(\omega_0)^2}{\Delta\nu_{D1}(T)^2} \propto \frac{1}{T\omega_0^4}. \tag{3.12}$$

In both regimes a high excitation probability $P_{^3P_0}$ favors small laser-beam radius ω_0 and low temperature T. Small laser-beam radius is an intuitive advantage here because atoms aren't interrogated long enough to undergo coherent Rabi flopping so smaller laser-beam radius will enhance the two-photon Rabi frequency $\Omega_{R2\gamma}$ (2.3). Lower temperatures lead to reduced atomic speeds $\bar{v}$ and longer interrogation times $\bar{t}$, which increase the probability $P_{^3P_0}$ of exciting a single atom.

3.6 Clock Excitation Rate

The experimental parameters that maximize the excitation rate $\dot{N}_{^3P_0}$ are different than those for optimum stability $\mathcal{S}$. While minimal $\mathcal{S}$ is the ultimate goal of this technology, it will be worthwhile to maximize $\dot{N}_{^3P_0}$ to experimentally quantify and optimize broadening parameters $\Delta\nu$ and transition probability $P_{^3P_0}$.

The effective clock excitation rate $\dot{N}_{^3P_0}$ (2.2) with a time-limited probability of excitation $P_{^3P_0}$ (3.11) and interrogation rate $\dot{N}_{tot}$ defined by (3.10) can now be reported in terms of temperature T and laser-beam radius ω_0:

$$\begin{aligned} \dot{N}_{^3P_0} &= P_{^3P_0} \times \dot{N}_{tot} && (3.13)\\ \dot{N}_{^3P_0}(T[K],\omega_0[m]) &\propto \frac{1}{T\omega_0^2} \times \begin{Bmatrix}\omega_0\\ \omega_0^3\end{Bmatrix}\sqrt{T}e^{\frac{-10^4}{T}} && (3.14)\\ &\propto \frac{e^{\frac{-10^4}{T}}}{\sqrt{T}}\begin{Bmatrix}\frac{1}{\omega_0}\\ \omega_0\end{Bmatrix} && (3.15)\end{aligned}$$

The curly brackets continue to denote the detection- (L_o) and Rayleigh-limited ($2z_R$) regimes of the experiment $\left\{\begin{smallmatrix}L_o\\ 2z_R\end{smallmatrix}\right\}$ (3.4,3.7). The optimal beam radius is the length

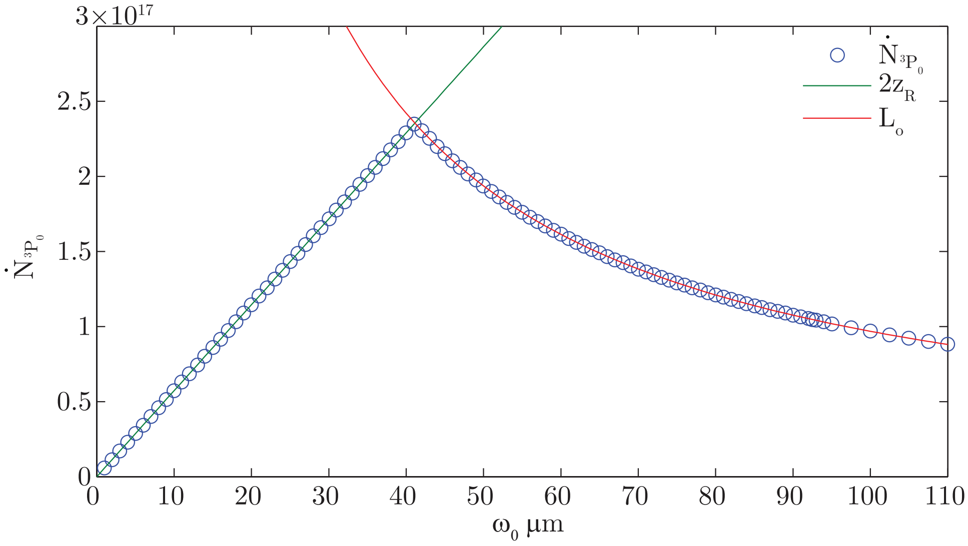

Figure 3.7: **Optimal laser-beam Size** Plot of effective excitation rate, $\dot{N}_{^3P_0}$, with respect to beam waist size (2.2) for neutral Hg at 448 K. Displays the asymptotic behavior in Rayleigh-limited and detection-limited regimes where the peak rates are found when the Rayleigh range $2z_R$ is set to match the detection length L_o, in Hg this happens at 41 μm.

where the Rayleigh range $2z_R$ matches the detection length L_o. Figure 3.7 show that for small ω_0, where $2z_r << L_o$, the overall rate increases with beam radius until $2z_R = L_o$, at which point the volume is detection-limited and detection rates begin to decrease with ω_0. The detection length L_o is the effective aperture of the detection system, any percent increase in L_o will lead to an equal percent in increase in interrogation volume and rate.

3.7 Experimental Detection of $^3P_0$ Atoms

The probability of detecting clock level occupation P_D depends on the chosen detection channel. Ideas for detection channels are explored in §7.6. We assume that all excited clock atoms will be detected by subsequent photon scattering. The photon collection efficiency of the imaging system (§7.5) impacts the probability of detection. In our calculation we set this collection efficiency P_{pc} at 1% as listed in Table 3.1.

Collisions are treated as a loss channel, so collision affects the P_D in calculation. Collision events occur with a rate proportional to the interrogation length $\bar{l} = 2\omega_0$ and the mean free path of the particles $(\rho\sigma)^{-1}$ where ρ is the number density of the atoms $[m^{-3}]$ and σ is the Van der Waals radius $[m^2]$. The number density ρ exponentially increases with temperature (3.8). The probability of no collision P_{nc} is given by

$$\begin{aligned} P_{nc}(T[K], \omega_0[m]) &= e^{-\rho(T)\sigma\bar{l}(\omega_0)} && (3.16) \\ &\propto e^{-\omega_0 e^{\frac{-10^4}{T}}} && (3.17) \end{aligned}$$

and primarily depends on the number density of atoms (see Figure 3.6). The risk of collision increases with interrogation length and cell temperature, which is unlike the rate behavior we've seen so far where increases in length and temperature increase rates. Hg is the only atom with a non-negligible probability of collision for the temperatures and interrogation lengths of this calculation, so optimal temperature and laser-beam radius represent the threshold between large excitation probability $P_{^3P_0}$ and large probability of no collision P_{nc}. This is due to Hg's considerably higher density compared with the other species, but the higher collision rate of Hg does not eliminate its viability as an optical clock. See §4.1.7 for details.

The final probability of detection P_D is

$$P_D = P_{pc} \times P_{nc}. \tag{3.18}$$

Using $\dot{N}_{^3P_0}$ and P_D, the calculated detection rates $\dot{N}_D$ for the group II type atoms, with optimal temperature T and laser-beam radius ω_0, are reported in Table 5.1 for the prototypical experimental settings listed in Table 3.1.

CHAPTER IV

E1-M1 Optical Clock Stability

Like the detection rate $\dot{N}_D$, the optimal clock stability $\mathcal{S}$ can be expressed in terms of experimentally controlled parameters. Stability scales with the inverse square root of the detection rate $\dot{N}_D$ (2.1) and linearly with the linewidth $\Delta\nu$

$$\mathcal{S} = \frac{\Delta\nu}{\nu_L}\sqrt{\frac{1}{\dot{N}_D}}. \tag{4.1}$$

The goal of an optical frequency standard is to minimize $\mathcal{S}$. The broadening mechanisms $\Delta\nu_i$ that in aggregate constitute the effective linewidth $\Delta\nu$ of this system will be discussed in detail in this chapter.

An optical frequency standard ultimately measures a resonant laser frequency ν_L. As described in Section 1.2, we assume that the natural transition frequency ν_0 is equivalent for like atoms. But the measured resonance will be inevitably offset from the natural transition frequency ν_0 by shifts due to environmental interaction

$$\nu_L = \nu_0 + \nu_B. \tag{4.2}$$

The total bias shift ν_B can be reduced or eliminated by reducing and offsetting individual experimental shifts $\Delta\nu_i$. The specific experimental settings that contribute to this shift ν_B are discussed in this chapter. The specific broadening and shift mechanisms we consider are listed in Table 4.1. The individual broadening and shift mechanisms for the optimal Hg clock are discussed explicitly. For the optimal monochromatic E1-M1 clock in Hg, the total broadening and shift budget is shown in Table 5.19.

Table 4.1: The mechanisms that contribute to broadening $\Delta\nu$ and the bias frequency shift ν_B in a hot E1-M1 clock are listed. The broadening due to the light shift $\Delta\nu_{LS}$ depends on the instability in laser intensity $\sigma_{\bar{I}}$. Broadening due to black-body radiation $\Delta\nu_{BB}$ will occur for temperature instability $\sigma_{\bar{T}}$.

Mechanism	$\Delta\nu$	ν_B
Natural	$\Delta\nu_{nat}$	0
Transit	$\Delta\nu_{TT}$	0
Laserline	$\Delta\nu_{LL}$	0
Doppler (1st-order)	$\Delta\nu_{D1}$	0
Doppler (2nd-order)	$\Delta\nu_{D2}$	ν_{D2}
Light Shift	$\Delta\nu_{LS}(\sigma_{\bar{I}})$	ν_{LS}
Blackbody Radiation	$\Delta\nu_{BB}(\sigma_{\bar{T}})$	ν_{BB}
Collision	$\Delta\nu_C$	ν_C

4.1 Broadening and Shift Mechanisms

4.1.1 Natural Width $\Delta\nu_{nat}$

The clock state has highly suppressed relaxation channels, leading to long lifetimes and intrinsically narrow linewidths $\Delta\nu_{nat}$. See §2.1 for a more thorough discussion of this forbidden relaxation property. Fermionic isotopes of the group II type atoms discussed here have a weakly allowed E1 transition between the clock state ${}^3P_0$ to the ground state ${}^1S_0$ due to hyperfine mixing with the ${}^3P_1$ intermediate level. This weakly allowed relaxation channel creates larger $\Delta\nu_{nat}$ in the Fermionic isotopes than in the Bosonic isotopes. A hot E1-M1 clock has fast atoms, and the short interrogation time of these atoms makes transit-time broadening $\Delta\nu_{TT}$ larger than the natural frequency width in both Fermionic and Bosonic isotopes.

Fermionic isotopes of Hg have estimated natural linewidths $\Delta\nu_{nat}$ of 0.5-0.7 Hz and the Bosonic isotopes have indefinite lifetimes [36].

4.1.2 Transit Broadening $\Delta\nu_{TT}$

The dominant broadening mechanism in an optimized hot E1-M1 scheme is transit-time broadening $\Delta\nu_{TT}$. In fact, any clock should set its Fourier limited resolution to match the next largest broadening mechanism. Transit broadening is defined by $\Delta\nu_{_{TT}} = 1/\bar{t}$ and is introduced by the brief interaction time of the fast atoms through the narrow laser-beam. As such, the optimal beam radius ω_0 to minimize $\Delta\nu_{TT}$ (and $\mathcal{S}$) is large. Transit broadening scales with the dynamic parameters ω_0 and T as:

$$\Delta\nu_{_{TT}}(T, \omega_0) \quad \propto \quad \frac{\sqrt{T}}{\omega_0} \tag{4.3}$$

For a hot Hg clock at minimal $\mathcal{S}$ we calculate a mean interrogation time of $5\,\mu s$, which introduces a Fourier uncertainty of $\Delta\nu_{TT} = 0.2$ MHz.

4.1.3 Light Shift and Broadening ν_{LS} and $\Delta\nu_{LS}$

The high levels of laser intensity required for non-vanishing transition probabilities $P_{^3P_0}$ (2.4) will introduce a.c. Stark shifts (light shifts) to the clock $^3P_0$ and ground $^1S_0$ states. This will create a systematic bias ν_{LS} in the fundamental frequency of the clock that scales with the intensity of the laser. Instability in laser intensity, $\sigma_{\bar{I}}$, will exhibit as a broadening to the system $\Delta\nu_{LS}$. Uncertainty in the absolute intensity will manifest as an unknown fundamental bias. The dynamic dipole polarizability difference $\Delta\alpha(\lambda)$ between the $^1S_0$ and $^3P_0$ levels of Hg at 531 nm is 21 a.u. [52][1] . The absolute shift scales with intensity as 2.25 kHz/$\frac{W}{mm^2}$.

---

[1] Thanks to Guangfu Wang who provided the exact value at 531 nm.

4.1.4 Doppler Effects

The motion of an atom with respect to a radiation source shifts that atom's resonance frequency from the natural frequency ν_0 into ν_{abs}

$$\nu_{abs} \simeq \nu_0 + \frac{\mathbf{k}}{2\pi} \cdot \mathbf{v} - \frac{1}{2}\nu_0 \left(\frac{v^2}{c^2}\right) + \frac{h\nu_0^2}{2Mc^2} \tag{4.4}$$

where $\mathbf{k}$ is the wavevector, $\mathbf{v}$ and v are the vector and scalar velocities of an atom, c is the speed of light, h is Planck's constant, and M is the atomic mass. The second term in (4.4) is the first-order Doppler shift $\nu_{D1} \approx \mathbf{k} \cdot \mathbf{v}$, the third term is the second-order Doppler shift $\nu_{D2} = -\frac{1}{2}\nu_0 \left(\frac{v^2}{c^2}\right)$, and the last term is the recoil shift which is negligibly small in our system. Doppler broadening depends on one of the dynamic parameters we elect to optimize: the vapor cell temperature T.

4.1.4.1 First-order Doppler Broadening $\Delta\nu_{D1}$

The primary measurement environment considered here is a hot vapor cell of atoms moving freely and isotropically with thermal velocity distributions (as opposed to ultracold trapped atoms). For the ensemble of atoms, the first-order Doppler broadening introduces no absolute bias shift ν_B to the optical transition because atomic velocities in the vapor cell are isotropically oriented. The distribution of velocities does introduce a distribution of effective detunings from resonance. An atom with velocity components in the direction of the wavevector k will experience an individual frequency shift ν_{D1} and the ensemble will have an aggregate distribution of resonant frequencies that depends on the velocity distribution of the atoms. This broadening is termed first-order Doppler broadening.

Single-photon optical frequency standards must operate with ultracold atoms because the first-order Doppler width is prohibitively large for room temperature atoms. Table 4.2 shows the single-photon E1-type first-order Doppler broadening in terms

Table 4.2: The $\Delta\nu_{D1}$ for E1-type atomic clock schemes. This table illustrates the prohibitively large fist-order Doppler broadening in group II type atoms that requires the use of ultracold atoms to construct a viable optical frequency standard.

atom	$\nu_{D1}(T)$ [MHz]	$\nu_{D1}(300K)$ [GHz]
Be	$160 \times \sqrt{T}$	2.8
Mg	$97 \times \sqrt{T}$	1.7
Hg	$58 \times \sqrt{T}$	1.0
Ca	$52 \times \sqrt{T}$	0.9
Sr	$33 \times \sqrt{T}$	0.6
Yb	$29 \times \sqrt{T}$	0.5
Ba	$23 \times \sqrt{T}$	0.4
Ra	$19 \times \sqrt{T}$	0.3

of temperature dependence for the group II type atoms. The GHz shifts at room temperature show it would be impractical to implement a single-photon E1 optical frequency standard in a vapor cell.

The first-order Doppler broadening that plagues single-photon transitions can be easily reduced in the two-photon transition of an E1-M1 optical standard. The first-order Doppler shift in a two-photon transition is the sum of the first-order Doppler shifts from each of the excitation lasers with wavevectors $\mathbf{k}_1$ and $\mathbf{k}_2$.

$$\nu_{D1} = \mathbf{k}_1 \cdot \mathbf{v} + \mathbf{k}_2 \cdot \mathbf{v}; \tag{4.5}$$

where experimentally setting $\mathbf{k}_1 = -\mathbf{k}_2$ to implement a Doppler-free excitation of an atom with any velocity orientation $\mathbf{v}$ is well known [7] and commonly performed. For the experimental implementation of a monochromatic ($|\mathbf{k}_1| = |\mathbf{k}_2|$), Doppler-free method, we must characterize error in alignment angle θ to obtain a bound on the residual first-order Doppler broadening. Alignment of counter-propagating lasers can be characterized by

$$\mathbf{k}_1 = -\mathbf{k}_2 \cos(\theta). \tag{4.6}$$

If we assume a misalignment of counter-propagating lasers by the angle limit listed in Table 3.1, we find that residual first-order Doppler broadening is larger than the natural linewidth of these atomic systems. The temperature T and alignment angle θ dependence of first-order Doppler broadening for each atomic species is listed in Table 3.4.

For the case of neutral Hg in a vapor cell with alignment angle $\theta = 0.0001$ radians, the residual first-order Doppler broadening is shown for $T = 380K$ and $T = 800K$ in Figure 4.1. This figure illustrates that setting $\Delta\nu_{D1}$ equal to the mean velocity $\bar{v}$ is appropriate because $\bar{v} \approx 1.1 v_P$.

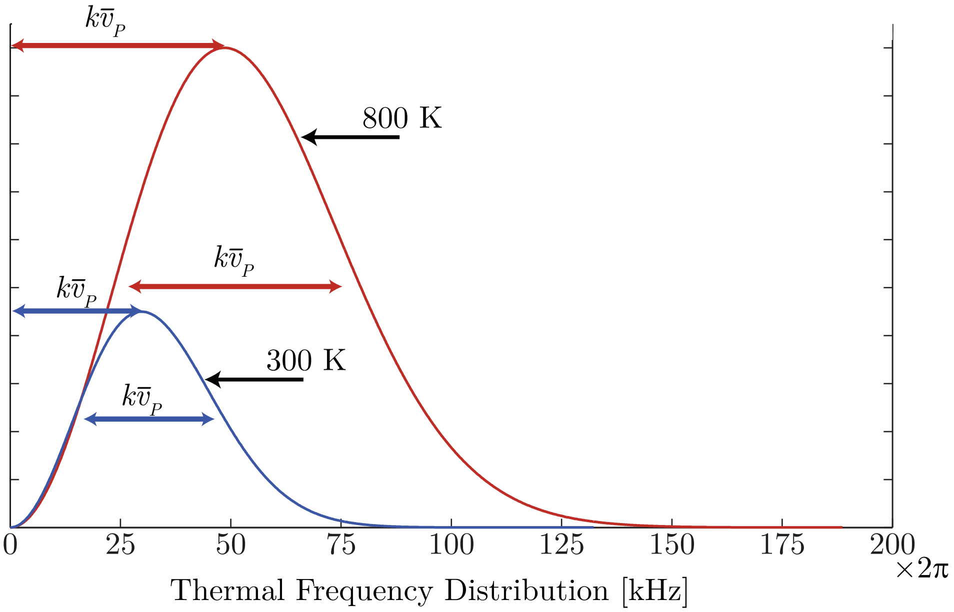

Figure 4.1: **Thermal Shift from Doppler Effects** Diagram of neutral Hg with the most probable frequency $\bar{v}_P/\lambda$ for each temperature class shown. This illustrates that mean velocity $\bar{v} = 2\bar{v}_P$ is a good, conservative estimation of the velocity broadening.

The magnitudes of residual first-order Doppler broadening $\Delta\nu_{D1}$ found in hot group II type atoms is an $\mathcal{S}$ limiting feature. This behavior is illustrated at the end of this chapter in Figure 4.2.

The bichromatic E1-M1 scheme that can be implemented to eliminate the light shift (see Chapter VI) requires that $|\mathbf{k}_1| \neq |\mathbf{k}_2|$. While the misalignment angle θ

(4.6) can be intentionally introduced to make $|\mathbf{k}_1| = |\mathbf{k}_2 \cos(\theta)|$, this will only eliminate first-order Doppler effects for a single velocity direction. In a vapor cell the atom velocities are isotropic and so the optimal alignment angle to reduce Doppler broadening is found at $\theta = 0$.

In a thermal atomic beam, the velocity distribution has a significant orientation along the atom beam path. A bichromatic excitation scheme may have smaller residual first-order Doppler broadening in an thermal beam than a vapor cell because laser alignment can be oriented to that thermal beam direction.

4.1.4.2 Second-order Doppler Broadening $\Delta\nu_{D2}$

The temperature dependence of the second-order Doppler shift is given by

$$\nu_{D2}(T) = -\nu \frac{\bar{v}(T)^2}{2c^2} \tag{4.7}$$

and the shift is linear in temperature.

Second-order Doppler shift ν_{D2} and broadening $\Delta\nu_{D2}$ cannot be compensated for with laser alignment like first-order broadening because these quantities scale with atomic velocity squared (4.4). The negative sign in the second-order Doppler shift ν_{D2} imparts a red-detuning shift to the overall bias frequency of the system ν_B. If we assume temperature stability of 0.1 K (see Table 3.1) we can place a firm estimate on the mean shift ν_{D2} at the optimal clock operating temperature. Instability of drift in temperature will lead to broadening but will likely occur on long timescales and therefore be easy to account for in analysis. Table 4.3 shows the second-order Doppler shift ν_{D2} of each of the group II type atoms in an E1-M1 schme with respect to temperature T in Kelvin.

The second-order Doppler effect also introduces broadening $\Delta\nu_{D2}$ to the resonance

Table 4.3: The E1-M1 second-order Doppler broadening $\Delta\nu_{D2}$ for the group II type atoms.

atom	$\nu_{D2}(T)$ [Hz]
Ra	$-0.04 \times T$
Ba	$-0.06 \times T$
Yb	$-0.07 \times T$
Sr	$-0.11 \times T$
Hg	$-0.13 \times T$
Ca	$-0.26 \times T$
Mg	$-0.62 \times T$
Be	$-1.7 \times T$

frequency of the transition. The velocity distribution of the thermal atoms leads to a distribution of second-order Doppler shifts which manifests as a broadening. The characteristic width of the velocity distribution is similar to the mean velocity, so we assume $\Delta\nu_{D2} \approx |\nu_{D2}|$.

First-order and second-order Doppler broadening both increase the linewidth of the frequency standard. The temperature dependence of first-order Doppler broadening is described by (3.2). Figure 4.1 illustrates the effective frequency shift from the first-order Doppler broadening in Hg. For the optimal Hg E1-M1 clock operating 380 K with misalignment angle θ less that 0.1 milliradians, the first-order Doppler broadening $\Delta\nu_{D1}$ will contribute a maximum of 44 kHz of line broadening and second-order Doppler broadening $\Delta\nu_{D2}$ will be 90 Hz

4.1.5 Laser-Line Broadening $\Delta\nu_{LL}$

The linewidth of the excitation laser contributes to the broadening of the system. This is because the laser linewidth is the bottleneck through which all narrow linewidth information passes to the oscillation counter in an optical frequency standard. If an optical transition has a kHz linewidth, but the resonant laser has a GHz linewidth, then even if the laser is resonant with and centered on the transition, the detector will not register resonance features narrower than a GHz. With transit broadening of nearly a MHz for all hot clock atoms in the E1-M1 scheme, excitation lasers with sub-kHz linewidths will make a negligible contribution to the overall broadening. Strictly speaking, the laser linewidth has a Lorentzian profile which does not contribute to broadening quadractically. However, since we assume that the laser linewidth is much smaller than the effective broadening of the system, we add it quadratically for $\mathcal{S}$ calculation purposes.

4.1.6 Black-body Radiation Shift and Broadening ν_{BB} and $\Delta\nu_{BB}$

The estimated black-body radiation shifts and uncertainties have been cataloged elsewhere [37]. In Hg at 380 K the shift is −1.63 Hz. Inaccuracy and instability $\sigma_{\bar{T}}$ in operating temperature can introduce an unknown systematic shift and broadening. This is typically much smaller than other broadening and shift features due to the overall small size of the black-body radiation shift.

4.1.7 Collision Shift and Broadening ν_C and $\Delta\nu_C$

In this calculation we treat collision as a loss channel so we exclude collision broadening for the effective linewidth calculation. Collisions do introduce harm the stability $\mathcal{S}$ in our calculation through reduced signal. This is an inaccurate approximation because it is not how collision dynamics contribute to signal, but this signal loss approximation imparts more damage to the $\mathcal{S}$ than actual collision broadening likely will. All the group II atoms, with the exception of Hg, have less than 0.1% probability of experiencing a collision in the excitation region. At the optimal operating temperature for the hot Hg clock, the collision frequency is 33 MHz. Approximately 60% of Hg atoms in the excitation region N will experience a collision which can, in the worst-case scenario, harm the stability of the clock by a factor of 1.3. The specific collision phase shift introduced by colliding ${}^1S_0$ and ${}^3P_0$ Hg atoms is unknown. The worst-case estimate assumes a collided atom $N_C = 0.6 \times N$ results in an even probability of a phase shift into (or out of) the clock level. We assume collided atoms are not more likely than uncollided atoms to excite to the clock level. In that limit, half of the collided atoms $0.5 \times N_C$ will present in the clock level and contribute noise as the square root of that number. The signal-to-noise of a clock system with $0.4 \times N$ clock-level atoms, absent collision noise, should scale as $\sqrt{0.4 \times N}$. Then our worst-case collision scenario suffers from a signal-to-noise reduction of

$$\frac{0.4 \times N}{\sqrt{0.4 \times N + 0.5 \times 0.6 \times N}} = \frac{\sqrt{0.4 \times N}}{1.3} \tag{4.8}$$

which is 1.3 times more harmful to $\mathcal{S}$ than a system without collision noise. The actual collision phase shifts are likely much less harmful to $\mathcal{S}$. The true collision dynamics must be measured experimentally to quantify broadening $\Delta\nu_C$ and any absolute collision shift ν_C.

4.2 Shift Mechanisms for Metrology Gravitational Redshift ν_G

The previous section (4.1) outlined shift mechanisms which must be measured precisely and compensated for during clock operation to achieve small $\mathcal{S}$ and accurate characterization of bias shift ν_B. However, one of the opportunities of an optical frequency standard with minimal $\mathcal{S}$ is sensitivity to environmental shifts that are otherwise challenging to measure. The gravitational redshift is one such opportunity and the sensitivity of a monochromatic E1-M1 clock to this shift is discussed.

When an oscillator changes elevation by Δh then that oscillator experiences a shift in frequency ν_G as

$$\frac{\nu_G}{\nu_0} = \frac{g\Delta h}{c^2} \tag{4.9}$$

where ν_0 is the natural frequency of the oscillator and g is local acceleration due to gravity [11]. To clarify the sign convention, when an oscillator is at a lower elevation it experiences a redshift. The elevation sensitivity of an optical frequency standard with stability $\mathcal{S}$ operated for a total measurement time τ is given by

$$\Delta h(\tau) \;=\; \frac{c^2\mathcal{S}}{g\tau} \tag{4.10}$$

An OFS becomes a meterstick on earth (i.e. is sensitive to Δh = one meter) with only 1 second of experiment time τ when the stability $\mathcal{S} = 1.1 \times 10^{-16}$. Table 5.20 displays the time each group II type atom's hot E1-M1 clock will attain meterstick precision.

4.3 Optimal Clock Stability

Optimal stability $\mathcal{S}$ for each group II type atom can be achieved by balancing the effects of laser-beam radius ω_0 with vapor cell temperature T. Figure 4.2 illustrates the asymptotic behavior of effective broadening $\Delta\nu$ of the hot monochromatic E1-M1 clock scheme in neutral Ra at $T = 800K$. The dependence of $\Delta\nu$ on $\Delta\nu_{TT}$ and $\Delta\nu_{D1}$ and its overall scaling with respect to laser-beam radius ω_0 in Ra is characteristic for all the group II type atoms, with the exception of Hg which has heightened sensitivity to collisions.

As you can see in Figure 4.2, the ideal laser-beam radius ω_0 for minimum $\mathcal{S}$ is closely related to the crossover point between time-limited $\Delta\nu_{TT}$ (4.3) and velocity-limited $\Delta\nu_{D1}$ (3.2) broadening regimes. The slight difference is due to the competing advantage of increased excitation rate $\dot{N}_{^3P_0}$ at smaller ω_0 in this detection-limited regime. Since optimal $\mathcal{S}$ occurs in a detection-limited volume, we use the L_o scaling of the effective clock excitation rate $\dot{N}_{^3P_0}$ (3.15). We compare the scaling behavior of the time- and velocity-limited regimes with respect to laser-beam radius ω_0 and temperature T to determine the minimum $\mathcal{S}$ (4.1):

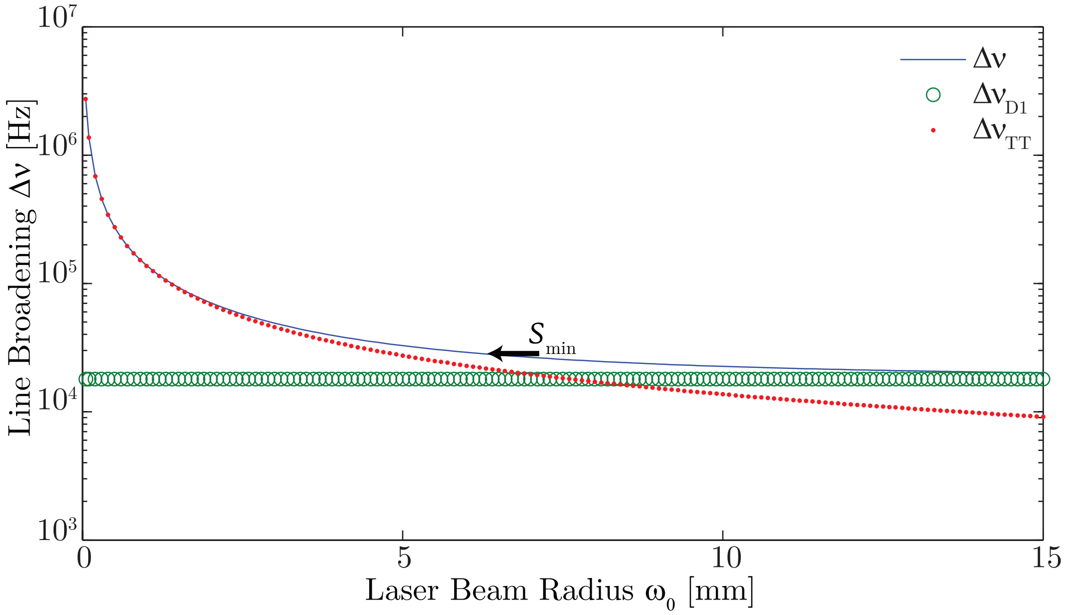

Figure 4.2: **Asymptotic Behavior of $\boldsymbol{\Delta\nu}$ in Ra** Calculation results for laser-beam radius ω_0 dependence of the transit broadening $\Delta\nu_{TT}$, first-order Doppler broadening $\Delta\nu_{D1}$, and total broadening $\Delta\nu$ for Ra at vapor cell temperature 800 K .

$$\mathcal{S} \propto \begin{Bmatrix} \Delta\nu_{TT} \\ \Delta\nu_{D1} \end{Bmatrix} \times \sqrt{\frac{1}{\dot{N}_{^3P_0}}} \tag{4.11}$$

$$\begin{aligned} \mathcal{S}(T[K], \omega_0[m]) &\propto \begin{Bmatrix} \sqrt{T}/\omega_0 \\ \sqrt{T} \end{Bmatrix} \times \sqrt{\frac{\omega_0\sqrt{T}}{e^{\frac{-10^4}{T}}}} \\ &\propto \sqrt{\frac{T\sqrt{T}}{e^{\frac{-10^4}{T}}} \begin{Bmatrix} \frac{1}{\omega_0} \\ \omega_0 \end{Bmatrix}}. \end{aligned} \tag{4.12}$$

Curly brackets no longer denote the geometry limits of (3.10), instead they are the time- and velocity-limited behavior $\left\{\begin{smallmatrix}\Delta\nu_{TT}\\ \Delta\nu_{D1}\end{smallmatrix}\right\}$. As when we maximize excitation rate $\dot{N}_{^3P_0}$ (3.15), optimally small $\mathcal{S}$ favors high temperature T. Unlike maximum $\dot{N}_{^3P_0}$, optimal $\mathcal{S}$ favors a larger laser-beam radius ω_0 than the one that matches the Rayleigh range to the detection-limit. This is due to $\mathcal{S}$'s sensitivity to transit-time broadening $\Delta\nu_{TT}$ (4.3). The beam size ω_0 for all candidate atoms (except Hg) is best increased until transit broadening is comparable with the residual first-order Doppler broadening. The specific beam size recommendations listed in Table 5.2 therefore reflect the transition from a $\Delta\nu_{TT}$ to $\Delta\nu_{D1}$ dominated regime for the non-Hg atoms.

Hg is affected by collision broadening and thus is optimized at a lower temperature T and smaller beam radius ω_0 than predicted by the collision-free model (4.12). The plot of $\Delta\nu$ for Hg is shown in Figure 4.3 where it can be seen that $\mathcal{S}_{min}$ occurs at a much smaller radius ω_0 than the crossover point.

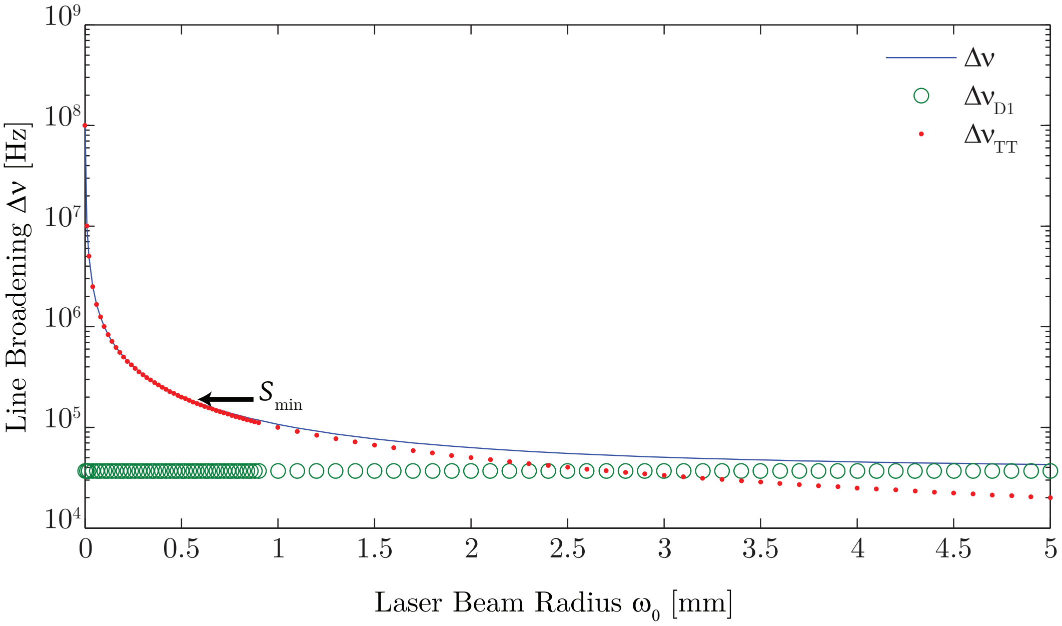

Figure 4.3: **Asymptotic Behavior of $\Delta\nu$ in Hg** Calculation results for laser-beam radius ω_0 dependence of the transit broadening $\Delta\nu_{TT}$, first-order Doppler broadening $\Delta\nu_{D1}$, and total broadening $\Delta\nu$ for Hg at vapor cell temperature 380 K .

Systematic shifts ν_B are inevitable, but for a well known system they can be monitored and offset in analysis. These absolute frequency shifts contribute linearly to the bias frequency, so the final ν_B is a sum of the systematic shifts of the E1-M1 experiment listed in Table 4.1.

The broadening components contribute in a more nuanced fashion. For $\mathcal{S}$ calculations, we aggregate the broadening in quadrature in keeping with the predominantly Gaussian nature of the broadening mechanisms.

We show in Chapter V that hot clock stabilities for group II type atoms are competitive with current cold standards. These stabilities $\mathcal{S}$ can be achieved with a single excitation laser driving a degenerate two-photon E1-M1 transition and in the case of Hg using commercially available laser and optics systems.

CHAPTER V

Monochromatic E1-M1 Optical Clock Detection Rates and Stability

5.1 Calculation Results

The calculated detection rates $\dot{N}_D$ and clock stabilities $\mathcal{S}$ for the hot monochromatic E1-M1 scheme are presented for the group II type atoms Hg, Sr, Yb, Ca, Mg, Be, Ra, and Ba. The optimal temperature T and laser-beam radius ω_0 for both detection rate $\dot{N}_D$ (2.1) and stability $\mathcal{S}$ (4.1) are presented.

While $\mathcal{S}$ is the most important parameter to consider for the ultimate performance of an optical frequency standard, the immediate work in developing an E1-M1 standard will require experimental quantification of all the assumptions made in this model (to name a few: collision broadening $\Delta\nu_C$, transition probability $P_{^3P_0}$, and light shift ν_{LS}). To precisely characterize these quantities it will be useful to operate at maximum detection rate $\dot{N}_D$.

Calculations from the models developed in this dissertation produce $\dot{N}_D$ and $\mathcal{S}$ magnitudes over the dynamic parameter space of laser-beam radius ω_0 and vapor cell temperature T. These are presented in contour plots which reveal the $\dot{N}_D$ maximum and $\mathcal{S}$ minimum for each species. These optimal spaces are denoted by the darkest color on the plot. For both $\dot{N}_{Dmax}$ and $\mathcal{S}_{min}$, neutral Hg performs the best

Table 5.1: The detection rate of clock atoms, $\dot{N}_D$, at the optimal vapor cell temperature T and laser-beam radius ω_0 for each group II type atom. The optimal ω_0 in all cases is the radius where the Rayleigh range matches the detection length, L_o, of the detection optics which maximizes $\dot{N}_D$. These are not the values for optimal clock stability.

Atom	T [K]	$\omega_0 [\mu m]$	$\dot{N}_D$ [s^{-1}]
Hg	448	41.0	$1.8 \times 10^{+12}$
Yb	800	60.0	$6.4 \times 10^{+10}$
Ra	800	70.0	$4.3 \times 10^{+10}$
Sr	800	67.5	$8.4 \times 10^{+8}$
Ba	800	72.5	$4.6 \times 10^{+8}$
Mg	800	55.0	$6.3 \times 10^{+6}$
Ca	800	65.0	$3.8 \times 10^{+6}$
Be	800	55.0	1.0×10^{-7}

of the group II type atoms.

For comparison between group II type atoms, the optimal experimental settings and maximum excitation rate $\dot{N}_D$ are listed for all atoms in Table 5.1. Likewise the optimal stability (small) $\mathcal{S}$ settings and results are listed in Table 5.2. All calculations use the experimental assumptions in Table 3.1. The optimal temperature for Hg stands out in each table because it is uniquely optimized at a lower temperature than the damage threshold of the optics. This difference from the other elements is due to its higher number density ρ and subsequently higher collision rate.

When comparing atoms, insensitivity to transit broadening $\Delta\nu_{TT}$ is important because it reduces $\mathcal{S}$ in a hot E1-M1 clock. Relative insensitivity to transit broadening scales with atomic mass. Table 3.4 shows relative first-order Doppler broadening between the group II type atoms. It is noteworthy to point out that as a hot E1-M1 optical clock Be is a worse frequency standard than a quartz oscillator.

Table 5.2: The vapor cell temperature T and laser-beam radius ω_0 to achieve minimum $\mathcal{S}$ for each group II type atom is listed. Stability $\mathcal{S}$ is defined in (1.2) and characterizes how quickly a frequency standard can achieve a chosen absolute instability σ_ν. Please see Table 3.2 for a list of the monochromatic excitation wavelengths $\lambda_{2\gamma}$.

Atom	T [K]	ω_0[mm]	$\mathcal{S}$ [$\sqrt{\text{Hz}^{-1}}$]
Hg	382	0.5	3.1×10^{-15}
Ra	800	6.3	7.1×10^{-15}
Yb	800	2.9	8.4×10^{-15}
Sr	800	5.1	8.4×10^{-14}
Ba	800	7.1	8.5×10^{-14}
Ca	800	5.7	1.7×10^{-12}
Mg	800	1.9	2.4×10^{-12}
Be	800	4.0	1.9×10^{-5}

5.2 Detection rate $\dot{N}_D$ results for group II type atoms

In this section you will find contour plots of each group II type atom's detection rate $\dot{N}_D$ magnitude with respect to temperature T and laser-beam radius ω_0. In calculation, laser-beam radius ω_0 was varied from 10 μm up to a few mm and vapor cell temperature T was evaluated from room temperature (300 K) up to the optical damage threshold of 800 K. The subset of laser-beam radii and temperatures immediately surrounding the local maximum of detection rate $\dot{N}_D$ are displayed. The Hg temperature and radius result is remarkably distinct from the other group II type atoms due to collision effects.

For insight into these contour plots, the vertical slice behavior is dominated by the detection- and Rayleigh- limited regimes of $\dot{N}_{^3P_0}$ for all group II type atoms shown with respect to laser-beam radius ω_0 in Figure 3.7.

Horizontal-slice scaling follows the number density ρ of atoms most strongly, shown with respect to temperature in Figure 3.6.

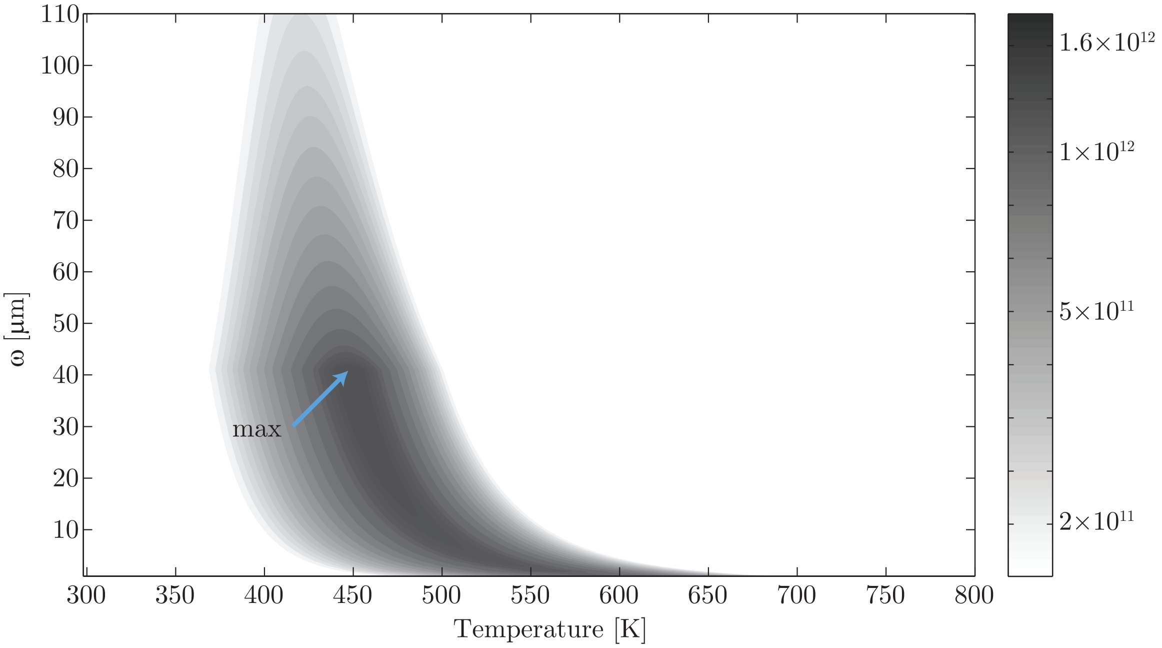

Figure 5.1: $\boldsymbol{\dot{N}_D}$ **Magnitudes for Hg** The hot Hg detection rate $\dot{N}_D$ (2.1) of the E1-M1 transition is plotted for laser-beam radius ω_0 and vapor cell temperature T. The maximum $\dot{N}_{D\max} = 1.8 \times 10^{12}\,\mathrm{s}^{-1}$ is found at $\omega_0 = 41\,\mu\mathrm{m}$ and $T = 448$ K.

Table 5.3: Hg parameters at the $\dot{N}_{D\max}$.

Parameter		Value
$\dot{N}_{D\max}$	detection rate (2.1)	$1.8{\times}10^{+12}$ s^{-1}
ω_0	laser-beam radius	41 μm
T	vapor cell temperature	448 K
$P_{^3P_0}$	excitation probability (2.4)	$1.1{\times}10^{-5}$
$\dot{N}_{\mathrm{tot}}$	atom interrogation rate (3.10)	$4.4{\times}10^{+19}$ s^{-1}
$\Omega_{R2\gamma}$	two-photon Rabi frequency (2.3)	$1.8{\times}10^{+4}$ Hz
$\bar{t}$	interrogation time (3.1)	0.38 μs

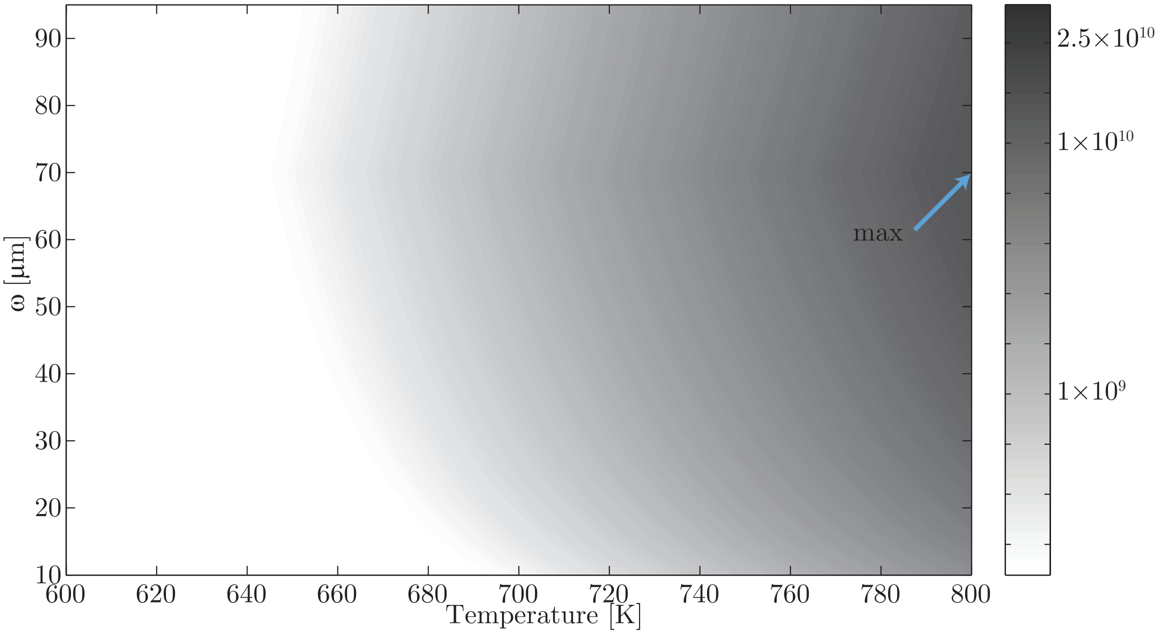

Figure 5.2: **$\dot{N}_D$ Magnitudes for Ra** The hot Ra detection rate $\dot{N}_D$ (2.1) of the E1-M1 transition is plotted for laser-beam radius ω_0 and vapor cell temperature T. The maximum $\dot{N}_{D\max} = 4.3 \times 10^{10}\,\mathrm{s}^{-1}$ is found at $\omega_0 = 70\,\mu$m and $T = 800$ K.

Table 5.4: Ra parameters at the $\dot{N}_{D\max}$.

Parameter		Value
$\dot{N}_{D\max}$	detection rate (2.1)	$4.3\times10^{+10}$ s^{-1}
ω_0	laser-beam radius	70 μm
T	vapor cell temperature	800 K
$P_{^3P_0}$	excitation probability (2.4)	1.4×10^{-4}
$\dot{N}_{\mathrm{tot}}$	atom interrogation rate (3.10)	$3.1\times10^{+16}$s^{-1}
$\Omega_{R2\gamma}$	two-photon Rabi frequency (2.3)	$4.6\times10^{+4}$ Hz
$\bar{t}$	interrogation time (3.1)	0.51 μs

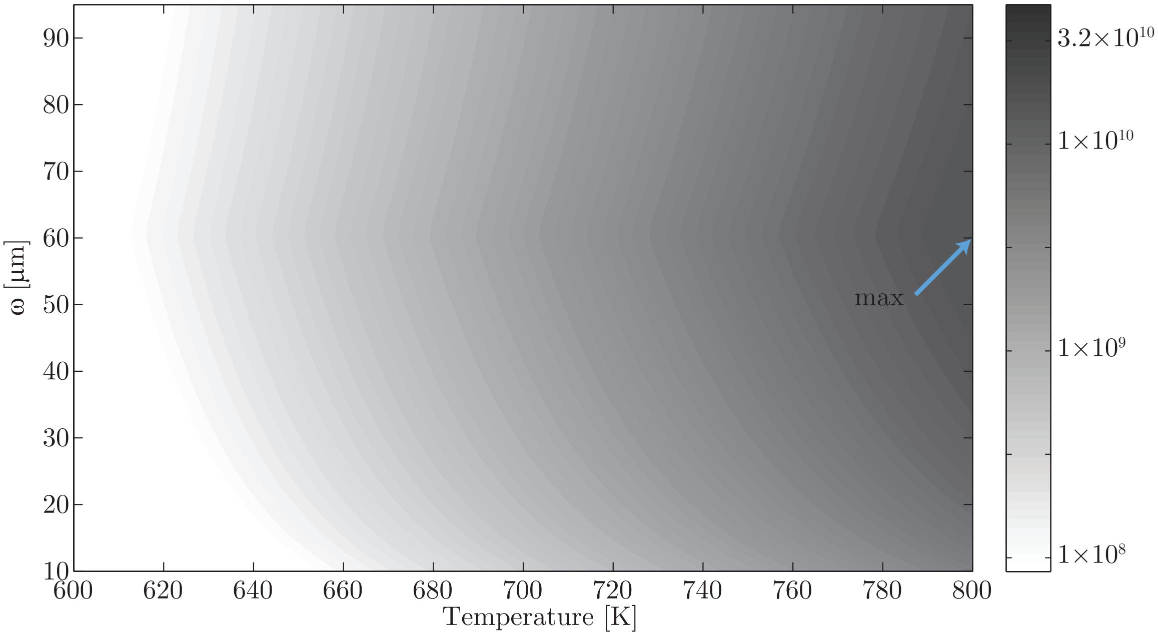

Figure 5.3: **$\dot{N}_D$ Magnitudes for Yb** The hot Yb detection rate $\dot{N}_D$ (2.1) of the E1-M1 transition is plotted for laser-beam radius ω_0 and vapor cell temperature T. The maximum $\dot{N}_{D\max} = 6.4 \times 10^{10}\,\mathrm{s}^{-1}$ is found at $\omega_0 = 60\,\mu$m and $T = 800$ K.

Table 5.5: Yb parameters at the $\dot{N}_{D\max}$.

Parameter		Value
$\dot{N}_{D\max}$	detection rate (2.1)	$6.4\times10^{+10}$ s^{-1}
ω_0	laser-beam radius	60 μm
T	vapor cell temperature	800 K
$P_{^3P_0}$	excitation probability (2.4)	1.8×10^{-5}
$\dot{N}_{\mathrm{tot}}$	atom interrogation rate (3.10)	$3.5\times10^{+17}$ s^{-1}
$\Omega_{R2\gamma}$	two-photon Rabi frequency (2.3)	$2.2\times10^{+4}$ Hz
$\bar{t}$	interrogation time (3.1)	0.38 μs

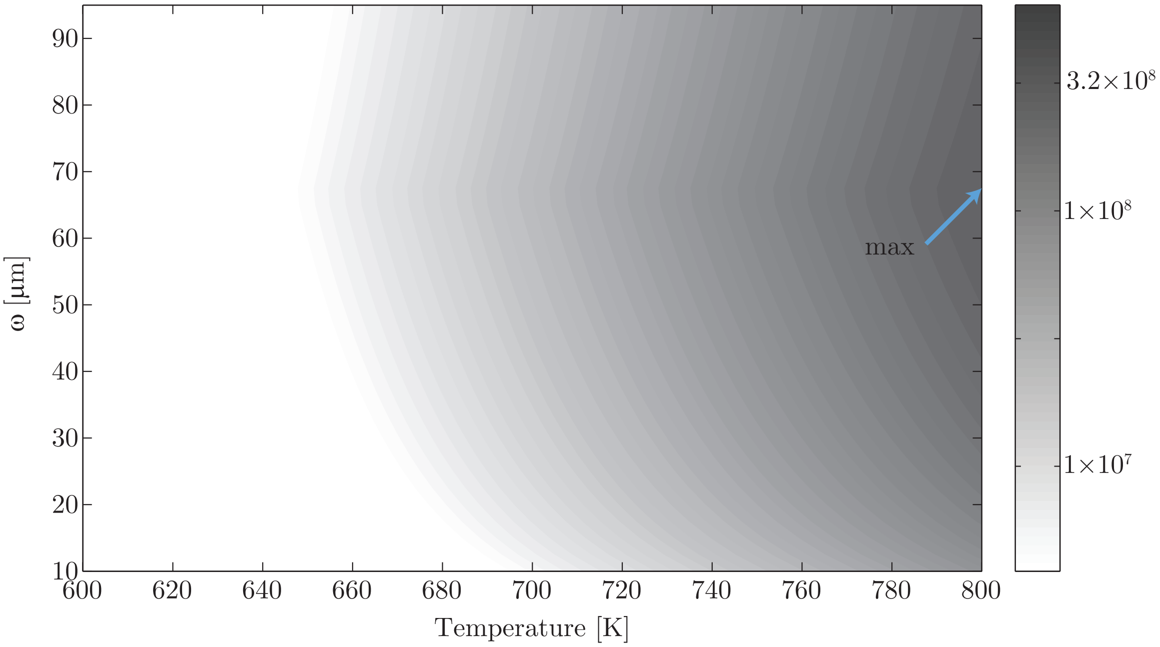

Figure 5.4: **$\dot{N}_D$ Magnitudes for Sr** The hot Sr detection rate $\dot{N}_D$ (2.1) of the E1-M1 transition is plotted for laser-beam radius ω_0 and vapor cell temperature T. The maximum $\dot{N}_{D\max} = 8.4 \times 10^8\,\mathrm{s}^{-1}$ is found at $\omega_0 = 67.5\,\mu$m and $T = 800$ K.

Table 5.6: Sr parameters at the $\dot{N}_{D\max}$.

Parameter		Value
$\dot{N}_{D\max}$	detection rate (2.1)	$8.4{\times}10^{+8}$ s^{-1}
ω_0	laser-beam radius	67.5 μm
T	vapor cell temperature	800 K
$P_{^3P_0}$	excitation probability (2.4)	$8.8{\times}10^{-7}$
$\dot{N}_{\mathrm{tot}}$	atom interrogation rate (3.10)	$9.6{\times}10^{+16}$ s^{-1}
$\Omega_{R2\gamma}$	two-photon Rabi frequency (2.3)	$6.1{\times}10^{+3}$ Hz
$\bar{t}$	interrogation time (3.1)	0.31 μs

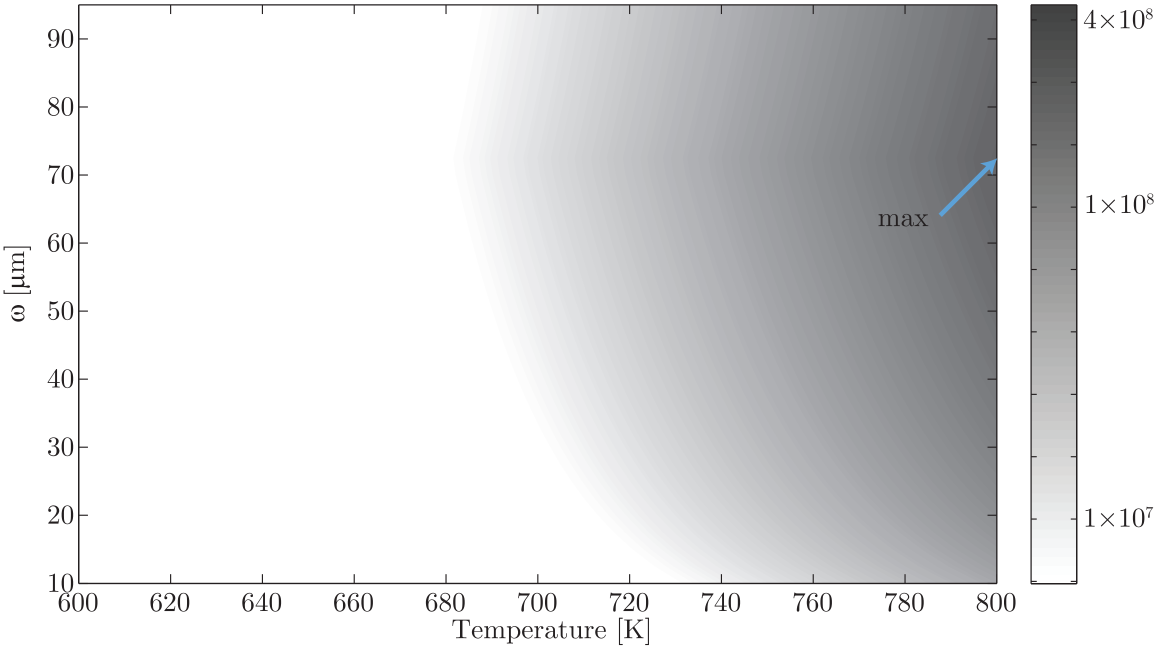

Figure 5.5: **$\dot{N}_D$ Magnitudes for Ba** The hot Ba detection rate $\dot{N}_D$ (2.1) of the E1-M1 transition is plotted for laser-beam radius ω_0 and vapor cell temperature T. The maximum $\dot{N}_{D\text{max}} = 4.6 \times 10^8\,\text{s}^{-1}$ is found at $\omega_0 = 72.5\,\mu$m and $T = 800$ K.

Table 5.7: Ba parameters at the $\dot{N}_{D\text{max}}$.

Parameter		Value
$\dot{N}_{D\text{max}}$	detection rate (2.1)	$4.6\times10^{+8}$ s^{-1}
ω_0	laser-beam radius	72.5 μm
T	vapor cell temperature	800 K
$P_{^3P_0}$	excitation probability (2.4)	1.4×10^{-5}
$\dot{N}_{\text{tot}}$	atom interrogation rate (3.10)	$3.3\times10^{+15}$s^{-1}
$\Omega_{R2\gamma}$	two-photon Rabi frequency (2.3)	$1.8\times10^{+4}$ Hz
$\bar{t}$	interrogation time (3.1)	0.41 μs

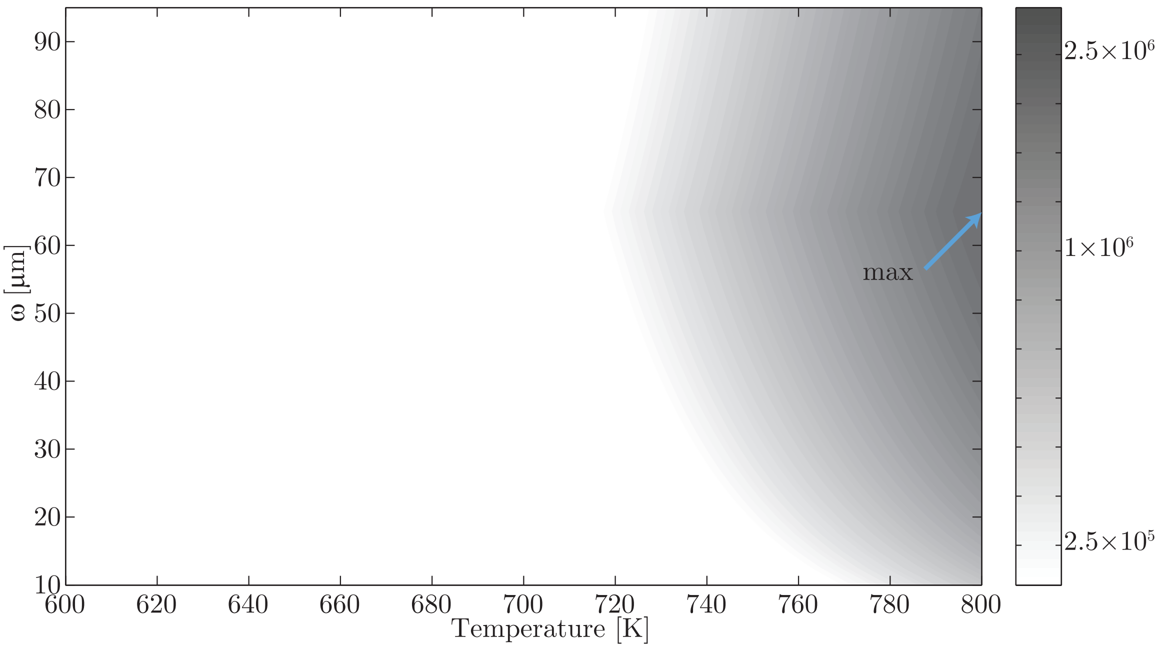

Figure 5.6: **$\dot{N}_D$ Magnitudes for Ca** The hot Ca detection rate $\dot{N}_D$ (2.1) of the E1-M1 transition is plotted for laser-beam radius ω_0 and vapor cell temperature T. The maximum $\dot{N}_{D\max} = 3.8 \times 10^6\,\mathrm{s}^{-1}$ is found at $\omega_0 = 65\,\mu$m and $T = 800$ K.

Table 5.8: Ca parameters at the $\dot{N}_{D\max}$.

Parameter		Value
$\dot{N}_{D\max}$	detection rate (2.1)	$3.8{\times}10^{+6}$ s^{-1}
ω_0	laser-beam radius	65 μm
T	vapor cell temperature	800 K
$P_{^3P_0}$	excitation probability (2.4)	$2.2{\times}10^{-8}$
$\dot{N}_{\mathrm{tot}}$	atom interrogation rate (3.10)	$1.8{\times}10^{+16}$ s^{-1}
$\Omega_{R2\gamma}$	two-photon Rabi frequency (2.3)	$1.5{\times}10^{+3}$ Hz
$\bar{t}$	interrogation time (3.1)	0.20 μs

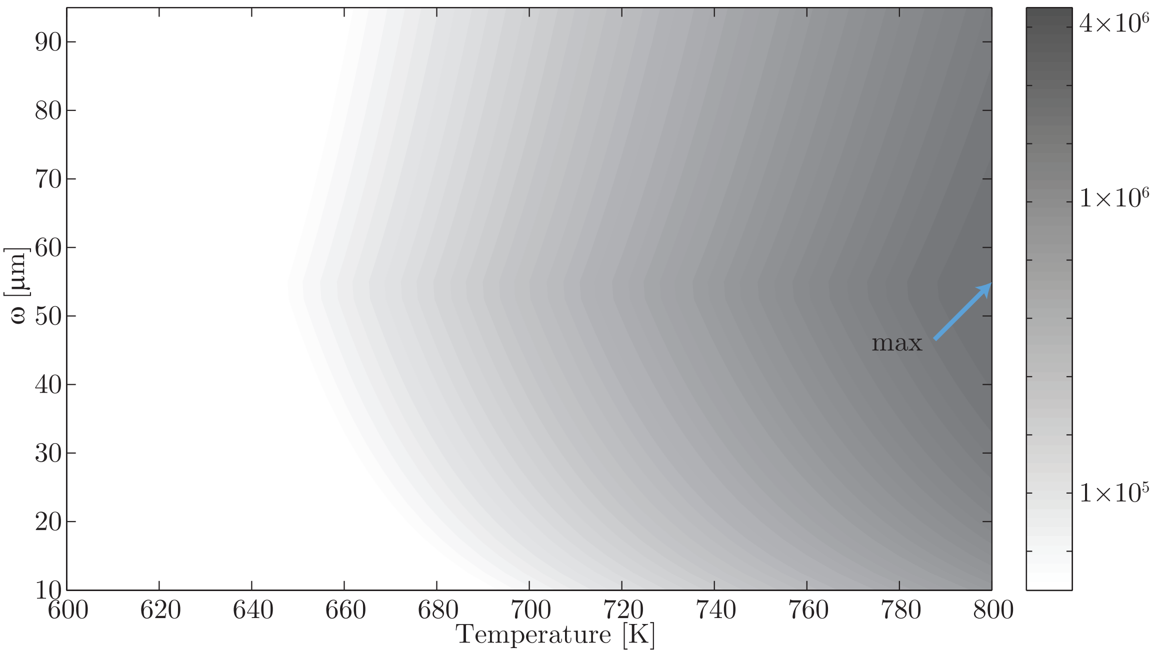

Figure 5.7: **$\dot{N}_D$ Magnitudes for Mg** The hot Mg detection rate $\dot{N}_D$ (2.1) of the E1-M1 transition is plotted for laser-beam radius ω_0 and vapor cell temperature T. The maximum $\dot{N}_{D\max} = 6.3 \times 10^6\,\mathrm{s}^{-1}$ is found at $\omega_0 = 55\,\mu$m and $T = 800$ K.

Table 5.9: Mg parameters at the $\dot{N}_{D\max}$.

Parameter		Value
$\dot{N}_{D\max}$	detection rate (2.1)	$6.3\times10^{+6}$ s^{-1}
ω_0	laser-beam radius	55 μm
T	vapor cell temperature	800 K
$P_{^3P_0}$	excitation probability (2.4)	2.3×10^{-10}
$\dot{N}_{\mathrm{tot}}$	atom interrogation rate (3.10)	$2.8\times10^{+18}$ s^{-1}
$\Omega_{R2\gamma}$	two-photon Rabi frequency (2.3)	$2.3\times10^{+2}$ Hz
$\bar{t}$	interrogation time (3.1)	0.13 μs

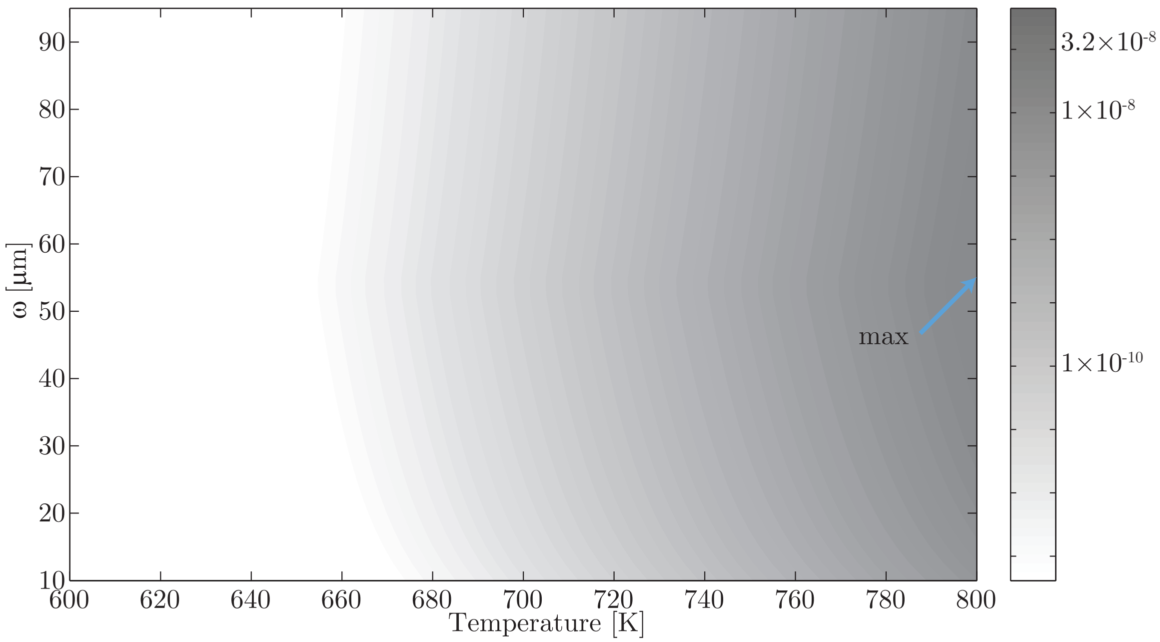

Figure 5.8: **$\dot{N}_D$ Magnitudes for Be** The hot Be detection rate $\dot{N}_D$ (2.1) of the E1-M1 transition is plotted for laser-beam radius ω_0 and vapor cell temperature T. The maximum $\dot{N}_{D\max} = 1 \times 10^{-7}\,\text{s}^{-1}$ is found at $\omega_0 = 55\,\mu$m and $T = 800$ K.

Table 5.10: Be parameters at the $\dot{N}_{D\max}$.

Parameter		Value
$\dot{N}_{D\max}$	detection rate (2.1)	1.0×10^{-7} s^{-1}
ω_0	laser-beam radius	55 μm
T	vapor cell temperature	800 K
$P_{^3P_0}$	excitation probability (2.4)	1.5×10^{-13}
$\dot{N}_{\text{tot}}$	atom interrogation rate (3.10)	$6.5\times10^{+7}$ s^{-1}
$\Omega_{R2\gamma}$	two-photon Rabi frequency (2.3)	9.7 Hz
$\bar{t}$	interrogation time (3.1)	0.08 μs

5.3 Stability results for group II type atoms

In this section you will find contour plots of each group II type atom's stability $\mathcal{S}$ magnitude with respect to temperature T and laser-beam radius ω_0. In calculation, laser-beam radius ω_0 was varied from 100 μm up to a 15 mm and vapor cell temperature was evaluated from room temperature (300 K) up to the optical damage threshold of 800 K. The subset of laser-beam radii and temperatures immediately surrounding the local minimum of stability $\mathcal{S}$ are displayed. The Hg result is remarkably distinct in temperature and radius from the other group II type atoms due to collision effects.

For insight into these plots, a characteristic example of a how $\Delta\nu$ in Ra scales for the non-Hg group II type atoms is shown in Figure 4.2 at 800 K, plotted with respect to laser-beam radius ω_0. The linewidth $\Delta\nu$ contributes linearly to the vertical-slice behavior of the contours displayed below. The equivalent $\Delta\nu$ plot for Hg is shown in Figure 4.3.

Insight into horizontal-slice scaling follows the number density ρ of atoms most strongly, shown with respect to temperature in Figure 3.6.

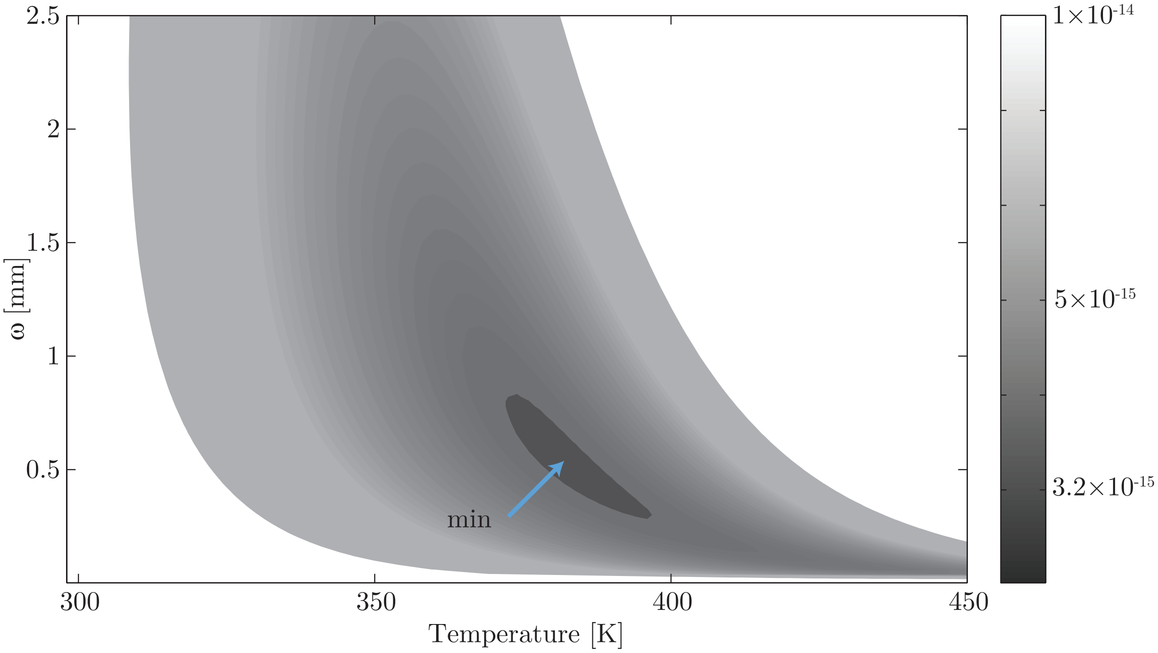

Figure 5.9: **$\mathcal{S}$ Magnitudes for Hg** The $\mathcal{S}$ (4.1) of a hot Hg E1-M1 clock is plotted for laser-beam radius ω_0 and vapor cell temperature T. $\mathcal{S}_{\text{min}} = 3.1 \times 10^{-15}\sqrt{\text{Hz}^{-1}}$ is found at $\omega_0 = 0.54$ mm and $T = 382$ K.

Table 5.11: Hg parameters at the $\mathcal{S}_{\text{min}}$.

Parameter		Value
$\mathcal{S}_{\text{min}}$	stability (4.1)	$3.1\times10^{-15}\ \sqrt{\text{Hz}^{-1}}$
ω_0	laser-beam radius	0.54 mm
T	vapor cell temperature	382 K
$P_{^3P_0}$	excitation probability (2.4)	7.5×10^{-8}
$\dot{N}_{tot}$	atom interrogation rate (3.10)	$3.8\times10^{+19}$ s^{-1}
$\Delta\nu$	effective linewidth - Table 4.1	$1.9\times10^{+5}$ Hz
$\Omega_{R2\gamma}$	two-photon Rabi frequency (2.3)	$1.0\times10^{+2}$ Hz
$\bar{t}$	interrogation time (3.1)	5.38 μs

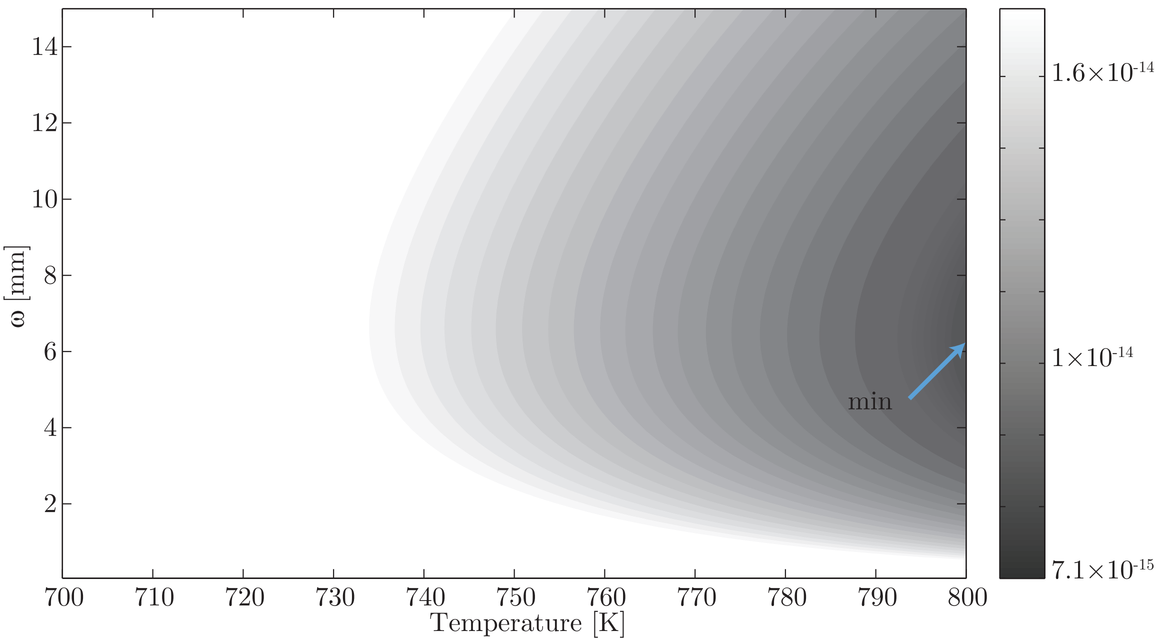

Figure 5.10: **$\boldsymbol{\mathcal{S}}$ Magnitudes for Ra** The $\mathcal{S}$ (4.1) of a hot Ra E1-M1 clock is plotted for laser-beam radius ω_0 and vapor cell temperature T. $\mathcal{S}_{\text{min}} = 7.1 \times 10^{-15}\sqrt{\text{Hz}^{-1}}$ is found at $\omega_0 = 6.3$ mm and $T = 800$ K.

Table 5.12: Ra parameters at the $\mathcal{S}_{\text{min}}$.

Parameter		Value
$\mathcal{S}_{\text{min}}$	stability (4.1)	$7.1\times10^{-15}\ \sqrt{\text{Hz}^{-1}}$
ω_0	laser-beam radius	6.3 mm
T	vapor cell temperature	800 K
$P_{^3P_0}$	excitation probability (2.4)	1.6×10^{-8}
$\dot{N}_{tot}$	atom interrogation rate (3.10)	$2.8\times10^{+18}$ s^{-1}
$\Delta\nu$	effective linewidth - Table 4.1	$2.8\times10^{+4}$ Hz
$\Omega_{R2\gamma}$	two-photon Rabi frequency (2.3)	$5.7\times10^{+0}$ Hz
$\bar{t}$	interrogation time (3.1)	46.02 μs

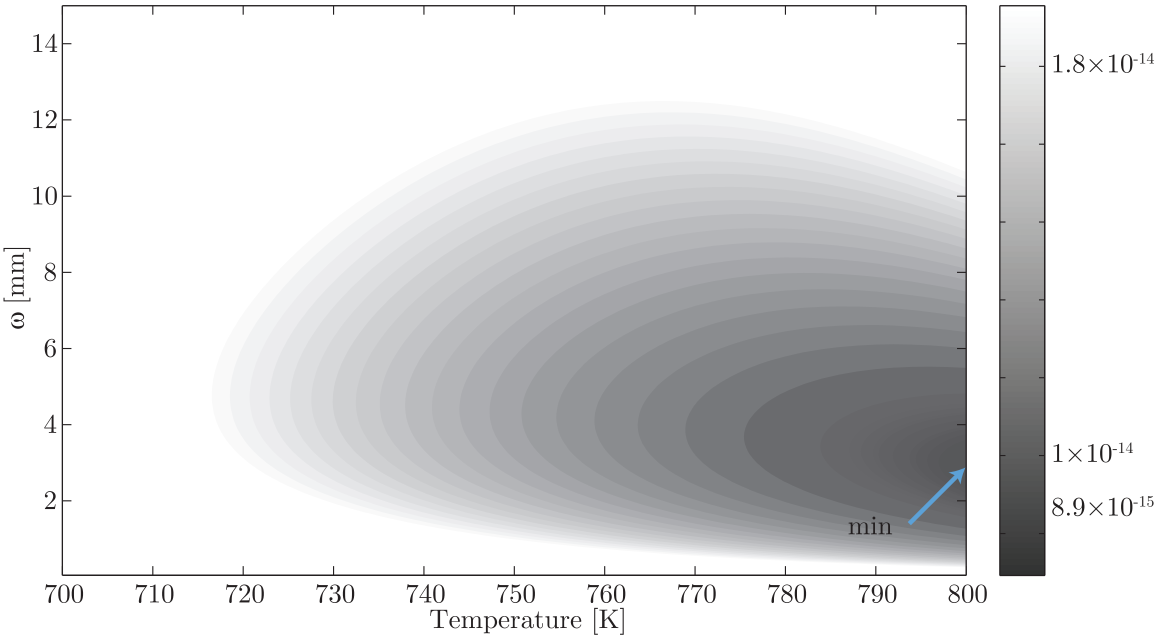

Figure 5.11: ***S* Magnitudes for Yb** The $\mathcal{S}$ (4.1) of a hot Yb E1-M1 clock is plotted for laser-beam radius ω_0 and vapor cell temperature T. $\mathcal{S}_{\text{min}} = 8.4 \times 10^{-15}\sqrt{\text{Hz}^{-1}}$ is found at $\omega_0 = 2.9$ mm and $T = 800$ K.

Table 5.13: Yb parameters at the $\mathcal{S}_{\text{min}}$.

Parameter		Value
$\mathcal{S}_{\text{min}}$	stability (4.1)	$8.4\times10^{-15}\ \sqrt{\text{Hz}^{-1}}$
ω_0	laser-beam radius	2.9 mm
T	vapor cell temperature	800 K
$P_{^3P_0}$	excitation probability (2.4)	7.7×10^{-9}
$\dot{N}_{tot}$	atom interrogation rate (3.10)	$1.7\times10^{+19}$ s^{-1}
$\Delta\nu$	effective linewidth - Table 4.1	$6.0\times10^{+4}$ Hz
$\Omega_{R2\gamma}$	two-photon Rabi frequency (2.3)	$9.6\times10^{+0}$ Hz
$\bar{t}$	interrogation time (3.1)	18.54 μs

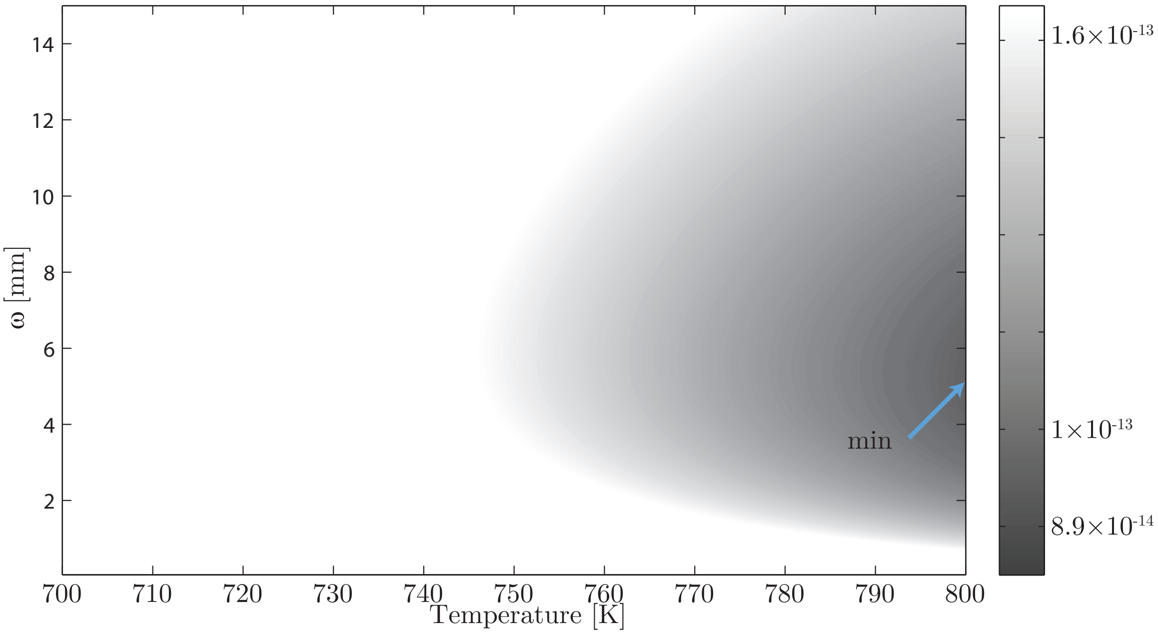

Figure 5.12: **$\mathcal{S}$ Magnitudes for Sr** The $\mathcal{S}$ (4.1) of a hot Sr E1-M1 clock is plotted for laser-beam radius ω_0 and vapor cell temperature T. $\mathcal{S}_{\text{min}} = 8.4 \times 10^{-14}\sqrt{\text{Hz}^{-1}}$ is found at $\omega_0 = 5.1$ mm and $T = 800$ K.

Table 5.14: Sr parameters at the $\mathcal{S}_{\text{min}}$.

Parameter		Value
$\mathcal{S}_{\text{min}}$	stability (4.1)	$8.4\times10^{-14}\ \sqrt{\text{Hz}^{-1}}$
ω_0	laser-beam radius	5.1 mm
T	vapor cell temperature	800 K
$P_{^3P_0}$	excitation probability (2.4)	1.5×10^{-10}
$\dot{N}_{tot}$	atom interrogation rate (3.10)	$7.2\times10^{+18}\ \text{s}^{-1}$
$\Delta\nu$	effective linewidth - Table 4.1	$5.3\times10^{+4}$ Hz
$\Omega_{R2\gamma}$	two-photon Rabi frequency (2.3)	1.1 Hz
$\bar{t}$	interrogation time (3.1)	23.20 μs

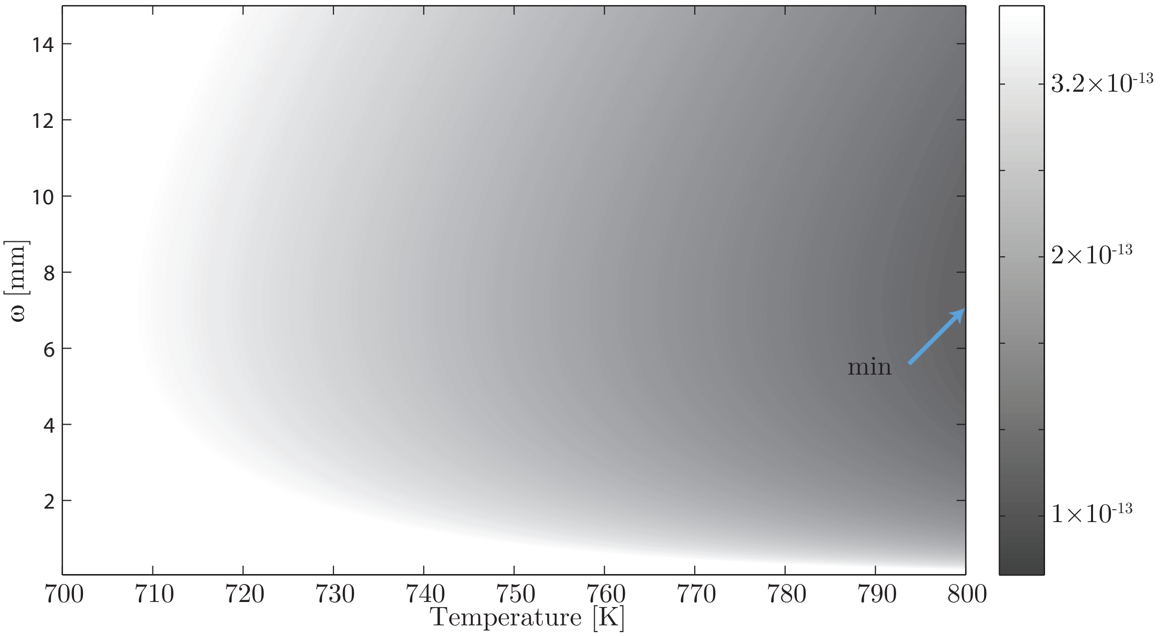

Figure 5.13: **$\mathcal{S}$ Magnitudes for Ba** The $\mathcal{S}$ (4.1) of a hot Ba E1-M1 clock is plotted for laser-beam radius ω_0 and vapor cell temperature T. $\mathcal{S}_{\text{min}} = 8.5 \times 10^{-14}\sqrt{\text{Hz}^{-1}}$ is found at $\omega_0 = 7.1$ mm and $T = 800$ K.

Table 5.15: Ba parameters at the $\mathcal{S}_{\text{min}}$.

Parameter		Value
$\mathcal{S}_{\text{min}}$	stability (4.1)	$8.5\times10^{-14}\ \sqrt{\text{Hz}^{-1}}$
ω_0	laser-beam radius	7.1 mm
T	vapor cell temperature	800 K
$P_{^3P_0}$	excitation probability (2.4)	1.4×10^{-9}
$\dot{N}_{tot}$	atom interrogation rate (3.10)	$3.2\times10^{+17}$ s^{-1}
$\Delta\nu$	effective linewidth - Table 4.1	$3.3\times10^{+4}$ Hz
$\Omega_{R2\gamma}$	two-photon Rabi frequency (2.3)	1.9 Hz
$\bar{t}$	interrogation time (3.1)	40.43 μs

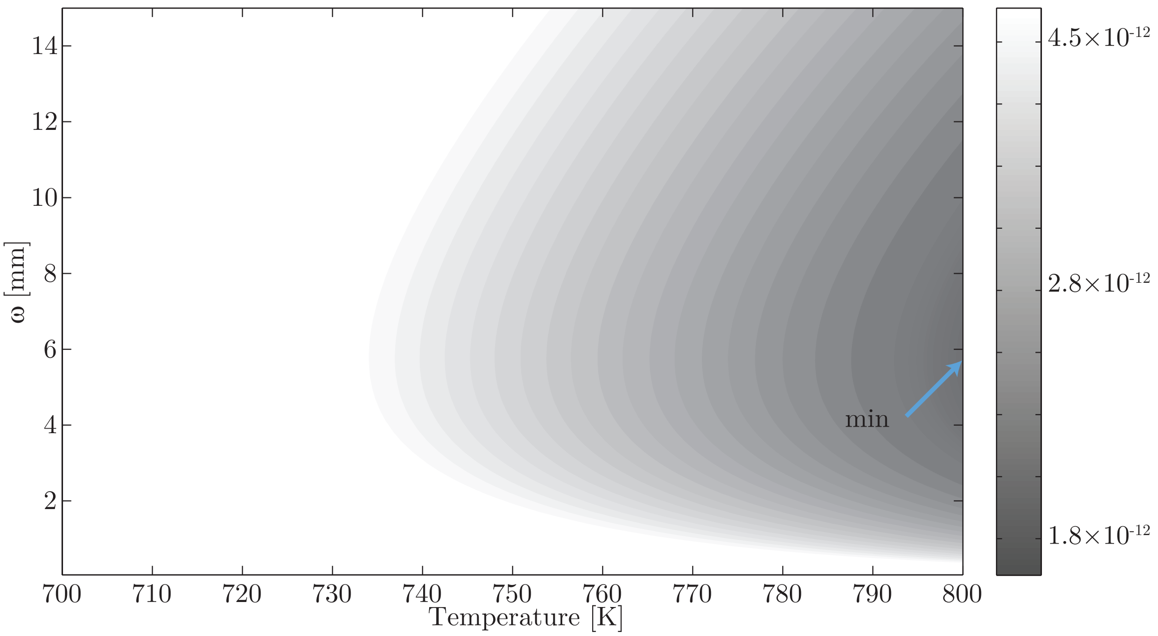

Figure 5.14: **$\mathcal{S}$ Magnitudes for Ca** The $\mathcal{S}$ (4.1) of a hot Ca E1-M1 clock is plotted for laser-beam radius ω_0 and vapor cell temperature T. $\mathcal{S}_{\text{min}} = 2.7 \times 10^{-12}\sqrt{\text{Hz}^{-1}}$ is found at $\omega_0 = 5.7$ mm and $T = 800$ K.

Table 5.16: Ca parameters at the $\mathcal{S}_{\text{min}}$.

Parameter		Value
$\mathcal{S}_{\text{min}}$	stability (4.1)	$1.7\times10^{-12}\ \sqrt{\text{Hz}^{-1}}$
ω_0	laser-beam radius	5.7 mm
T	vapor cell temperature	800 K
$P_{^3P_0}$	excitation probability (2.4)	2.7×10^{-12}
$\dot{N}_{tot}$	atom interrogation rate (3.10)	$1.5\times10^{+18}$ s^{-1}
$\Delta\nu$	effective linewidth - Table 4.1	$7.5\times10^{+4}$ Hz
$\Omega_{R2\gamma}$	two-photon Rabi frequency (2.3)	1.9×10^{-1} Hz
$\bar{t}$	interrogation time (3.1)	17.54 μs

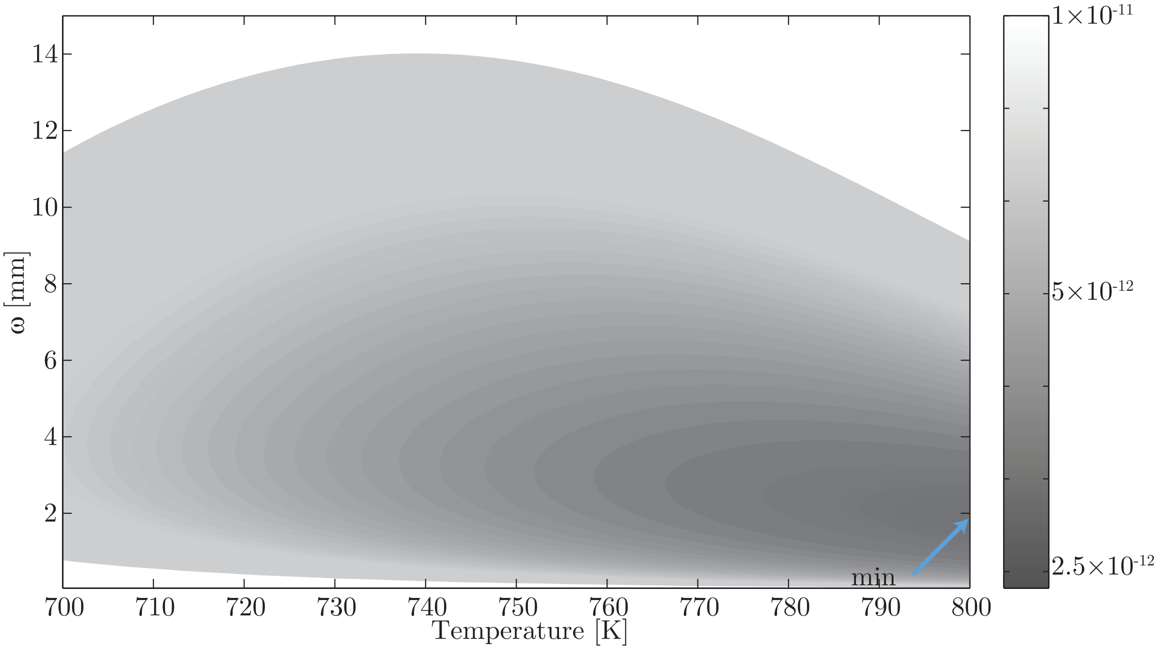

Figure 5.15: **$\mathcal{S}$ Magnitudes for Mg** The $\mathcal{S}$ (4.1) of a hot Mg E1-M1 clock is plotted for laser-beam radius ω_0 and vapor cell temperature T. $\mathcal{S}_{\text{min}} = 2.4 \times 10^{-12}\sqrt{\text{Hz}^{-1}}$ is found at $\omega_0 = 4$ mm and $T = 800$ K.

Table 5.17: Mg parameters at the $\mathcal{S}_{\text{min}}$.

Parameter		Value
$\mathcal{S}_{\text{min}}$	stability (4.1)	$2.4\times10^{-12}\ \sqrt{\text{Hz}^{-1}}$
ω_0	laser-beam radius	1.9 mm
T	vapor cell temperature	800 K
$P_{^3P_0}$	excitation probability (2.4)	1.9×10^{-13}
$\dot{N}_{tot}$	atom interrogation rate (3.10)	$9.7\times10^{+19}$ s^{-1}
$\Delta\nu$	effective linewidth - Table 4.1	$2.4\times10^{+5}$ Hz
$\Omega_{R2\gamma}$	two-photon Rabi frequency (2.3)	1.9×10^{-1} Hz
$\bar{t}$	interrogation time (3.1)	4.55 μs

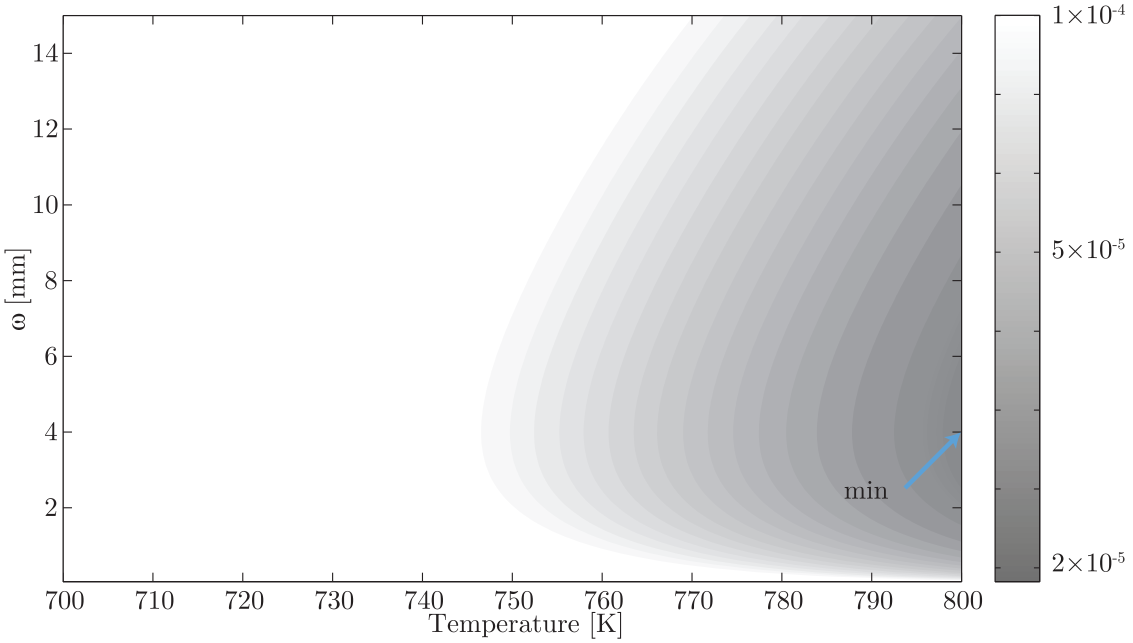

Figure 5.16: **$\boldsymbol{\mathcal{S}}$ Magnitudes for Be** The $\mathcal{S}$ (4.1) of a hot Be E1-M1 clock is plotted for laser-beam radius ω_0 and vapor cell temperature T. $\mathcal{S}_{\text{min}} = 1.9 \times 10^{-5}\sqrt{\text{Hz}^{-1}}$ is found at $\omega_0 = 4$ mm and $T = 800$ K.

Table 5.18: Be parameters at the $\mathcal{S}_{\text{min}}$.

Parameter		Value
$\mathcal{S}_{\text{min}}$	stability (4.1)	$1.9\times10^{-5}\ \sqrt{\text{Hz}^{-1}}$
ω_0	laser-beam radius	4 mm
T	vapor cell temperature	800 K
$P_{^3P_0}$	excitation probability (2.4)	2.7×10^{-17}
$\dot{N}_{tot}$	atom interrogation rate (3.10)	$4.7\times10^{+9}$ s^{-1}
$\Delta\nu$	effective linewidth - Table 4.1	$2.3\times10^{+5}$ Hz
$\Omega_{R2\gamma}$	two-photon Rabi frequency (2.3)	1.8×10^{-3} Hz
$\bar{t}$	interrogation time (3.1)	5.86 μs

5.4 Broadening Budget

Table 5.19: Broadening and shift budget for the monochromatic E1-M1 Hg clock at the temperature (380 K) and laser-beam radius (0.6 mm) where the minimum $\mathcal{S}$ is found.

Mechanism	Broadening [Hz]	Shift [Hz]
Transit	$2{\times}10^5$	0
Doppler 1st	$4{\times}10^4$	0
Doppler 2nd	90	-90
BBR	10^{-16}	-1.7
Stark	314	$1.6{\times}10^4$
Natural	0.45	0
$\Delta\nu$	$2{\times}10^5$	
ν_B		$1.6{\times}10^4$

5.5 Gravitational Redshift Sensitivity

We can report the time-to-meterstick and one second elevation sensitivity of each of these hot group II type clocks. See §4.2 for a discussion of the gravitational redshift ν_G sensitivity of oscillators.

Table 5.20: Gravitational Redshift Sensitivity

Atom	Time-to-meterstick [hrs]	1 s elevation resolution [m]
Hg	0.23	29
Ra	1.2	65
Yb	1.6	77
Sr	170	770
Ba	170	780
Ca	6.4×10^4	1.5×10^4
Mg	1.4×10^5	2.2×10^4
Be	8.6×10^{18}	1.8×10^{11}

5.6 Why Hot Atoms?

We find that most atoms have optimally small $\mathcal{S}$ and optimally large $\dot{N}_D$ at high temperatures. This is because, for most atoms, the statistical advantage of a larger sample size outweighs the harm from broadening due to thermal effects. These species improve with arbitrarily high heating. The exception is Hg, which prefers the hotter than room temperature (273 K) thermal environment of 380 K. Hg is optimized at less than the optical damage threshold of 800 K because it is more sensitive to collisions at these temperatures than the other group II type atoms. The incidental benefit of optimal $\mathcal{S}$ at these high temperatures is the portability advantage it introduces.

5.7 Viability of a Hg Standard

Hg is a very desirable species for a hot E1-M1 clock. Its high number density ρ is the main virtue that catapults it to the best species for both $\dot{N}_D$ and $\mathcal{S}$. The off-the-shelf availability of the monochomatic scheme's wavelength (531 nm) and the $^3P_0 \to {}^3S_1$ detection wavelength (405 nm) is convenient. So is the availability of off-the-shelf steering and filtering optics, such as mirrors, waveplates, and interference filters. Finally, heating a vapor cell to 380 K (the optimal T for minimal $\mathcal{S}$) is easy and can be done in a portable set-up. Together these features make developing and deploying an E1-M1 standard in hot Hg a viable scheme.

CHAPTER VI

Bichromatic E1-M1 Optical Clock Elimination of Light Shift

Introducing a second excitation laser frequency in the E1-M1 clock scheme creates an opportunity to eliminate the light shift ν_{LS} completely. Light shift is discussed in §4.1.3.

Current lattice clocks use the clock atom's magic wavelength for atom trapping to balance the dynamic light shift of the ground and clock levels due to the lattice laser [49, 41]. These systems remain subject to a light shift from the excitation beam, although this is fairly small due to the low laser powers required to drive the transition, and especially small when compared to the large shift of the E1-M1 scheme. The magic wavelength is the wavelength where the dynamic dipole polarizability of the $^1S_0$ ground state, $\alpha_{^1S_0}(\lambda)$, and the $^3P_0$ clock-state, $\alpha_{^3P_0}(\lambda)$, are equal. Even though a light shift occurs in both levels while they are addressed by a light field at the magic wavelength, the shifts are equal in magnitude and sign so the effective transition frequency matches the natural transition frequency. The magic wavelength has been calculated for many group II type neutral atoms [52, 16]. Methods to mediate the impact of the light shift on an optical clock transition by the excitation light have been explored directly [55] or by extension [26, 54].

Complete elimination of the light shift during excitation is possible in an E1-M1 clock with dual frequencies. Wavelengths (λ) can be selected to together resonate with the transition and the laser intensity for each λ can be chosen to offset light shift differences perfectly. The dynamic dipole polarizabilities of neutral Hg have been calculated across optical wavelengths above and below the two-photon transition wavelength $2\lambda_{^3P_0} = 531$ nm [52] which is adequate to evaluate magic wavelength pairs that will fully eliminate the light shift during optical excitation of the clock transition in Hg.

6.1 Bichromatic E1-M1: Hg

From dynamic polarizability calculations performed elsewhere that found the one-photon (E1 scheme) magic wavelength in Hg [52], we can determine pairs of excitation wavelengths that can be chosen to offset the light shift during excitation. The dynamic polarizability introduces a shift to the energy E of the system as:

$$\Delta E = -\alpha(\omega)F^2 + \cdots \tag{6.1}$$

where F is the electric field.

Figure 6.1 plots the dynamic dipole polarizability difference in Hg, $\Delta\alpha(\lambda) = \alpha_{^3P_0}(\lambda) - \alpha_{^1S_0}(\lambda)$. This difference has been measured as zero at 362.53 nm [53], the magic wavelength used for trapping neutral Hg for a lattice clock. The goal is to find wavelength and laser intensitiy pairs that together offset the light shift. The matching pair of wavelengths must together be resonant with the clock transition. The two-photon transition wavelength is $\lambda_{2\gamma} = 531$ nm, and a bichromatic pair of resonant wavelengths will be found on opposite sides this wavelength. We plot all the pairs of wavelength which are resonant with the transition frequency in Figure 6.2 (a).

For the specific case of two, equal intensity beams, there exists a pair of magic

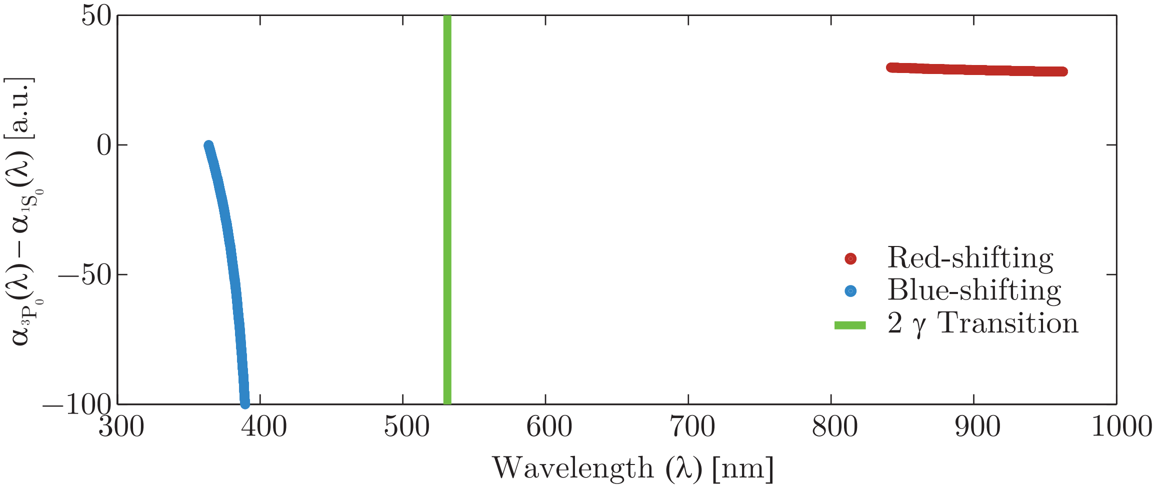

Figure 6.1: **Dynamic Dipole Polarizability Difference** $\Delta\alpha(\lambda)$ between the ground $^1S_0$ and clock $^3P_0$ levels. The two-photon transition wavelength $\lambda_{2\gamma} = 531$ nm is shown. Calculation data from [52].

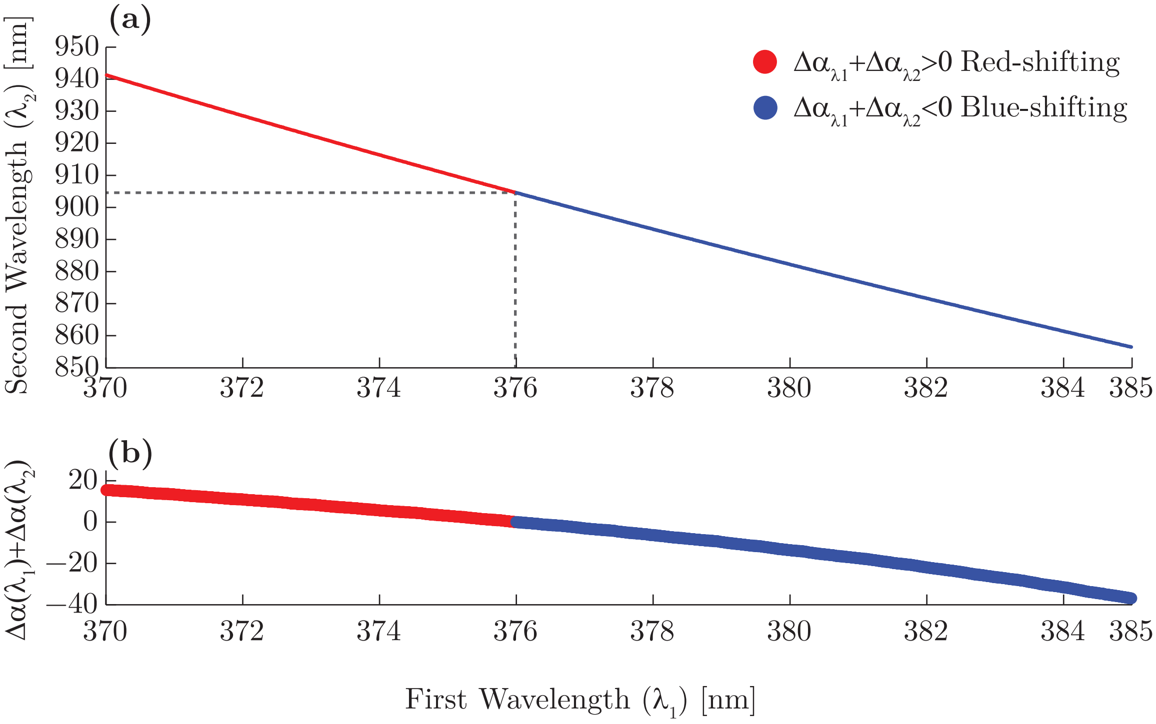

Figure 6.2: **E1-M1 Magic Wavelength Pairs in Hg**(a) Resonant pairs color-coded equal laser power shift and (b) the sum of $\Delta\alpha(\lambda)$ for each resonant pair. Calculation data from [52].

wavelengths where for equal intensity beams this resonant photon pair exactly offsets the light shift, shown in Figure 6.2 (b) where $\Delta\alpha(\lambda_1) - \Delta\alpha(\lambda_2) = 0$. See Table 6.1 for the calculated $\Delta\alpha(\lambda)$ of this particular case in Hg.

Table 6.1: A magic wavelength pair for neutral Hg is shown. This pair of wavelengths (λ_1 and λ_2) eliminate the light shift when the electric field F of each laser is equal in magnitude. The dynamic dipole polarizability of the ground state $\alpha_{^1S_0}(\lambda)$ and clock state $\alpha_{^3P_0}(\lambda)$ are listed along with the dynamic dipole polarizability difference $\Delta\alpha(\lambda)$. These values were calculated in [52].

$\lambda[nm]$	$\alpha_{^1S_0}(\lambda)$ [a.u.]	$\alpha_{^3P_0}(\lambda)$ [a.u.]	$\Delta\alpha(\lambda)$
376	39	10	-29
905	32	61	$+29$

A bichromatic scheme enjoys a smaller intermediate detuning Δ from the $^3P_1$ level than the monochromatic scheme, this will lead to a relative increase in the resonant two-photon Rabi frequency $\Omega_{R2\gamma}$ (2.3). The specific two-photon Rabi frequency of the magic pair solution in Table 6.1 will be a factor of 4.9 larger than the monochromatic solution of the hot Hg clock. Excitation probability $P_{^3P_0}$ estimates based on adiabatic elimination of the intermediate level may begin to degrade [9] with reduced intermediate detuning Δ. Implementation of a bichromatic method to eliminate a light shift will elevate first-order Doppler broadening to unacceptable levels in a hot clock by degrading the Doppler free spectroscopy with $|\mathbf{k}_1| \neq |\mathbf{k}_2|$, see §4.1.4.1. A bichromatic E1-M1 clock will require ultracold atoms. Conveniently, either excitation beam can serve as a red-detuned optical dipole trap cycling on the 265 nm $^1S_0 \overset{\text{E1}}{\longleftrightarrow} {^3P_1}$ transition. The trap laser can combine with its magic pair from another laser to complete a bichromatic E1-M1 excitation. These lasers introduce offsetting light shifts and completely negate the light shift bias ν_{LS} while exciting the transition.

Offsetting light shift ν_{LS} requires accurate laser power metrology. With such metrology, other wavelength pairs can be selected with unequal laser powers that have been scaled to balance dynamic dipole polarizability differences.

CHAPTER VII

Experimental Equipment

7.1 Experimental Accomplishments

We were able to build a high-power, narrow-linewidth laser and scan over the known transition frequency of ^{201}Hg [40]. We explored two detection schemes and achieved excellent signal-to-noise potential in our system. Alas, we did not detect the E1-M1 transition despite building many excellent tools toward that goal. This chapter discusses those efforts and the technologies developed.

7.2 Iodine Spectroscopy

We were confident that our laser system could scan over the ^{201}Hg clock transition because we were able to scan over a known molecular Iodine resonance and we knew the exact transition frequency of the Fermionic isotopes due to single-photon clock work performed by [40]. A successful scan of the Iodine (R126(36-0)) line is shown in Figure 7.2. This Iodine line is useful due to its proximity to the known and estimated lines of neutral Hg, the spectra of molecular Iodine and Hg are shown together in Figure 7.1 [21, 40].

The Iodine spectroscopy also confirmed that we had, at most, a 1 MHz laser linewidth. The ability to resolve spectral features at the frequency resolution of our

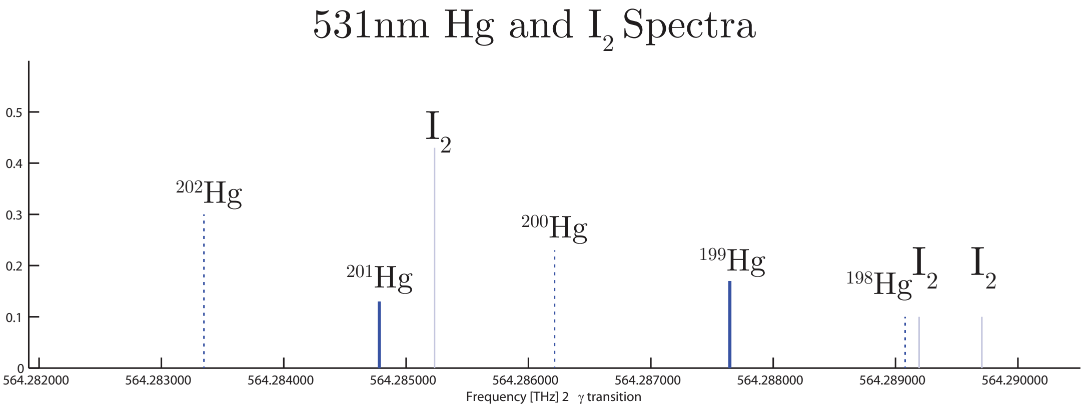

Figure 7.1: **Iodine and Hg Spectra** Absolute centers of the I_2 and known Hg lines [21, 40]. The Bosonic line centers of Hg are imputed by assuming uniform separation of all isotopes.

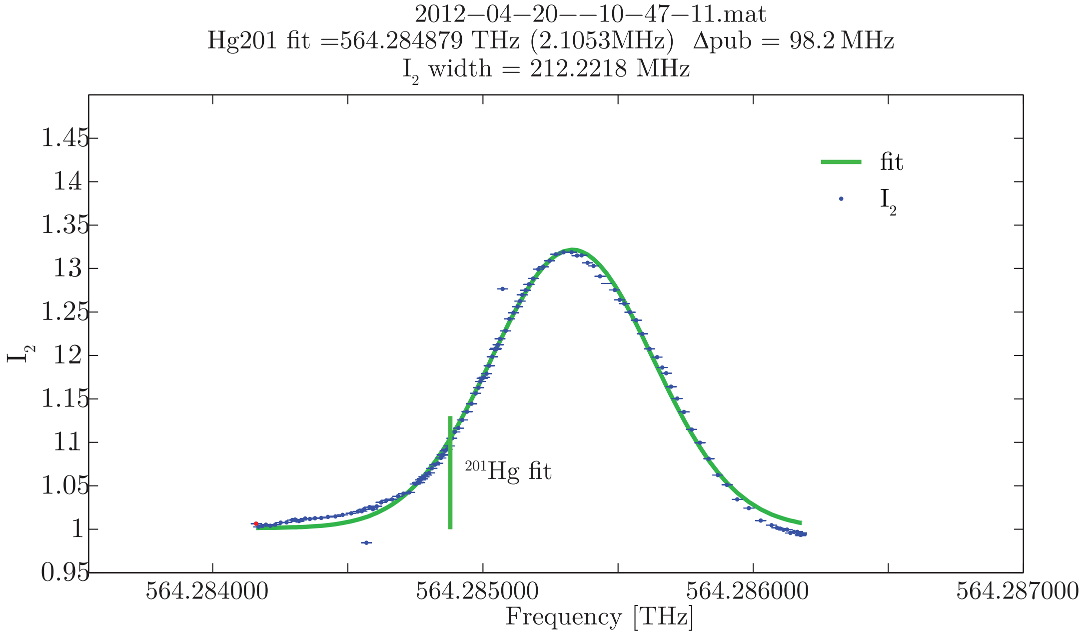

Figure 7.2: **Iodine signal with clock laser at 531-nm** Please note the displayed frequency is the reported directly from the wavemeter which had a large absolute frequency shift but a negligible relative shift over the frequency window we scanned.

wavemeter indicates that the laser being measured has a frequency linewidth that is at most the detection resolution of that frequency measurement system. In the worst case scenario of 1 MHz actual laser linewidth (larger than the 1 kHz specified) we would still expect signal, although diluted by factor of five from the effective transition linewidth of 200 kHz (See Table 5.19) divided by the laser linewidth (1 MHz). The effective laser intensity driving an optical transition is only the resonant intensity.

The ^{201}Hg transition frequency overlaps the thermal (300 K) Iodine reference line (R126(36-0)), and is offset from the center of that line by about 400 MHz. We implemented a two-stage AOM frequency shift scheme to permit a methodical scan for the Hg reference that was ultimately abandoned due to the adequate resolution of our wavemeter (High Finesse - WS Ultimate 10 MC8). An Iodine locking scheme would be helpful if a two-degree-of-freedom search were required for implementation of the $^3S_1$ detection scheme discussed in section 7.6.

7.3 Alignment Angle θ precision

The optical path length from the SHG crystal to the interrogation and detection region is approximately 1.2 m. We can set the retroreflection polarization rotation such that some light returns to the SHG crystal. We can visually overlap the retroreflection beam to the input beam with an estimated resolution of 0.5 mm. This allowed us to experimentally assume an alignment angle θ of 0.2 milliradians. This introduces a factor of 2 increase to the $\Delta\nu_{D1}$ calculated magnitudes of this dissertation. Figure 3.2 depicts the alignment angle in a vapor cell geometry.

7.4 Monochromatic E1-M1 Laser System

The viability of the monochromatic E1-M1 optical frequency standard relies on the construction of a high-power, narrow-linewidth, resonant system. We constructed

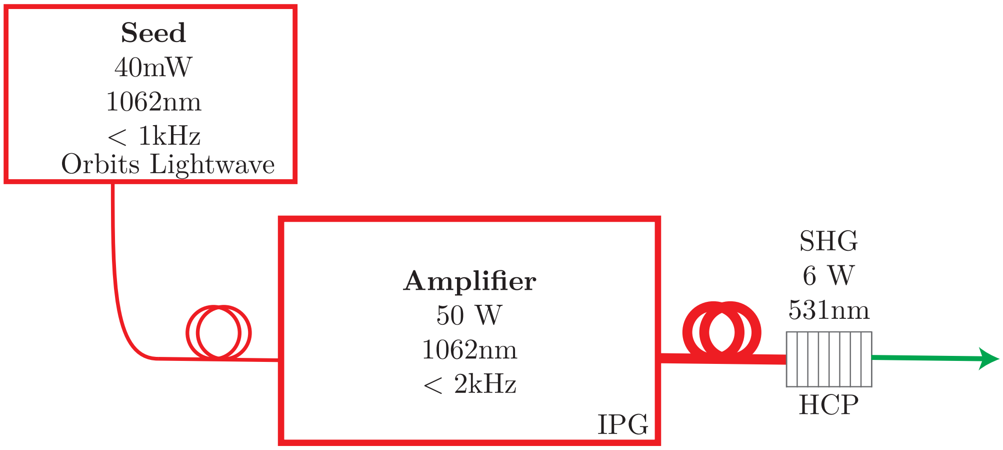

Figure 7.3: **Schematic of Laser System** The high-power narrow-linewidth laser system has three components, an infrared (IR) seed laser, an IR amplifier, and a SHG crystal that produces CW 531 nm green light needed to excite the E1-M1 transition.

an 8 W, 531 nm, and sub-kHz laser source.

An auspicious feature of neutral Hg is the ubiquity of its E1-M1 scheme wavelengths. The degenerate two-photon resonant excitation is at 531 nm. Hand-held laser pointers are 532 nm because that is a simple frequency conversion from the commonly found Nd:YAG wavelength of 1064 nm. We were able to purchase a high power 1062 nm system because a line-center difference of 2 nm in the infrared is well within the construction capability of most laser manufacturers.

Narrow-linewidth is also an essential feature in an excitation laser because excitation probability is the convolution of the effective linewidth of the atomic system and the laser frequency linewidth. The two-photon Rabi frequency only depends on resonant laser intensity, so when $\Delta\nu_{LL} >> \Delta\nu_{nat}$ only a subset of the total laser intensity contributes to excitation probability.

The final laser system we constructed was able to meet both experimental requirements of being high power and narrow linewidth. It is a three-stage system with an extremely narrow-linewidth seed laser at 1062 nm. That infrared seed is amplified up to 50 W with no measurable increase in linewidth. Finally, that high power beam is frequency doubled after a single-pass through a periodically poled crystal.

7.4.1 Narrow-linewidth Seed Laser

The laser system begins with a narrow-linewidth 1062 nm laser. Narrow-linewidth immediately demands a CW laser (as opposed to a pulsed laser). The magnitude "narrow" is only meaningful in comparison with the linewidth of the transition. Free-running CW cavity lasers can have off-the-shelf linewidths of about 1 MHz. Free-running simply means no external control corrects the laser cavity length which is how the frequency stability is usually maintained.

The seed laser (Orbits Lightwave - Ethernal) was delivered with a free-running specification of sub-kHz linewidth. This laser is the size of a small, paperback book and is therefore portable. We were only able to confirm MHz level resolution with an external system using an Iodine reference cell, see §7.2. We didn't have an independent means of confirming the sub-kHz laser linewidth specification, but never observed contradicting evidence. The seed laser system contained external locking mechanisms which had the potential to reduce the linewidth further with the help of an external resonator. For a hot Hg E1-M1 clock, the dominant broadening mechanism in the atomic system is transit broadening Δ_{TT} with a magnitude of approximately 200 kHz, see Table 5.19. This transit broadening is far greater than the estimated free-running laser linewidth.

7.4.2 High-power Infrared Amplifier

The laser amplifier (IPG YAR-50K-1064-LP-SF) can amplify between 2 and 10 mW of 1062 nm light up to 50 W of output power. This amplifier is about the size of a suitcase, less than 0.1 m^3 in volume, and therefore maintains the portability of this experiment. A member or our group performed homodyne detection on the system, comparing the input seed lasers frequency to output light from the amplifier that had been offset slightly with an Acousto-Optic Modulator (AOM). The homodyne detection method involved interfering amplified and offset IR light with the seed IR light and looking at the frequency width of the beat note. The frequency resolution of detection was measured by applying a random noise source directly to a secondary arm of the seed laser that was offset and then interfering that modulated arm with the unmodulated arm of the seed in the interferometer. The applied noise had a noise floor of 4 kHz and the detector was sensitive to that small signal. When the amplifier output replaced the artifically noisy arm of the homodyne system, less than 10 Hz of noise was observed. This does not guarantee that the fundamental linewidth is this small, but it does guarantee that the amplifier can protect a narrow linewidth source.

7.4.3 Single Pass SHG

The final stage of the monochromatic laser system is frequency doubling by SHG. We were able to use a logistically simple, single-pass periodically-poled crystal. The efficiency of SHG is measured in $\%/W$ where the laser-beam radius in the crystal is captured by the separately reported focusing parameter ξ. The most common variety of periodically-poled crystal is PPLN; the specific crystal type we selected has robust properties for high laser intensities. We used Periodically Poled MgO-Doped : Stoichiometric Lithium Tantalate (PPMgO:SLT) as our SHG crystal with period 7.87 μm. The PPMgO:SLT-type of SHG crystal has measured conversion efficiencies of 1.7%/W at 1064 nm in a 30 mm crystal (the focusing parameter was $\xi = 2.48$ in a 30 mm crystal which matched the Rayleigh range to the crystal length) [46]. Since conversion efficiency increases with incident power, increasing the power of the pump laser is important. Pulsed sources (like in a hand-held laser pointer) have high instantaneous intensities and can achieve high conversion efficiency with only one trip through an SHG crystal to produce green output light. In low-power CW systems, a generic SHG crystal can be placed in a multi-pass cavity. High output powers can be achieved with active locking of the multi-pass cavity length, a complex and expensive scheme.

We must use a continuous-wave source in a frequency standard, which limits our peak intensity compared with pulsed systems, but the required high powers for E1-M1 transitions have high conversion efficiencies in a simple single-pass SHG setup. Single-pass is the self-explanatory alternative to multi-pass where a pump beam passes through the crystal only once and does not require active cavity-locking electronics. Periodically-poled materials have improved enough to tolerate high power pump lasers. While we achieved as much as 8 W of 531 nm, we more commonly operated with 6 W of green light from 26 W of 1062 nm, IR light in a single-pass system, an efficiency of 23%. This was measured using a Coherent LabMax_TOP detector with the PM30 thermopile sensor head.The synthetic construction of periodic crystals for second harmonic generation is an old technology [19]. Materials have advanced such that the quantum efficiency of conversion and damage threshold are at a level where it is appropriate to expect a 10 W laser in a portable package [46].

7.5 Imaging System - Detection

For an estimate of 10 W of resonant green laser power (that is effectively 20 W in the cell with retro-reflection) we expect 10^{12} clock atom scattering events in the blue per second. This compares to the 10^{27} green photons in the interrogation window from the 20 W of excitation light during the same period. Fortunately the spatial collimation of the laser means that most excitation light doesn't enter the detection imaging system. We must still contend with Rayleigh scattered and surface scattered light arriving at the detector. To detect any blue signal we needed to implement filtering. Optical Depth (OD) is a metric that characterizes how much

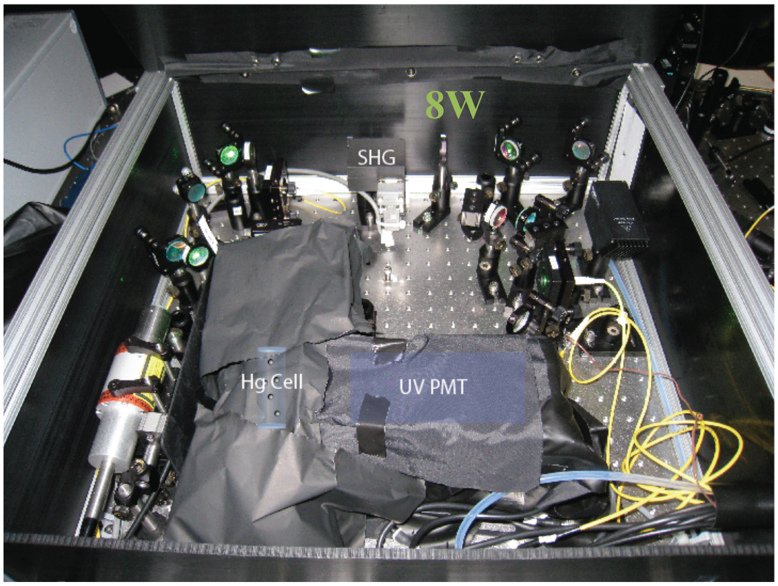

Figure 7.4: **Physical Experiment** A 60 cm × 60 cm area contained the final, SHG stage of the laser, the hot vapor cell, and the detector.

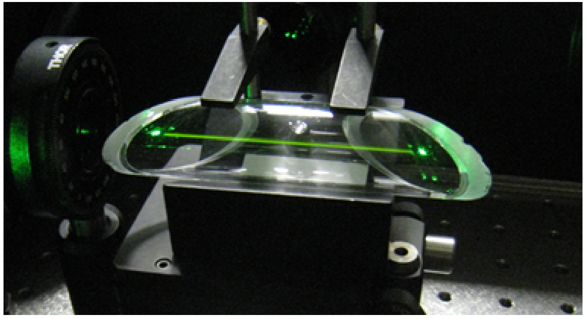

Figure 7.5: **Illuminated Iodine** The narrow-linewidth, 531 nm laser was able to scan a resonance of molecular Iodine (R126(36-0)) and scatter green light.

light is extinguished by a medium where 10^{-OD} is the light attenuation. An OD of 1 is equivalent to 90% extinction of signal. To characterize the collection efficiency of the system we keep track of the OD of each stage because OD magnitudes add linearly.

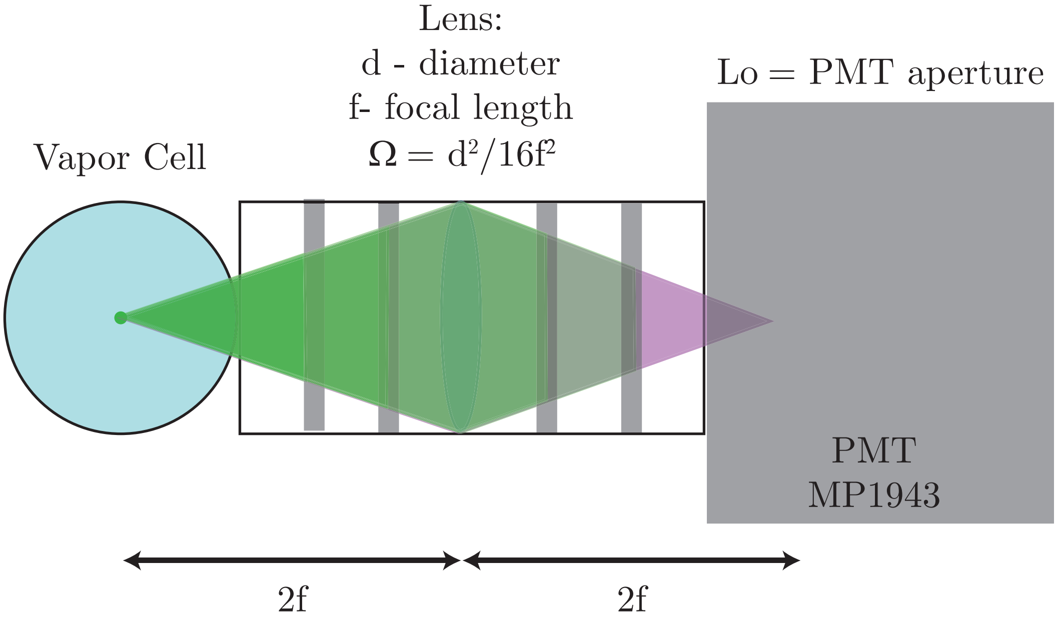

Figure 7.6: **A 1:1 Imaging System** An example detection system, with a UV sensitive PMT, filters, and an imaging lens placed 2f from the image and object planes.

A 1:1 imaging system is an efficient way to map a detection region onto a detector. A lens of diameter d is placed two focal lengths f away from the detection region, see Figure 7.6.

7.5.1 Collection Angle

The proximity of the lens and the diameter of the lens limit the percentage of solid angle that we can observe. For the 1:1 imaging system we implemented with 2.5 cm diameter lens with focal length of 2.5 cm located 5 cm away. We collect 6.8% of the solid angle, this collection solid angle is equivalent to an OD of 1.2. For detection by NH_3 relaxation, there is no dipole radiation pattern to enhance a region of solid angle.

For a $^3S_1$ detection, the $^3S_1 \rightarrow {}^3P_1$ detection line is a $J_i = 1 \rightarrow J_f = 1$ transition without the dipole radiation enhancement that can be created in $J_f = 0$ systems.

7.5.2 Filters

We implemented narrow-band, 531 nm filters to extinguish scattered green light from the excitation beam at the detector. Through multiple filters and quantum inefficiency at 531 nm by the detector, we were able to extinguish green background with an estimated OD of 20. We were unable to test the full OD suppression because it would require direct incidence of the laser onto the optics which would exceed the damage threshold of those filtering optics. There is no need to filter direct laser incidence because the only light we are concerned with is ambient scattered green light.

The interference filters (AT350 and NT49-817) were quite transparent at our wavelengths of interest. We had a 385 nm laser and were able to confirm that the OD of the filter system was < 2.2. The total filtering of the system is shown in Table 7.1

Table 7.1: Optical attenuation of signal (300-400 nm) and noise (531 nm) for the NH_3 system

Filtering Element	531 nm OD	350 nm OD
Solid Angle Ω	1.2	1.2
Detector (MP1943)	1.3	0.7
3×Filter (AT350)	3×5	3×0.8
Filter (NT49-817)	4	0.05
OD_{tot}	21.5	4.4

Signal-to-noise was further improved by encapsulating the Photo-multiplier Tube (PMT) and the interrogation region with an opaque enclosure. Small holes (1 cm diameter) were drilled into the enclosure to give the laser access to the vapor cell. This process resulted in a green photon counting rate of 190 Hz for 6 Watts of incident excitation laser power.

7.6 Detection Channels

We explored two detection schemes to observe ${}^3P_0$ occupation in neutral Hg. We tried a passive scheme where a buffer gas of NH_3 can relax atoms with clock level occupation through collision and produce a relaxation signal photon in the UV. We also began the exploration of an active, subsequent excitation from the clock level ${}^3P_0 \rightarrow {}^3S_1$. Hg is a well studied system and the ${}^3P_0 \rightarrow {}^3S_1$ transition has been observed in discharge lamp experiments from the turn of the 20th century, see the quicksilver "Quecksilberlichtbogen" spectra observed in [31]. These schemes are discussed here.

7.6.1 Passive: NH_3

Vapor cells of Hg with a buffer gas of NH_3 have been able to directly detect ${}^3P_0$ clock level occupation [39]. The branching behavior of highly excited Hg includes relaxation into the dark ${}^3P_0$ clock level. To recover the dark ${}^3P_0$ branching fraction; [39] observed that a buffer gas of NH_3 induced excimer relaxation of ${}^3P_0$ with a signal photon in the UV. The spectrum of this cascade channel is broad, 300-400nm. We included a buffer gas of NH_3 in our Hg cell and selected a detector (MP1490) with high quantum efficiency in the UV to detect these relaxation photons that would signal clock level occupation.

Our best effort to drive and detect the E1-M1 transition the NH_3 scheme had a background count uncertainty of 40 counts per second after 70 minutes of experiment time. Our imaging system for this measurement had an effective OD 4.4, see Table 7.1. True scattered signal would be attenuated by this factor of $10^{-4.4} \approx 4 \times 10^{-5}$. This measurement was performed in a Hg vapor cell at lab temperature (T = 298 K). We had 6 W of laser power and a 1-mm laser-beam radius ω_0. For these setting, we expected $\dot{N}_{{}^3P_0} = 9.7 \times 10^9$ [Hz]. We binned the data in 3 MHz windows, so for a 100 kHz effective linewidth at 298 K, we would expect an effective OD of 1.5. In

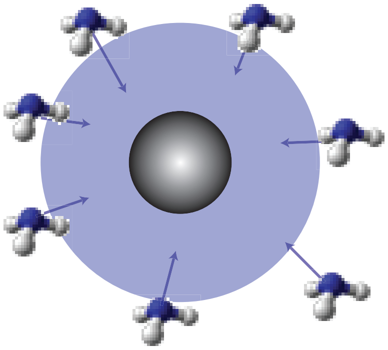

Figure 7.7: **NH_3 Detection Scheme** Collision of a $^3P_0$ Hg atom with NH_3 is known to relax in the UV.

total this gave us an estimated detection rate $\dot{N}_D = 1.2 \times 10^4$ Hz, well above the background noise. While our estimated signal-to-noise made this experiment seem viable, no signal was detected with this method. This may be due to the increased collision effects from NH_3 that are not included in the excitation rate estimates $\dot{N}_{^3P_0}$ but could conceivably attenuate an E1-M1 detection rate through collision effects.

7.6.2 Active: $^3S_1$

An alternative detection avenue is an E1-allowed transition between $6s6p^3P_0 \rightarrow 6s7s^3S_1$, see Figure 1.1 for the level structure. The $^3P_0$ level is coupled to the $^3S_1$ level by a 405 nm photon, which is the Blu-Ray wavelength and therefore a ubiquitous diode laser. The $^3S_1$ relaxation is through a unique wavelength (436 nm) and so can be filtered from the excitation (531 nm) and probe (405 nm) light for detection.

The initial E1-M1 excitation of atoms in motion to the $^3P_0$ clock level will need to be time separated from the detection of still moving $^3P_0$ atoms to avoid additional light shift from the 405 nm light and natural broadening from the $^3S_1$ linewidth. Sequencing excitation and detection harms the duty cycle of the experiment compared with concurrent measurement methods. The $^3S_1$ transition has a linewidth of 20 MHz [5], so the detection time can be brief. The $^3S_1$ level cascades to the ground level predominantly through the $6s6s\,^3P_1$ intermediate level [5]. This cascade channel radiates at 436 nm, a wavelength distinct from all others in the system.

We obtained a Blu-Ray laser diode and attempted blind cycling on this transition. The laser was free-running, which is risky because broad-band lasers do not emit at all frequencies under the larger frequency envelope. The $^3P_0 \rightarrow {}^3S_1$ transition frequency may have been dark in the laser.

Free-running was a good first step because there are challenges with the narrow linewidth of a cavity locked laser. Specifically, a $^3S_1$ detection scheme for the novel detection of the E1-M1 transition would require the primary search for the exact (and in some cases unknown) isotope transition frequencies between $^1S_0 \rightarrow {}^3P_0$ and a concurrent secondary search for the completely unknown $^3P_0 \rightarrow {}^3S_1$ transition frequencies. This would mean detection of an E1-M1 clock excitation would be a two degree-of-freedom walk across 531 nm and 405 nm space to find the clock resonances and the detection resonances.

Our detection attempts included the implementation of a crude Hg discharge lamp setup to excite the $^3P_0 \rightarrow {}^3S_1$ transition, but that was flawed because it also radiated at our signal wavelength of 436 nm.

CHAPTER VIII

Conclusion

8.1 An Undetected Transition

Efforts to observe the E1-M1 transition in are detailed in §7.6.1. In short, despite operating in a favorable parameter space where an estimated signal of 10 kHz above noise of 40 Hz, we did not observe the E1-M1 optical transition. This begs the question: why not? The best model for the E1-M1 excitation scheme is outlined in this dissertation. Here is a heuristic explanation of what may have gone wrong.

The collision broadening and collision loss rate models were based on a very simple, billiard-ball model of the atoms. It may be that there are collision dynamics at play which profoundly reduce the excitation rates.

The detection channels are the least understood systems. While we know NH_3 facilitates clock level relaxation in Hg, we don't know how the presence of NH_3 will affect the Hg excitation rate. Preliminary implementation of the $^3S_1$ coupled detection path did not generate signal. The 405 nm laser diode was free running, and such diode lasers typically have very broad frequency linewidths. Those frequency envelopes are also usually non-uniform, meaning there are enclosed frequencies that are dark. It's possible that the resonance frequency required for detection was in a dark frequency window of the laser. Implementation of an ECDL locking scheme would have given us the ability to scan methodically for 405 nm resonance, but this would have required a two-degree-of-freedom walk through the unknown $^1S_0 \rightarrow {}^3P_0$ transition and the unknown $^3P_0 \rightarrow {}^3S_1$ transition.

8.2 Comparision of E1-M1 to E1 Schemes

A hot E1-M1 Hg vapor cell can achieve small $\mathcal{S}$, comparable to the current minimum found in the Sr lattice clock [8]. Table 8.1 summarizes this along with other state-of-the-art frequency standards. We include the Rb chip [29] to allow comparison of an E1-M1 scheme to the best portable standard.

Table 8.1: The stability $\mathcal{S}$ and accuracy σ_ν of current frequency standards. The fundamental frequency ν, linewidth $\Delta\nu$, and detected atom number N are also listed for these systems.
(**bold** denotes predicted values)
fn - fountain, *cp* - chip, *ion* - ion, *lt* - lattice,
vp - hot vapor cell

Atom	ν [Hz]	$\Delta\nu$ [Hz]	N [#]	$\mathcal{S}$ $\sqrt{\text{Hz}^{-1}}$	σ_ν
Rb$_{cp}$[29]	6.8[9]			6[−11]	6[-12]
Cs$_{fn}$[27]	9.1[9]		1[7]	2[-13]	5[-16]
Hg$_{vp}$	5.6[14]	**2[5]**	**1.1[10]**	**3.1[−15]**	
Al$^+_{ion}$[12, 10]	1.1[15]	7	1	3.7[−16]	8.6[−18]
Yb$_{lt}$ [23]	5.2[14]	6	5[3]	3.2[−16]	1.6[−18]
Sr$_{lt}$ [8]	4.3[14]	6 − 50	2[3]	3.1[−16]	6.4[−18]

8.3 Looking Forward

I think it would be prudent as a next step to prepare a cold Hg sample and probe the E1-M1 clock transition this way. Ultracold Hg samples [34] (including a Hg lattice clock [35]) have already been developed. This would allow experimental verification of the E1-M1 optical transition properties (Chapter II) and some of the optical stability properties (Chapter IV). Detection would be trivial because ultracold samples can readily report ground state population and a reduction in ground state population could indicate clock state excitation.

With the goal of ultimately returning the E1-M1 standard to a hot setting, the cold system could help determine the exact transition frequencies for the clock transition $^1S_0 \rightarrow {}^3P_0$. Then the detection channel frequencies $^3P_0 \overset{\text{E1}}{\longleftrightarrow} {}^3S_1$ for each isotope of Hg could be searched for. When an E1-M1 resonance is found in the cold sample, the same light could be applied to a hot sample to explore NH_3 relaxation dynamics, which is desirable because it could be the basis of a passive detection scheme.

8.4 Conclusion

The prospects of a hot monochromatic E1-M1 clock as a portable frequency standard are compelling. The Hg system enjoys a large number of addressed atoms which improve its precision through statistics, but it suffers from a large, absolute frequency shift due to the intensity of the incident beam. The accuracy of this standard will require precise laser power metrology.

A frequency standard unbiased by the light shift due to excitation is achievable with a bichromatic E1-M1 scheme. This two-photon excitation scheme may enable current cold systems to completely eliminate systematic frequency bias. Such an absolutely accurate frequency standard can be used to place firm local and temporal bounds on acceleration due to gravity.

In this dissertation I have characterized the E1-M1 clock. I have shown how the clock-level excitation rates for each group II type atom depend on the experimentally-controlled parameters of vapor cell temperature T and laser-beam radius ω_0. Based on these calculations, neutral Hg is the optimal atomic system for a hot E1-M1 optical clock. With the conservative experimental parameters assumed in this paper, we calculate the stability for a hot Hg clock could be as low as $3.1 \times 10^{-15}\ \sqrt{\text{Hz}^{-1}}$. This stability is competitive with other optical frequency standards while offering the portability of a vapor cell.

APPENDICES

APPENDIX A

Symbol Conventions

A.1 Spin Notation - Russell Saunders Coupling Scheme

The atomic levels are referred to using the Russell Saunders coupling scheme notation [45]. For example, the clock level is referred to as ${}^3P_0$. This notation is a summary of the Spin-Spin (S), Orbit-Orbit (L), and Spin-Orbit (J) coupling of the denoted level. The specific notation is ${}^{2S+1}\mathsf{L}_J$, where when L$= 0, 1, 2, 3$ we denote it as $\mathsf{L} = S, P, D, F$.

A.2 Optical Frequency Standard Nomenclature

The language of optical frequency standards is remarkably imprecise. Any optical frequency standard result can be filtered into two metrics, the stability $\mathcal{S}$ and the instability σ_ν , and the community is converging on this nomenclature. However, in practice these metrics can be found under a variety of names. As a reminder, instability σ_ν is the final, statistical error in a resonant frequency measurement of an oscillator. Usually what is published as absolute σ_ν is the result a long duration measurement, perhaps hours, days, or months. The stability $\mathcal{S}$ is the extrapolated rate at which the instability was achieved (1.1). The best stability $\mathcal{S}$ measured in a clock can comes from a shorter measurement times τ than the best instability σ_ν.

If you are not sure which metric is being referenced, the instability σ_ν is dimensionless and stability has units $\sqrt{\text{Hz}^{-1}}$. Beware the reported $\mathcal{S}$ magnitude because it is sometimes reported in units of $\sqrt{days}$. "Fractional frequency instability" is used in the literature to describe both instability and stability, but dimensional analysis readily repairs the confusing landscape this creates.

Table A.1: Aliases for Instability σ_ν

Instability σ_ν
Accuracy
Fractional Frequency Uncertainty (ffu)
Fractional Frequency Instability [20]
1/Q
Allen Deviation

Table A.2: Aliases for Stability $\mathcal{S}$

Stability $\mathcal{S}$ [$\sqrt{\text{Hz}^{-1}}$]
Precision
Fractional Frequency Instability [3]

Accuracy usually is interchanged with instability σ_ν, and precision with stability $\mathcal{S}$. I use that nomenclature swap casually in this dissertation, but it is a problematic representation because both σ_ν and $\mathcal{S}$ have properties that can be meaningfully characterized in terms of accuracy and precision.

Good optical frequency standards attain low/small/minimal stabilities and instabilities. This is a confusing because "minimal stability" evokes a poor quality, but on the contrary it denotes an optimal quality.

In this dissertation I use the Δ- prefix to ν to denote a linewidth $\Delta\nu$ and I use an isolated ν to denote an absolute frequency, including a frequency shift. This has the potential to be confusing since a single Δ and δ denote a frequency offset in discussions and level diagrams of transition energy.

APPENDIX B

Modeling the Three-Level System

If we treat the clock system as a closed three-level Λ system, we can easily express the system in the Schrödinger picture so the probability amplitudes of the chosen eigenstates can be calculated numerically. The time-dependent Schrödinger equation is

$$i\hbar\frac{\delta}{\delta t}\Psi(t) = \mathbf{H}\Psi(t) \tag{B.1}$$

where the $\mathbf{H}$ is

$$\mathbf{H} = \mathbf{H}_0 + \mathbf{V}(t). \tag{B.2}$$

The unperturbed Hamiltonian $\mathbf{H}_0$ is

$$\mathbf{H}_0 = \hbar \begin{pmatrix} \omega_{^1S_0} & 0 & 0 \\ 0 & \omega_{^3P_1} & 0 \\ 0 & 0 & \omega_{^3P_0} \end{pmatrix} \tag{B.3}$$

and the interaction Hamiltonian $\mathbf{V}(t)$ is

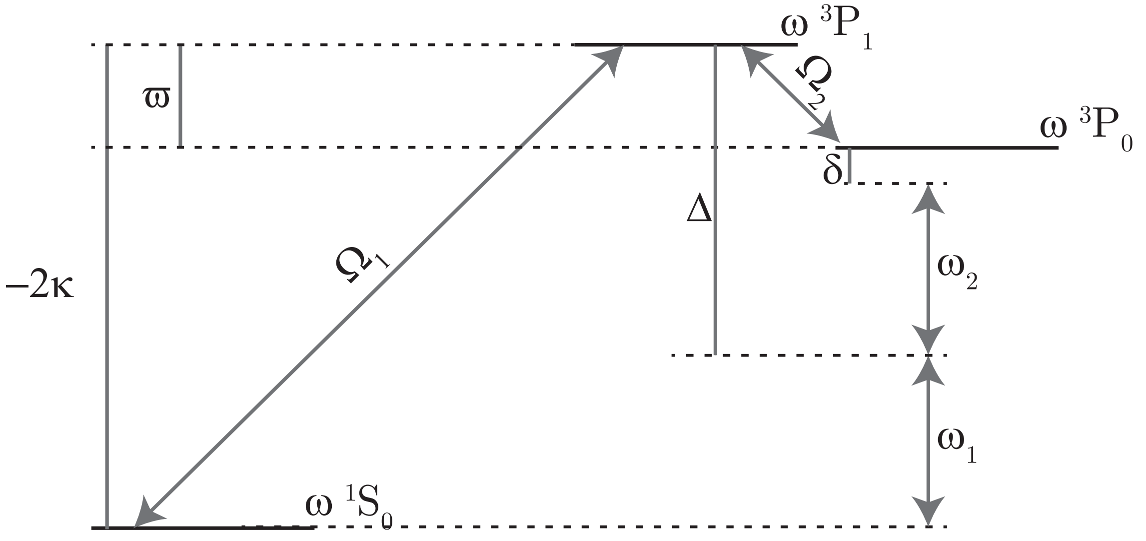

Figure B.1: **Level Structure, Frequencies, and Coupling in a Λ System** This diagram shows the frequency scale and coupling of the clock system for modeling.

$$\mathbf{V}(t) = \hbar \begin{pmatrix} 0 & |\Omega_1|\cos(\omega_1 t) & 0 \\ |\Omega_1|\cos(\omega_1 t) & 0 & |\Omega_2|\cos(\omega_2 t) \\ 0 & |\Omega_2|\cos(\omega_2 t) & 0 \end{pmatrix}. \tag{B.4}$$

where I have made the dipole approximation. I also assume that Rabi frequency Ω_n and phase of the laser do not vary with time. I articulate the bichromatic case where laser frequencies $\omega_1 \neq \omega_2$ in the interaction Hamiltonian. I have implicitly assumed that the bichromatic solution frequencies ω_1 and ω_2 are the dominant oscillators coupling the ${}^3P_1 - {}^1S_0$ and ${}^3P_1 - {}^3P_0$ respectively. I will express the time-varying component of each $\Psi_i(t)$ as the probability amplitudes $a_i(t)$ of the static eigenstate ψ_i, specifically

$$\mathbf{\Psi}(t) = \mathbf{a}(t)\psi \tag{B.5}$$

Now I can solve for the probability amplitudes of this closed, Λ system

$$i\hbar \begin{pmatrix} \dot{a}_1(t) \\ \dot{a}_2(t) \\ \dot{a}_3(t) \end{pmatrix} = \hbar \begin{pmatrix} \omega_{^1S_0} & |\Omega_1|\cos(\omega_1 t) & 0 \\ |\Omega_1|\cos(\omega_1 t) & \omega_{^3P_1} & |\Omega_2|\cos(\omega_2 t) \\ 0 & |\Omega_2|\cos(\omega_2 t) & \omega_{^3P_0} \end{pmatrix} \begin{pmatrix} a_1(t) \\ a_2(t) \\ a_3(t) \end{pmatrix}. \tag{B.6}$$

If simulation time-steps, t, are chosen to be smaller than the characteristic frequencies of the system, then the Hamiltonian can be treated as time-independent and the probability amplitudes can be evolved according to

$$a_i(t_0 + t) = e^{-i\mathbf{H}t/\hbar} a_i(t_0) \tag{B.7}$$

B.0.1 Adiabatic Approximation

The adiabatic approximation can be described as the assumption that if a two-photon transition coupled to an intermediate level is driven by photons that are each far detuned from that intermediate level, then we can assume the time-varying probability amplitude of the intermediate level will oscillate rapidly and average to zero $\dot{a}_2 = 0$ [48, 9]. The probability amplitude of the intermediate level will be small, but non-zero enabling us to solve (B.6).

As is customary, I will also define (and invert) the energy levels such that $-2\kappa = \omega_{^3P_1} - \omega_{^1S_0}$ such that when $\omega_{^1S_0} \rightarrow \kappa$ then $\omega_{^3P_0} \rightarrow -\kappa$. I will also simplify $\mathit{\Omega}_i = |\Omega_i|\cos(\omega_i t)$ and $\varpi = -\kappa + (\omega_{^3P_1} - \omega_{^3P_0})$. This results in re-writing (B.6) as

$$\begin{aligned} i\dot{a}_1 &= \kappa a_1 + \mathit{\Omega}_1 a_2 && \text{(B.8)} \\ i\dot{a}_2 &= \mathit{\Omega}_1 a_1 - \kappa a_2 + \mathit{\Omega}_2 a_3 && \text{(B.9)} \\ i\dot{a}_3 &= \mathit{\Omega}_2 a_2 + \varpi a_3 && \text{(B.10)} \end{aligned}$$

When we implement the assumption that $\dot{a}_2 \approx 0$ we find (B.9) can be simplified to

$$\varOmega_1 a_1 - \kappa a_2 + \varOmega_2 a_3 \approx 0 \tag{B.11}$$

$$a_2 = \frac{\varOmega_1}{\kappa} a_1 + \frac{\varOmega_2}{\kappa} a_3 \tag{B.12}$$

When we express a_2 in terms of a_1 and a_3 in equations (B.8) and (B.10), this produces an effective two level system

$$i\dot{a}_1 = \kappa a_1 + \varOmega_1 \left(\frac{\varOmega_1}{\kappa} a_1 + \frac{\varOmega_2}{\kappa} a_3 \right) \tag{B.13}$$

$$i\dot{a}_3 = \varOmega_2 \left(\frac{\varOmega_1}{\kappa} a_1 + \frac{\varOmega_2}{\kappa} a_3 \right) + \varpi a_3 \tag{B.14}$$

A characteristic frequency in the E1-M1 system is the two-photon Rabi frequency $\Omega_{R2\gamma}$ (2.3) where

$$\Omega_{R2\gamma} := \frac{\Omega_1 \Omega_2}{\kappa} \tag{B.15}$$

and if your eyes haven't glazed over in this equation landscape, you will see $\Omega_{R2\gamma}$ start to appear in (B.13) and (B.13). That pair of equations has the form

$$i\dot{a}_1 = A a_1 + \Omega_{R2\gamma} a_3 \tag{B.16}$$

$$i\dot{a}_3 = \Omega_{R2\gamma} a_1 + B a_3 \tag{B.17}$$

where

$$
\begin{aligned}
A &:= \kappa + \frac{\mathit{\Omega_1}^2}{\kappa} && \text{(B.18)}\\
B &:= \varpi + \frac{\mathit{\Omega_2}^2}{\kappa} && \text{(B.19)}
\end{aligned}
$$

These coefficients A and B reveal the effective light shifts to the $\omega_{{}^1S_0}$ and $\omega_{{}^3P_0}$ levels by $\frac{\mathit{\Omega_1}^2}{\kappa}$ and $\frac{\mathit{\Omega_2}^2}{\kappa}$ respectively. This approximation of the light shift is for the simplified three-level system.

The coupled equations (B.16) and (B.17) for an effective two-level system have well known solution [43]. If we assume all population is in the ground state initially ($a_1(0) = 1$), then we can report the probability amplitude of $a_3(t)$ at time t as

$$
a_3(t) = -i\frac{\Omega_{R2\gamma}}{\sqrt{\delta^2 + \Omega_{R2\gamma}^2}} \sin\left(\frac{\sqrt{\delta^2 + \Omega_{R2\gamma}^2}}{2} t\right) \tag{B.20}
$$

where δ is the detuning from the light shifted resonance. We implement this result in our E1-M1 analysis to determine the probability of clock excitation (2.4) where $P_{{}^3P_0} = a_3^* a_3$.

Symbols	
$\Omega_n = -dF/\hbar$	Rabi Frequency
d	reduced dipole matrix element
F	Electric field
$\mathbf{a}_i(t)$	time-varying amplitude in Schrdinger picture
ω_i	laser frequency i
$\mathbf{H}_0$	unperturbed Hamiltonian
$\mathbf{H}$	Hamiltonian
$\mathbf{V}(t)$	interaction Ham
Λ	three level structure like ...
δ	$\frac{\omega_{^1S_0} - \omega_{^3P_1}}{2}$
κ	the detuning from the light shifted resonance
$\Omega_{R2\gamma}$	two-photon Rabi frequency
$\mathit{\Omega}_i$	$\lvert\Omega_i\rvert \cos(\omega_i t)$
ϖ	$-\kappa + (\omega_{^3P_1} - \omega_{^3P_0})$

Table B.1: Symbols in Appendix B for Λ-type system atom-photon dynamics

BIBLIOGRAPHY

BIBLIOGRAPHY

[1] C. B. Alcock, V. P. Itkin, and M. K. Horrigan. Vapour Pressure Equations for the Metallic Elements: 298-2500 K. *Canadian Metallurgical Quarterly*, 3:309–313, 1984.

[2] Z. Barber, C. Hoyt, C. Oates, L. Hollberg, A. Taichenachev, and V. Yudin. Direct Excitation of the Forbidden Clock Transition in Neutral ^{174}Yb Atoms Confined to an Optical Lattice. *Phys. Rev. Lett.*, 96(8):083002, March 2006.

[3] A. Bartels, S. A. Diddams, C. W. Oates, G. Wilpers, J. C. Bergquist, W. H Oskay, and L. Hollberg. Femtosecond-laser-based synthesis of ultrastable microwave signals from optical frequency references. *Optics letters*, 30(6):667–669, 2005.

[4] K. Beloy, J. A. Sherman, N. D. Lemke, N. Hinkley, C. W. Oates, and A. D. Ludlow. Determination of the 5d6s $^3D_1$ state lifetime and blackbody-radiation clock shift in Yb. *Phys. Rev. A*, 86(5):051404, November 2012.

[5] E. C. Benck, J. E. Lawler, and J. T. Dakin. Lifetimes, branching ratios, and absolute transition probabilities in Hg I. *Journal of the Optical Society of America B*, 6(1):11, January 1989.

[6] J. Bieroń, P. Indelicato, and P. Jönsson. Multiconfiguration Dirac-Hartree-Fock calculations of transition rates and lifetimes of the eight lowest excited levels of radium. *The European Physical Journal Special Topics*, 144(1):75–84, May 2007.

[7] F. Biraben, B. Cagnac, and G. Grynberg. Experimental evidence of two-photon transition without doppler broadening. *Phys. Rev. Lett.*, 32:643–645, Mar 1974.

[8] B. J. Bloom, T. L. Nicholson, J. R. Williams, S. L. Campbell, M. Bishof, X. Zhang, W. Zhang, S. L. Bromley, and J. Ye. An optical lattice clock with accuracy and stability at the 10^{-18} level. *Nature*, advance on, January 2014.

[9] E. Brion, L. H. Pedersen, and K. Mølmer. Adiabatic elimination in a lambda system. *Journal of Physics A: Mathematical and Theoretical*, 40(5):1033, 2007.

[10] C. W. Chou, D. B. Hume, J. C. J. Koelemeij, D. J. Wineland, and T. Rosenband. Frequency Comparison of Two High-Accuracy Al$^+$ Optical Clocks. *Phys. Rev. Lett.*, 104(7), February 2010.

[11] C. W. Chou, D. B. Hume, T. Rosenband, and D. J. Wineland. Optical Clocks and Relativity. *Science*, 329(5999):1630–1633, September 2010.

[12] C. W. Chou, D. B. Hume, M. Thorpe, D. J. Wineland, and T. Rosenband. Quantum Coherence between Two Atoms beyond Q=10^{15}. *Phys. Rev. Lett.*, 106(16), April 2011.

[13] L. J. Curtis. *Atomic Structure and Lifetimes.* Cambridge University Press, Cambridge, 2001.

[14] J. Dalibard and C. Cohen-Tannoudji. Laser cooling below the Doppler limit by polarization gradients: simple theoretical models. *Journal of the Optical Society of America B*, 6(11):2023, November 1989.

[15] P. Del'Haye, T. Herr, E. Gavartin, M. L. Gorodetsky, R. Holzwarth, and T. J. Kippenberg. Octave spanning tunable frequency comb from a microresonator. *Phys. Rev. Lett.*, 107(6):063901, 2011.

[16] V. A. Dzuba and A. Derevianko. Dynamic polarizabilities and related properties of clock states of the ytterbium atom. *Journal of Physics B: Atomic, Molecular and Optical Physics*, 43(7):074011, 2010.

[17] V. A. Dzuba, V. V. Flambaum, and J. S. M. Ginges. Calculation of parity and time invariance violation in the radium atom. *Phys. Rev. A*, 61(6):062509, May 2000.

[18] F.-X. Esnault, E. Blanshan, E. N. Ivanov, R. E. Scholten, J. Kitching, and E. A. Donley. Cold-atom double-λ coherent population trapping clock. *Phys. Rev. A*, 88(4):042120, 2013.

[19] M. M. Fejer, G. A. Magel, D. H. Jundt, and R. L. Byer. Quasi-phase-matched second harmonic generation: tuning and tolerances. *IEEE Journal of Quantum Electronics*, 28(11):2631–2654, 1992.

[20] T. M. Fortier, M. S. Kirchner, F. Quinlan, J. Taylor, J. C. Bergquist, T. Rosenband, N. Lemke, A. Ludlow, Y. Jiang, C. W. Oates, et al. Generation of ultrastable microwaves via optical frequency division. *Nature Photonics*, 5(7):425–429, 2011.

[21] S. Gerstenkorn and P. Luc. Atlas du spectre d'absorption de la molecule d'iode 14800-20000 cm^{-1}. *Paris: Editions du Centre National de la Recherche Scientifique (CNRS), 1978*, 1, 1978.

[22] TL Gustavson, P Bouyer, and MA Kasevich. Precision rotation measurements with an atom interferometer gyroscope. *Phys. Rev. Lett.*, 78(11):2046–2049, 1997.

[23] N Hinkley, J A Sherman, N B Phillips, M Schioppo, N D Lemke, K Beloy, M Pizzocaro, C W Oates, and A D Ludlow. An atomic clock with 10^{-18} instability. *Science (New York, N.Y.)*, 341(6151):1215–8, September 2013.

[24] T. Hong, C. Cramer, E. Cook, W. Nagourney, and E. N. Fortson. Observation of the $^1S_0 - {}^3P_0$ transition in atomic ytterbium for optical clocks and qubit arrays. *Optics Letters*, 30(19):2644, October 2005.

[25] M. L. Huber, A. Laesecke, and D. G. Friend. The Vapor Pressure of Mercury. Technical report, 2006.

[26] N. Huntemann, B. Lipphardt, M. Okhapkin, Chr. Tamm, E. Peik, A. V. Taichenachev, and V. I. Yudin. Generalized Ramsey Excitation Scheme with Suppressed Light Shift. *Phys. Rev. Lett.*, 109(21):213002, November 2012.

[27] S. R. Jefferts, T. P. Heavner, T. E. Parker, and J. H. Shirley. *NIST cesium fountains: current status and future prospects*. SPIE, 2007.

[28] V. V. Karasiev, L. N. Labzowsky, and A. V. Nefiodov. Parity violation in heliumlike uranium. *Physics Letters A*, 172(1-2):62–65, December 1992.

[29] S. Knappe, V. Gerginov, P. D. D. Schwindt, V. Shah, H. G. Robinson, L. Hollberg, and J. Kitching. Atomic vapor cells for chip-scale atomic clocks with improved long-term frequency stability. *Optics Letters*, 30(18):2351, September 2005.

[30] A. Kramida, Y. Ralchenko, J. Reader, and NIST ASD Team. NIST Atomic Spectra Database (ver. 5.1), [Online]. Available: `http://physics.nist.gov/asd` [2013, November 11]. National Institute of Standards and Technology, Gaithersburg, MD., 2013.

[31] R. Küch and T. Retschinsky. Photometrische und spektralphotometrische messungen am quecksilberlichtbogen bei hohem dampfdruck. *Annalen der Physik*, 325(8):563–583, 1906.

[32] A. Ludlow, M. Boyd, T. Zelevinsky, S. Foreman, S. Blatt, M. Notcutt, T. Ido, and J. Ye. Systematic Study of the ^{87}Sr Clock Transition in an Optical Lattice. *Phys. Rev. Lett.*, 96(3):033003, January 2006.

[33] J. C. McConnell and B. L. Moiseiwitsch. Charge-transfer cross sections and mobilities for Hg^+ ions in atomic mercury. *Journal of Physics B: Atomic and Molecular Physics*, 2(8):821, 1969.

[34] J. J. McFerran, L. Yi, S. Mejri, and S. Bize. Sub-Doppler cooling of fermionic Hg isotopes in a magneto-optical trap. *Optics letters*, 35(18):3078–3080, 2010.

[35] J. J. McFerran, L. Yi, S. Mejri, S. Di Manno, W. Zhang, J. Guéna, Y. Le Coq, and S. Bize. Neutral Atom Frequency Reference in the Deep Ultraviolet with Fractional Uncertainty=5.7×10^{-15}. *Physical Review Letters*, 108(18), May 2012.

[36] A. P. Mishra and T. K. Balasubramanian. Radiative lifetimes of the first excited $^3P_{2,0o}$ metastable levels in Kr I, Xe I, Yb I and Hg-like atoms. *Spectroscopy*, 69(6):769–780, 2001.

[37] J. Mitroy, M. S. Safronova, and C. W Clark. Theory and applications of atomic and ionic polarizabilities. *Journal of Physics B: Atomic, Molecular and Optical Physics*, 43(20):202001, October 2010.

[38] K. Moler, D. S. Weiss, M. Kasevich, and S. Chu. Theoretical analysis of velocity-selective raman transitions. *Phys. Rev. A*, 45:342–348, Jan 1992.

[39] R. H. Newman, C. G. Freeman, M. J. McEwan, R. F. C. Claridge, and L. F. Phillips. Mercury-sensitized luminescence of NH3 and ND3. *Transactions of the Faraday Society*, 66:2827, 1970.

[40] M. Petersen, R. Chicireanu, S. T. Dawkins, D. V. Magalh Aes, C. Mandache, Y. Le Coq, A. Clairon, and S. Bize. Doppler-Free Spectroscopy of the $^1S_0 - {}^3P_0$ Optical Clock Transition in Laser-Cooled Fermionic Isotopes of Neutral Mercury. *Physical Review Letters*, 101(18), 2008.

[41] N. Poli, Z. Barber, N. Lemke, C. Oates, L. Ma, J. Stalnaker, T. Fortier, S. Diddams, L. Hollberg, J. Bergquist, A. Brusch, S. Jefferts, T. Heavner, and T. Parker. Frequency evaluation of the doubly forbidden $^1S_0 \rightarrow {}^3P_0$ transition in bosonic ^{174}Yb. *Phys. Rev. A*, 77(5):050501, May 2008.

[42] S. Porsev, M. Kozlov, Yu. Rakhlina, and A. Derevianko. Many-body calculations of electric-dipole amplitudes for transitions between low-lying levels of Mg, Ca, and Sr. *Phys. Rev. A*, 64(1):012508, June 2001.

[43] N. F. Ramsey. A molecular beam resonance method with separated oscillating fields. *Phys. Rev.*, 78:695–699, Jun 1950.

[44] T. Rosenband, D. B. Hume, P. O. Schmidt, C. W. Chou, A. Brusch, L. Lorini, W. H. Oskay, R. E. Drullinger, T. M. Fortier, J. E. Stalnaker, S. A. Diddams, W. C. Swann, N. R. Newbury, W. M. Itano, D. J. Wineland, and J. C. Bergquist. Frequency ratio of Al$^+$ and Hg$^+$ single-ion optical clocks; metrology at the 17th decimal place. *Science (New York, N.Y.)*, 319(5871):1808–12, March 2008.

[45] H. N. Russell and F. A. Saunders. New regularities in the spectra of the alkaline earths. *The Astrophysical Journal*, 61:38, 1925.

[46] G. K. Samanta, S. C. Kumar, and M. Ebrahim-Zadeh. Stable, 9.6 W, continuous-wave, single-frequency, fiber-based green source at 532 nm. *Opt. Lett.*, 34(10):1561–1563, May 2009.

[47] H. Schäffer, R. Dunford, E. Kanter, S. Cheng, L. Curtis, A. Livingston, and P. Mokler. Measurement of the two-photon spectral distribution from decay of the 1s2s $^1S_0$ level in heliumlike nickel. *Physical Review A*, 59(1):245–250, January 1999.

[48] B. W. Shore. *The theory of coherent atomic excitation*, volume 2. Wiley (New York), 1990.

[49] M. Takamoto, F.-L. Hong, R. Higashi, and H. Katori. An optical lattice clock. *Nature*, 435(7040):321–324, 2005.

[50] T. Udem, R. Holzwarth, and T. W. Hänsch. Optical frequency metrology. *Nature*, 416(6877):233–237, 2002.

[51] C. Vian, P. Rosenbusch, H. Marion, S. Bize, L. Cacciapuoti, S. Zhang, M. Abgrall, D. Chambon, I. Maksimovic, P. Laurent, et al. BNM-SYRTE fountains: recent results. *Instrumentation and Measurement, IEEE Transactions on*, 54(2):833–836, 2005.

[52] A. Ye and G. Wang. Dipole polarizabilities of ns^2 $^1S_0$ and nsnp $^3P_0$ states and relevant magic wavelengths of group-IIB atoms. *Phys. Rev. A*, 78(1), July 2008.

[53] L. Yi, S. Mejri, J. J. McFerran, Y. Le Coq, and S. Bize. Optical Lattice Trapping of ^{199}Hg and Determination of the Magic Wavelength for the Ultraviolet $^1S_0 - ^3P_0$ Clock Transition. *Physical Review Letters*, 106(7), February 2011.

[54] V. Yudin, A. Taichenachev, C. Oates, Z. Barber, N. Lemke, A. Ludlow, U. Sterr, Ch. Lisdat, and F. Riehle. Hyper-Ramsey spectroscopy of optical clock transitions. *Phys. Rev. A*, 82(1), July 2010.

[55] T. Zanon-Willette, A. Ludlow, S. Blatt, M. Boyd, E. Arimondo, and J. Ye. Cancellation of Stark Shifts in Optical Lattice Clocks by Use of Pulsed Raman and Electromagnetically Induced Transparency Techniques. *Phys. Rev. Lett.*, 97(23):233001, December 2006.

[56] T. Zelevinsky, M. M. Boyd, A. D. Ludlow, S. M. Foreman, S. Blatt, T. Ido, and J. Ye. Optical clock and ultracold collisions with trapped strontium atoms. *Hyperfine Interactions*, 174(1-3):55–64, 2007.